Noise in Nonlinear Fiber-Optic Systems

Inaugural Dissertation
of the Faculty of Science
University of Bern

Presented by
Benoît Sierro
from Hérémence (CH)

Supervisor of the doctoral thesis:

Prof. Dr. Alexander Heidt
Institute of Applied Physics
of the University of Bern

Noise in Nonlinear Fiber-Optic Systems

Inaugural Dissertation
of the Faculty of Science
University of Bern

Presented by
Benoît Sierro
from Hérémence (CH)

Supervisor of the doctoral thesis:
Prof. Dr. Alexander Heidt
Institute of Applied Physics
of the University of Bern

Accepted by the Faculty of Science.

Bern, 21 October 2024

The Dean
Prof. Dr. Jean-Louis Reymond

Abstract

The optical frequency comb (OFC) is a laser-based technology that has revolutionized metrology, enabling timing and frequency measurements with unprecedented precision. Beyond their original purpose, OFCs have been adopted in various fields of fundamental science and emerging technologies such as autonomous driving and wireless communications. However, current challenges in generating low-noise OFC sources at high repetition rates with sufficient optical bandwidth hinder their full potential. To address these challenges, supercontinuum (SC) generation in nonlinear fiber optics is an attractive approach because it can provide a large bandwidth at relatively low pump power, but at the cost of noise amplification. This thesis explores new ways to generate low-noise SC-based OFC sources to meet the ever-increasing demands of these novel applications. The first proposed solution is a hybrid fiber that combines the best qualities of both SC generation regimes. With this fiber, it is possible to generate an ultra-low noise fiber SC covering the 930–2130 nm range with phase coherence close to unity, spectrally resolved relative intensity noise (RIN) as low as 0.05 %, and averaging 0.01 % over a bandwidth of 750 nm, approaching the theoretical limits close to the pump laser noise. The second important result of this work is the development of a new numerical method, capable of simulating entire trains of ultrafast pulses propagating in nonlinear fibers and studying the evolution of their noise properties. We use this model to corroborate and explain measurements of unprecedented low noise observed on a dual-comb SC source, including shot-noise-limited SC generation and up to 20 dB of RIN suppression. Finally, hollow-core fibers are introduced as a promising way to reach new SC regimes, including deep UV pulses and TW peak power.

Contents

Chapter 1

Introduction

Optical frequency combs (OFCs) emit spectra of perfectly spaced, phase-coherent, and ultra-precise laser lines resembling the teeth of a comb. Their realization more than two decades ago, enabled by advances in femtosecond lasers and nonlinear optical fiber technology, was originally motivated by their groundbreaking impact in metrology. OFCs act as frequency rulers seamlessly connecting microwave and optical frequencies, leading to timing and frequency measurements with precision more than five orders of magnitude higher than the previous standards set by radio frequency atomic clocks (2005 Nobel Prize [1, 2]). Very rapidly, frequency combs were adopted into other fields of fundamental science beyond their original purpose with unforeseen success. For instance, they became essential in attosecond science (2023 Nobel Prize [3]) for precise control of the carrier-envelope phase of ultrashort pulses, revolutionized molecular spectroscopy, enabled the construction of all-optical atomic clocks, and facilitated coherent quantum system control [4, 5].

While the first generation of frequency comb sources have been predominantly confined to fundamental research laboratories, there is an accelerating trend for OFC sources to become key-drivers in consumer applications, including many emerging technologies, such as autonomous driving, high capacity fiber-optic and 6G wireless communications, and artificial intelligence [6–8]. Additionally, they are fundamental to the development of pioneering new tools for high-speed medical imaging, climate change monitoring, and the exploration of exoplanets [9, 10].

Historically, advances in OFC technology and nonlinear fiber optics have been closely linked. Two decades ago, the emergence of self-referenced OFC sources was dependent on advancements of microstructured photonic crystal fiber (PCF) technology enabling the coherent, octave-spanning broadening of narrowband combs emitted by mode-locked lasers at repetition rates in the 100 MHz range [11]. Today we face similar challenges: the demand for OFC sources at tens or even hundreds of GHz repetition rate results in lower pulse energies for the same average power, making it challenging to use nonlinear broadening to produce the octave bandwidths required for self-referencing. Ultimately, new concepts for increasing nonlinearity and design flexibility will be required.

Recently, the noise amplification inherent to the supercontinuum generation (SCG) process has received increasing attention due to its importance for

high-sensitivity metrology, spectroscopy and imaging applications [12, 13]. The increase in noise is particularly critical for supercontinuum (SC) sources operating in the anomalous dispersion regime (negative group velocity dispersion). This regime enables the generation of ultra-wide bandwidths driven by nonlinear dynamics based on soliton self-compression and soliton fission effects. However, this regime is prone to strong noise amplification due to modulation instabilities and stimulated Raman scattering (SRS) leading to reduced spectral coherence [14]. Similarly, these SC sources exhibit much higher relative intensity noise (RIN) than the driving laser [15, 16]: the shot-noise of the pump laser can be amplified by up to about 90 dB [15–17].

While experimental research has been aware of the importance of noise, few contributions have been published on the numerical study of such noise phenomena [18], especially when it comes to how nonlinear spectral broadening affects the noise power spectral density (PSD) of fluctuations in the pulse train. These fluctuations occur at frequencies up to half the repetition rate, typically in the radio frequency (RF) domain. Pulse propagation equations and numerical integration schemes already abound in the literature, providing all the tools to simulate single pulses in various nonlinear optical systems. In this context, there is an opportunity to contribute and provide a new numerical model capable of simulating entire pulse trains and analyzing their noise evolution during the SCG process. There is no doubt that such a model is crucial for a better understanding of the physical mechanisms that affect noise evolution in the spectral broadening of OFC sources.

This thesis explores new ways of generating low-noise OFCs using SCG. Chapter 2 begins with a breakdown of some of the phenomena that lead to the nonlinear spectral broadening observed when short, high-intensity pulses travel through optical fibers. It introduces the distinction between anomalous, or *conventional*, SCG and all-normal dispersion (ANDi) SCG, which is a central point of this work. It also gives a summary of the numerical integration methods used throughout this thesis. Finally, this chapter will cover the theory behind some nonlinear noise dynamics and how they are affected by SCG in different dispersion regimes.

Chapter 3 addresses the fact that it is challenging to generate a SC spectrum that is both low-noise and broadband at low peak power in a single fiber. To resolve this conundrum, a new hybrid fiber design is proposed. It combines the advantages of both conventional and ANDi SCG. Supported by both experimental measurements and numerical simulations, it is argued that this hybrid fiber exhibits the lowest RIN known to date for an octave-spanning SC while using inexpensive, commercially available fibers.

The limits of low noise OFCs are challenged again in Chapter 4. It presents experimental evidence of up to 20 dB of RIN suppression while generating a 400 nm SC at 1053 nm. With a single-cavity, dual-comb oscillator, it is possible to generate two identical SC spectra in a single ANDi fiber using polarization multiplexing. Nonlinear interaction between both comb during the spectral broadening process are investigated numerically, and experimental results confirm that they do not compromise dual-comb interferometry (DCI) measurements. With its exceptional combination of high power, high bandwidth and low noise, this system is highly attractive for any dual-comb sensing applications such as broadband spectroscopy, hyperspectral LiDAR and imaging, as well as multicolor pump-probe measurements.

In order to verify the RIN suppression mentioned above and study its physical origin, a new simulation method is developed in Chapter 5. This method is capable of generating a realistic pulse train from a standard, RF noise measurement. By propagating each pulse with conventional methods and analyzing the resulting pulse train statistically, accurate reproduction of real noise PSD measurements are achieved. This new numerical framework is both highly flexible and easy to implement atop an existing numerical tool set, which is expected to lead researchers in performing more extensive noise analyses when simulating SCG.

Finally, while much of this work is focused on noise characterization and control, Chapter 6 explores nonlinear broadening of fs pulses at high power in hollow-core fibers. With the aim of building a system capable of generating short, deep ultraviolet (UV) pulses [19] for use in ultrafast spectroscopy, we present our mechanical design approach as well as initial results of SC spectra observed in gas-filled capillary tubes and hollow-core photonic crystal fibers.

Chapter 2

Theory

The physical principles behind the nonlinear broadening of ultrafast pulses in nonlinear fibers have been studied extensively [14, 20–23]. This chapter gives an overview of these phenomena, focusing mainly on the elements most relevant to the rest of this thesis.

SCG processes in optical fibers are based on the interplay between the chromatic dispersion of a fiber and its nonlinear refractive index. They can be classified into two families, depending on the relationship between the pump wavelength and the group-velocity dispersion (GVD) profile of the fiber used. *Conventional* SCG occurs when a fiber is pumped in the anomalous region of its GVD, close to its zero dispersion wavelength (ZDW). There, if the peak power is high enough, the anomalous dispersion cannot compensate for the nonlinear phase induced on the pulse by the Kerr effect. After an initial phase in which the pulse is compressed, it is perturbed by Raman scattering and higher-order dispersion until it breaks apart in a process called *soliton fission*. This results in a complexly structured spectrum spanning a large bandwidth, where phase matching between the normal and anomalous dispersion regimes allows energy transfer from longer wavelength solitons to shorter wavelength dispersive waves (DWs), thereby redshifting these solitons.

As with conventional SCG, ANDi SCG is based on the interaction between Kerr-induced self-phase modulation (SPM) and GVD. As the name implies, ANDi fibers exhibit only positive GVD in the wavelength range of interest. Since SPM introduces a linear chirp in the center of the pulse, normal dispersion works to push the newly created frequencies toward the head and tail of the pulse, making it nearly rectangular. If phase matching conditions are met, interferences between the pump frequency and these new frequencies create spectral sidebands through a mechanism known as optical wave-breaking (OWB).

Recently, the focus has shifted to low-noise SC sources [24–26]. Indeed, the noise performance of these sources plays a critical role in many applications, affecting precision, acquisition time and signal-to-noise ratio (SNR). Consequently, a good understanding of the noise evolution during SCG is crucial for the design of ultra-low noise systems for the most demanding applications. In terms of noise, conventional and ANDi SCG are not the same. While conventional SC spectra are typically broader than their ANDi counterparts when pumped with comparable pulses, the underlying physical mechanisms tend to greatly amplify fluctuations in the pump, especially at longer pulse durations.

2.1 Nonlinear Spectral Broadening in Optical Fibers

The complex envelope of an ultrashort pulse traveling through a single-mode optical fiber is written as $A(z, \tau)$, where z stands for the propagation distance and τ for the delay in a frame of reference traveling at the pump group velocity. This makes use of the slowly varying envelope approximation, which has been validated for all realistic pulse durations, down to the single cycle [27, 28]. A is scaled such that $I := |A(z, \tau)|^2$ gives the instantaneous power in W.

2.1.1 Dispersion

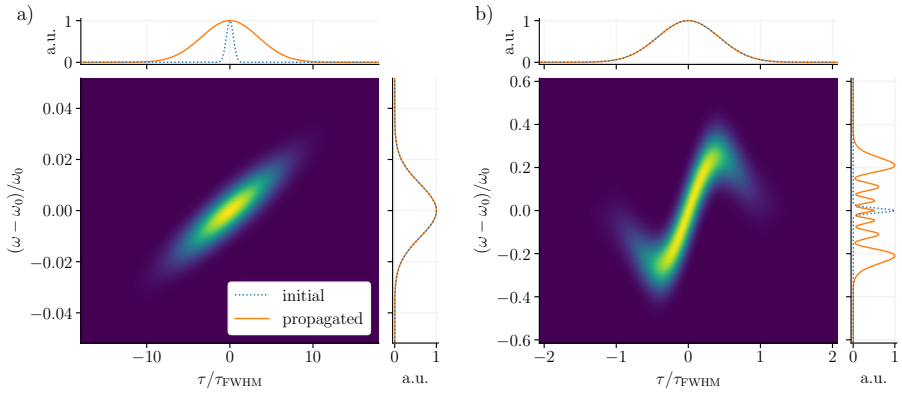

Figure 2.1: Spectrograms of Gaussian pulses after simulated propagation. (a) Only normal dispersion is affecting the pulse. (b) Only SPM is affecting the pulse. For each plot, the main area is a spectrogram in logarithmic scale, while the top and right plot represent the temporal, respectively spectral, intensity in a normalized, linear scale.

It is a direct consequence of Fourier mathematics that pulses of finite duration necessarily contain a multitude of spectral components. When traveling through a medium, those components of angular frequency ω propagate at a speed of $c/n(\omega)$, smaller than the speed of light in vacuum c. The refractive index $n(\omega)$ is different for each component, leading to a distortion of the pulse in time.

To study the different regimes of dispersion, the mode-propagation constant β is introduced. It is customary to write it as its Taylor expansion around the pump frequency ω_0:

$$\begin{aligned} \beta(\omega) &= n(\omega)\frac{\omega}{c} = \beta_0 + \beta_1(\omega - \omega_0) + \frac{1}{2}\beta_2(\omega - \omega_0)^2 + \ldots, \\ \beta_k &= \left.\frac{\mathrm{d}^k \beta(\omega)}{\mathrm{d}\omega^k}\right|_{\omega=\omega_0}. \end{aligned} \tag{2.1}$$

The speed at which a pulse envelope travels is the group velocity $v_g = 1/\beta_1$. Therefore, it is natural to define the rate at which different spectral component

spread out in time due to different group velocities as the first derivative of β_1, which is the GVD β_2. This number is sometimes written as the dispersion parameter D:

$$D(\lambda) = -\frac{2\pi c}{\lambda^2}\beta_2, \quad \lambda = \frac{2\pi c}{\omega}, \tag{2.2}$$

where λ is the wavelength in vacuum. Positive β_2 (negative D) is referred to as *normal dispersion* and negative β_2 (positive D) is called *anomalous dispersion*. Fibers that exhibit normal dispersion over their entire design wavelength range are called all-normal dispersion (ANDi) fibers. All other fibers have at least one zero dispersion wavelength (ZDW) where $\beta_2 = 0$.

The length scale over which chromatic dispersion is relevant is the dispersion length L_D:

$$L_D = \frac{T_0^2}{|\beta_2|} \tag{2.3}$$

where, for a Gaussian pulse, $\tau_{\mathrm{FWHM}} = T_0\sqrt{2\ln 2}$ is the full width at half maximum (FWHM) duration of the pulse. A Gaussian pulse broadens by a factor of $\sqrt{2}$ over a propagation length of L_D.

The result of dispersion is illustrated in Fig. 2.1(a). It shows the spectrogram of a Gaussian pulse after a propagation distance of $4L_D$ while experiencing only normal dispersion. As shown by the top and right panels, the positive chirped imparted by the GVD stretches the pulse in time while maintaining its original spectral envelope.

2.1.2 Self-Phase Modulation

On its own, chromatic dispersion can affect the temporal envelope of a pulse, but not its spectral one. On the other hand, SPM will change the spectrum of a pulse without changing its temporal profile. SPM is a consequence of the Kerr effect, a nonlinear response of a material to extreme light intensity. The Kerr effects manifests as an instantaneous change of refractive index Δn proportional to the light intensity I:

$$\Delta n = n_2 I. \tag{2.4}$$

The nonlinear refractive index n_2 is a property of the material proportional to the real part of the third order susceptibility $\chi^{(3)}$. It can be wavelength-dependent [29], although it is considered constant throughout this work.

To understand SPM, let's have a look at the nonlinear Schrödinger equation (NLSE):

$$\frac{\partial}{\partial z}A(z,\tau) = -i\frac{\beta_2}{2}\frac{\partial^2}{\partial \tau^2}A(z,\tau) + i\gamma A(z,\tau)|A(z,\tau)|^2. \tag{2.5}$$

This scalar equation describes how the complex pulse envelope A evolves when under the influence of SPM and second order dispersion. Here, $\gamma \propto n_2$ is the nonlinear parameter [20]. Let's write the pulse envelope A in terms of its magnitude $|A|$ and phase ϕ:

$$A(z,\tau) = |A(z,\tau)|\exp(i\phi(z,\tau)). \tag{2.6}$$

Ignoring GVD ($\beta_2 = 0$), inserting (2.6) in (2.5) yields:

$$\frac{\partial}{\partial z}|A(z,\tau)| = 0, \quad \frac{\partial}{\partial z}\phi(z,\tau) = \gamma|A(z,\tau)|^2. \tag{2.7}$$

With the definition of the instantaneous frequency $\omega_c = -\mathrm{d}\phi/\mathrm{d}t$, it can be shown that SPM creates new frequencies by chirping the middle of the pulse without changing its temporal shape.

The spectral broadening induced by SPM is illustrated on in Fig. 2.1(b). As with the dispersion example, this example starts with an unchirped Gaussian pulse. During propagation, the rising edge of the pulse gets redshifted while the falling edge gets blueshifted. This imparts the characteristic S shape of SPM on the spectrogram. Notice how the temporal envelope is not affected by SPM. Interferences of identical spectral component at different times within one pulse cause an oscillatory pattern on the spectrum. The number of peaks is related to the nonlinear phase shift $\Phi_{\mathrm{NL}} = \gamma P_0 z$, where P_0 is the initial peak power. On Fig. 2.1(b), $\Phi_{\mathrm{NL}} = 6.5\pi$. This leads to a very natural definition of the nonlinear length L_{NL}, the propagation distance required for a nonlinear phase shift of 1:

$$L_{\mathrm{NL}} = \frac{1}{\gamma P_0} \tag{2.8}$$

2.1.3 Solitons

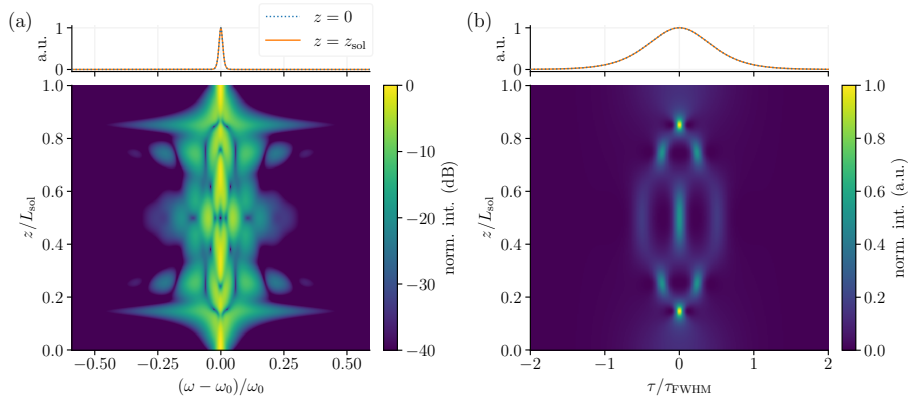

Figure 2.2: Propagation of an $N = 4$ soliton. (a) Spectral evolution in logarithmic scale. The top panel shows identical spectra between $z = 0$ and $z = L_{\mathrm{sol}}$. (b) Temporal evolution in linear scale. As with (a), the top panel shows identical pulses before and after propagation.

When anomalous dispersion and SPM combine, they give rise to soliton dynamics. Solitons are pulses that preserve their shape as they propagate. Not only do they constitute fascinating mathematical curiosities, they also find practical applications, such as in telecommunication [30].

In the context of the NLSE, a *fundamental soliton* is a solution of Eq. (2.5) where the positive, nonlinear chirp induced by SPM is perfectly balanced by the negative chirp induced by anomalous dispersion. To define this solution mathematically, the soliton number N must first be introduced. It is expressed in terms of the dispersion length and the nonlinear length:

$$N^2 = \frac{L_D}{L_{\mathrm{NL}}} = \frac{\gamma P_0 T_0^2}{|\beta_2|}. \tag{2.9}$$

N reflects the balance between nonlinearities and dispersion. If parametrized such that both effect balance out each other ($N = 1$), the following pulse definition is a solution of Eq. (2.5).

$$A(z, \tau) = \sqrt{P_0}\text{sech}(\tau/\tau_0) \exp\left(i\frac{z}{2L_D}\right). \tag{2.10}$$

Notice how the temporal and spectral envelopes of this solution do not depend on z, i.e. the pulse only picks up a constant phase as it propagates. This is only the case for $N = 1$. With higher positive values of N, both the temporal and spectral envelope evolve periodically. Fig. 2.2 shows this phenomenon for an $N = 4$ soliton. The cycle starts with a strong spectral broadening induced by SPM. Because of the anomalous dispersion, the redshifted rising edge is slowed down and the blueshifted falling edge is sped up, thus leading to a temporal compression of the pulse. This initial compression stage occurs for every $N > 1$ and the following periodic evolution of the pulse becomes more intricate with larger values of N.

2.1.4 Optical Wave-Breaking

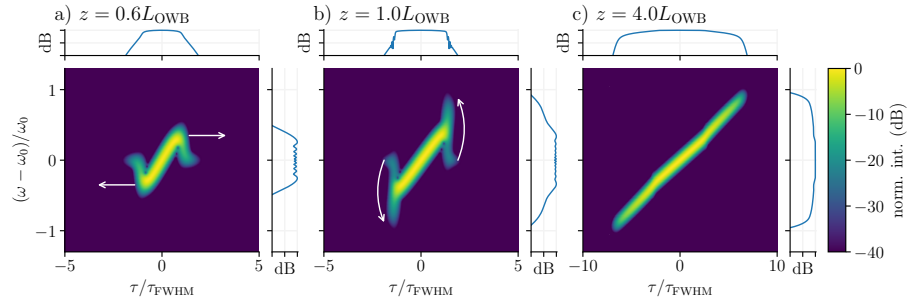

Figure 2.3: Logarithmic scale spectrograms illustrating the OWB process. Top and right panels on each subfigure show the corresponding temporal envelopes, respectively spectrum, at 20 dB/div. scale. (a) Before OWB. (b) During OWB. (c) After OWB.

The SCG mechanism in ANDi fibers can be almost completely explained with only GVD and SPM. These two phenomena are combined in a process called optical wave-breaking (OWB). The length scale of this process is [31]:

$$L_{\text{OWB}} \approx 1.1\frac{L_D}{N}. \tag{2.11}$$

In contrast to anomalous dispersion and soliton dynamics, normal dispersion acts to accelerate the light redshifted by SPM on the rising edge of a pulse and to slow down the blueshifted light on the falling edge. This results in a completely different spectral and temporal evolution of the pulse.

Fig. 2.3 shows spectrograms of the evolution of a Gaussian pulse at 3 key moments of OWB. In Fig. 2.3(a) the arrows highlight the blueshift and redshift of the spectral components produced by SPM. Around $z \approx L_{\text{OWB}}$ (Fig. 2.3(b)), these shifted components begin to overlap and interfere with the extreme ends

of the pulse, as shown by the oscillations in the time domain. There, four-wave mixing (FWM) creates new spectral components, as indicated by the arrows in the figure. Fig. 2.3(c) shows the results of the OWB process, where the spectrum is smooth and normal dispersion stretches it further in time.

2.1.5 Generalized Nonlinear Schrödinger Equation

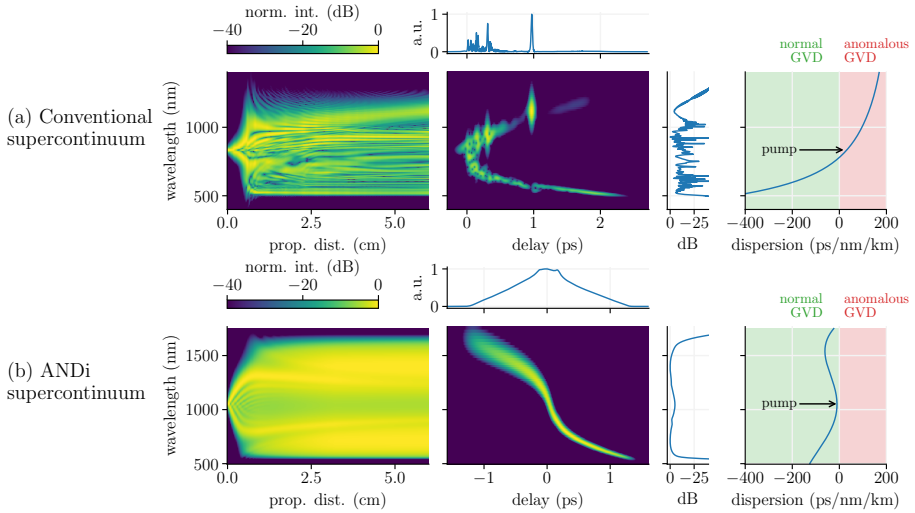

Figure 2.4: Generalized nonlinear Schrödinger equation (GNLSE) simulations of 50 fs pulses using the full generalized nonlinear Schrödinger equation (GNLSE). From left to right: spectral evolution as function of propagation distance; spectrogram at the end of propagation with projections in time (above) and wavelength (right); dispersion of the fiber. (a) Conventional SC generated with $N = 10$ soliton. (b) ANDi SC generated with 52 kW peak power.

To simulate actual SCG experiments, a common equation to use is the generalized nonlinear Schrödinger equation (GNLSE), an equation fundamentally similar to Eq. (2.5), but with a few additions [14]:

$$\begin{aligned}\frac{\partial A(z,\tau)}{\partial z} = &-\frac{\alpha}{2}A(z,\tau) - \sum_{k=2}^{\infty}\beta_k\frac{i^{k-1}}{k!}\frac{\partial^k}{\partial\tau^k}A(z,\tau)\\ &+ i\gamma\left(1+\frac{i}{\omega_0}\frac{\partial}{\partial\tau}\right)A(z,\tau)\int_{-\infty}^{\infty}R(\tau')\,|A(z,\tau-\tau')|\,\mathrm{d}\tau'.\end{aligned} \tag{2.12}$$

Linear effects are expressed in the first line of the right-hand side (RHS) while all nonlinear effects are grouped in the second line. On top of GVD already present in the NLSE, arbitrarily high order dispersion can be included, as well as linear loss through the attenuation coefficient α.

Because of the Kerr effect, the peak of a pulse will experience a higher effective refractive index than its edges and will start to lag compared to the rest of the pulse. The term $\frac{i}{\omega_0}\partial/\partial\tau$ accounts for this effect. Finally, the instantaneous effect of SPM, represented as the Dirac delta $\delta(\tau)$, is grouped together

with delayed Raman scattering, represented as $h_R(\tau)$, in the response function $R(\tau) = (1 - f_R)\delta(\tau) + f_R h_R(\tau)$. The fractional contribution of each effect is tuned with the parameter $0 \leq f_R \leq 1$.

In the anomalous dispersion regime, these added effects perturb solitons when they reach their maximum compression. This leads to *soliton fission*, where a high order soliton breaks into a train of fundamental solitons. When the fiber is pumped close to its ZDW in the anomalous regime, phase matching in favorable to the creation of DWs in the short wavelength side of the spectrum. At the same time, Raman scattering is responsible for the redshifting of solitons. Fig. 2.4(a) shows an example of such SCG. The spectral evolution plot shows the initial spectral broadening caused by SPM. At the point of maximum compression, soliton fission occurs, from which a highly complex spectrum emerges. Propagation is prolonged for a few more cm to show Raman scattering redshifting a soliton on the long wavelength side of the spectrum. The spectrogram gives more insight into the structure of the SC after 6 cm of propagation.

When using an ANDi fiber, the SCG process is dominated by normal GVD and SPM. Therefore, the other effects mentioned above have little influence, resulting in the smooth and flat SC shown on Fig. 2.4(b).

In practice, the Fourier transform of Eq. (2.12) is the equation solved by the simulation program. By working in the frequency domain rather than in the time domain, computations of time derivatives are trivial and inclusion of a frequency-dependence in the attenuation coefficient or the nonlinear parameter is easier [32]. The equation is integrated using a Runge-Kutta method in the interaction picture. This implies splitting the RHS of Eq. (2.12) into a linear operator (first line) and a nonlinear operator (second line), which can be separately applied according to the specific integration scheme. Simulations in Chapter 3 are performed using a straightforward 4th order Runge-Kutta scheme [33] with adaptive step size controlled by photon number conservation [34]. Simulations in Chapters 4 and 5 are carried out using an embedded Runge-Kutta method of 4th and 3rd order [35]. Simulation code was written in Python for the purpose of this thesis and makes heavy use of Numpy [36], SciPy [37] and Matplotlib [38].

2.2 Noise in Supercontinuum Generation

This section is part of a published article [12].

The noise properties of SC sources can be understood in terms of a competition between coherent and incoherent nonlinear processes. Low-noise and phase-coherent SC can be generated in the normal dispersion regime under a wide range of conditions when SPM and OWB dominate [39], or in the anomalous dispersion regime when soliton fission dominates, i.e. using pump pulses with very short durations and low soliton numbers [14]. However, these coherent dynamics can be disturbed by incoherent nonlinear effects, which can build up new spectral components from quantum noise and whose influence grows with longer pump pulse durations [14].

Examples of this noise amplification are illustrated in Fig. 2.5 showing SC generated by (a) FWM-induced modulation instability (MI) and (b) SRS. Both nonlinear effects generate gain bands spectrally separated from the input pulse

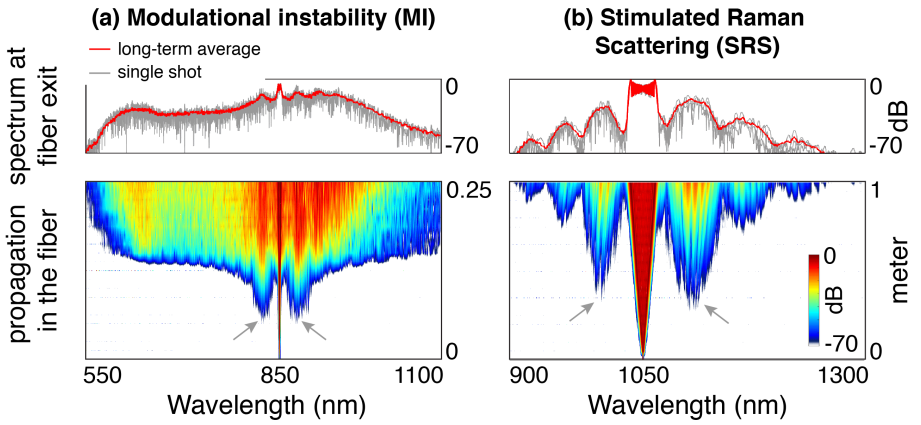

Figure 2.5: Origin of SC noise. Simulated spectral evolution of 5 ps, 5 kW pulses in (a) conventional and (b) ANDi fiber On top, the mean spectrum is displayed in red, obtained from averaging 20 simulations with random noise seeds. Gray traces show single shot spectra. Arrows indicate primary gain bands for amplification of quantum noise.

spectrum, providing enormous exponential gain to any seed signal injected into these bands. When this gain remains unseeded, as in these examples, then random quantum fluctuations serve as the seed and are amplified to become significant and eventually dominate the nonlinear dynamics. The noise-seeded spectral components contained in the MI and SRS peaks exhibit random fluctuations in amplitude and phase from shot to shot and are thus incoherent with the pump. With further propagation, cascaded Stokes (redshifted) and anti-Stokes (blueshifted) gain bands emerge and eventually distribute noise throughout the SC pulse. Similar noise amplifying nonlinear effects exist when coherent and incoherent mode coupling between the two principal polarization axes of a fiber is considered.

2.2.1 Noise Control by Dispersion Engineering

In order to develop strategies for controlling the stability of SC sources, it is helpful to compare the strength of coherent and incoherent nonlinearities and their dependence on the fiber dispersion profile. The strength of coherent nonlinear dynamics is only weakly dependent on the dispersion regime, as can be concluded from the almost identical expressions for the characteristic length scales of soliton fission and OWB [31, 40]. Therefore, the noise properties of a particular SC source are mainly determined by the gain of incoherent nonlinear effects dominated by MI and SRS. Traditionally, these incoherent dynamics have been treated separately, depending on the fiber dispersion regime; MI is regarded as a dominating mechanism of decoherence in anomalous dispersion [41]. In normal dispersion, MI is usually suppressed, and SRS is considered the predominant effect [42]. Here we provide a different, more comprehensive perspective on noise amplification in nonlinear fiber optics that allows us to unveil the significant potential for control and suppression of noise provided by the well-known concepts of dispersion engineering in specialty optical fibers.

Since the seminal work of Bloembergen and Shen[43], it is known that a nonlinear coupling of SRS and FWM occurs in the regime of low dispersion and high nonlinearity, i.e. exactly in the conditions relevant to SC generation. In a single-mode fiber, the interaction between these two nonlinear processes can be described by the mixed parametric Raman (MPR) gain [44], written as:

$$g_{\mathrm{MPR}} = 2\gamma\,\Re\left(\sqrt{K(2q-K)}\right), \tag{2.13}$$

where $K = -\beta_2\Omega_R^2/(2\gamma P_0)$ describes the ratio of chromatic dispersion and nonlinearity, peak angular frequency shift of the Raman gain Ω_R, and pulse peak power P_0. The factor $q = (1-f_R) + f_R\chi_R^{(3)}(-\Omega_R)$ contains the Raman susceptibility $\chi_R^{(3)}$ and fractional contribution f_R (~ 0.18 for silica) of the Raman effect to the total nonlinear response of the fiber material. Fig. 2.6 shows g_{MPR} for a silica fiber as a function of K, normalized to the standard Raman gain coefficient $g_R \simeq 0.5\gamma$.

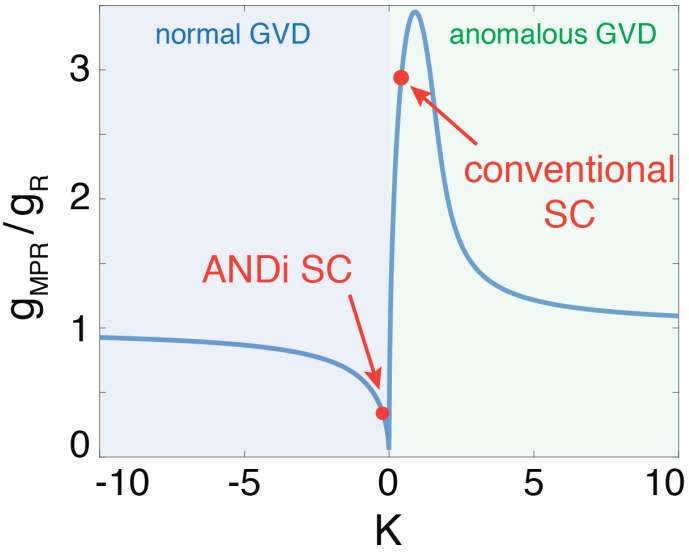

Figure 2.6: MPR gain g_{MPR}, Eq. (2.13), normalized by the standard Raman gain g_R. We use the MPR gain to describe the dispersion dependence of noise-amplifying incoherent nonlinearities in SC generation dynamics. Typical conditions for octave-spanning SC generation for ANDi and conventional SC from Fig. 2.4 are indicated.

Eq.(2.13) describes an explicit dependence of the Raman gain on chromatic dispersion and nonlinearity, and its validity in nonlinear fibers has been experimentally verified [45, 46]. However, so far its implications for the control of nonlinear noise amplification by engineering the fiber dispersion profile have not been fully realized. While our recent work has shown the important role of the MPR gain for the noise properties of ANDi SC [39], we believe that it can in fact be applied more universally to explain the observed noise properties of SC generated in both dispersion regimes. In Fig. 2.6 (c), mainly the region $|K| < 1$ is relevant to SC generation, where we observe a strong suppression of the MPR

gain in normal dispersion, while MPR noise-amplification is strongly amplified in the anomalous dispersion region. The peak of the MPR gain is located at $K \simeq 1 - f_R/2$, where Stokes and anti-Stokes Raman sidebands are effectively amplified by MI, whose role in the coherence collapse of conventional SC has been investigated since the early days of fiber-based SC generation [16, 41]. When we consider the typical conditions for octave-spanning SC generation, we find that the MPR gain and associated noise amplification can be decreased by over one order of magnitude by changing from the conventional to the ANDi fiber design. In fact, this order of magnitude difference in noise susceptibility is a recurrent factor found in many theoretical and experimental studies, as we detail below, and can be seen as the main reason behind the attraction of ANDi fibers for low-noise SC source development.

From this fundamental physics perspective, we expect ANDi SC to be significantly more stable than conventional SC. Detailed numerical and experimental studies have confirmed this expectation. The competition between the coherent and incoherent dynamics typically leads to a threshold pulse duration T_{crit} or threshold soliton number N_{crit} above which the nature of the SC changes from coherent to incoherent [14, 21]. The ANDi fiber design exhibits about 10x higher T_{crit} and 50x higher N_{crit} than its conventional counterparts for octave-spanning bandwidths [39]. The superior coherence and noise properties of ANDi SCs over conventional SCs were verified, for example, by measurements of RIN, spectral coherence, dispersive Fourier transformation, and RF beating with stabilized laser diodes [47–49]. ANDi SC also possess a remarkable resistance against technical pump laser fluctuations [24, 50, 51], while conventional SCs amplify such fluctuations by up to 20 dB, even in the regime where coherent dynamics dominate [15]. Describing incoherent nonlinear dynamics in terms of the MPR gain is therefore a successful concept for explaining the superior stability of ANDi SC. It also provides a new perspective on the considerable potential for noise control in nonlinear fiber optics. A future challenge will therefore lie in the development of new fiber designs specifically tailored for low-noise operation in a variety of nonlinear frequency conversion applications.

2.2.2 Noise Control by Designing Fiber Geometry and Birefringence

Every fiber exhibits a certain amount of birefringence that breaks the degeneracy of polarization modes. Birefringence might be induced unintentionally by unavoidable external stresses or bending of the fiber, or it can be engineered, e.g. by including stress rods or asymmetries into the design of the fiber cross-sectional geometry. The coherent and incoherent coupling of the fiber's polarization modes leads to several nonlinear effects that, in addition to the MPR gain, have the potential to amplify quantum noise and result in unpredictable fluctuations of the polarization state. In the context of ANDi SC sources especially relevant are polarization modulation instability (PMI) [55, 56], cross-phase modulation instability (XMI) [57, 58], and Raman amplification assisted by cross-phase modulation [59, 60].

In general, the occurrence of noise amplification is a complex function of fiber birefringence and dispersion, as well as relative orientation of input pulse polarization and fiber axes. On Fig. 2.7, we present preliminary results of high resolution polarization-dependent RIN measurements visualizing this complex-

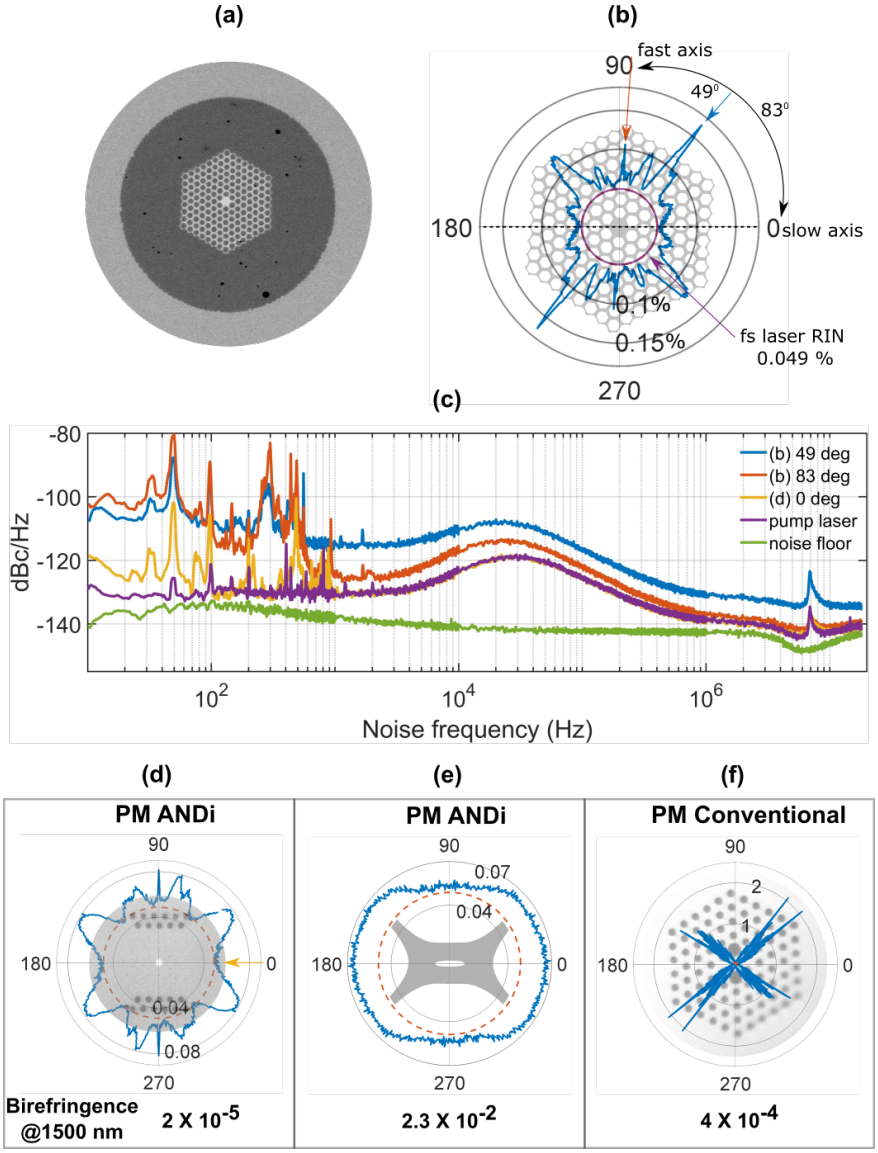

Figure 2.7: Noise fingerprints of various ANDi SC (a-e) and conventional SC (f) pumped by an Er:fiber laser (80 fs, 40 MHz) at 1550 nm, generating comparable bandwidths in the range 1.2-2.2 μm. (a) Microscope image of low-birefringence all-solid ANDi PCF [52]. (b) Integrated RIN values (in %) of SC generated in fiber (a) shown in a polar plot in dependence of pump pulse polarization orientation. Corresponding orientation of the fiber geometry shown in background. The fiber's slow axis is aligned to zero degrees. The red-dotted line shows the RIN of the pump laser (0.05%). (c) Detailed noise spectra in a range 10 Hz–20 MHz for positions 48^o and 83^o (fast axis) of noise fingerprint in (b), and position 0^o (slow axis) of noise fingerprint in (d). Pump laser noise and detection noise floor shown for comparison. (d) Noise fingerprint of SC generated in silica polarization-maintaining (PM) air-hole microstructured PCF [53], (e) nanohole suspended-core ANDi fiber[54], and (f) commercial conventional fiber NKT PM-1550-01.

ity. For these measurements, pulses from an ultrafast Er:fiber laser (80 fs, 40 MHz, 0.05% RIN) were coupled into ANDi fibers with similar dispersion profiles, but very different geometries and birefringence, generating SC with comparable spectral bandwidths in the range 1.2 – 2.2 μm. A rotating half-wave plate in front of the fiber and a synchronized analyzer at the fiber exit control the plane of pump pulse and detection polarization with respect to the fiber geometry. Polarization-dependent RIN values are measured with an angular resolution of approximately 0.2^o using a photodiode and electronic spectrum analyzer and visualized in polar plots. These plots were found to be unique for each tested fiber and are therefore referred to as "noise fingerprints".

These measurements reveal a strong correlation between the nonlinear noise amplification and the cross-sectional geometry of a particular fiber, which we attribute to the unique stress profile associated with each fiber structure and its drawing conditions. The ANDi fiber in Fig. 2.7(a, b) is designed as an all-solid microstructured PCF made from two different soft glasses forming the photonic lattice and inclusions. The structure causes a complex stress pattern due to different thermal expansion coefficients of the two glasses. Since there is no intentional stress axis defined in this design, the resulting birefringence is random and the polarization axes are not well-defined, evident by the 83^o angle measured between the axes. The complex stress profile is also reflected in the highly polarization-dependent nonlinear noise amplification pattern, which we found to be highly susceptible to environmental disturbances, such as bending the fiber, different clamping conditions, or day-to-day temperature changes.

Since for each angular RIN measurement a full noise spectrum is available, we can identify the underlying noise amplification process for every feature of the fingerprint by analyzing its characteristic noise frequencies (Fig. 2.7(c)). For example, at 49^o the noise spectrum of the SC is shifted upward in comparison to the pump laser due to a significant contribution of excess white noise, which is a characteristic signature of quantum noise amplification, and can therefore be attributed to the occurrence of XMI and PMI. Near the fast axis, on the other hand, we mainly observe low-frequency noise, which indicates polarization instability caused by the cancellation of the small linear fiber birefringence by the nonlinear Kerr effect. In general, we observe a complex superposition of these effects.

Fig. 2.7 also illustrates that birefringence is an effective control parameter to reduce polarization-dependent noise in ANDi SC generation. With increasing birefringence the noise fingerprints become more regular and environmentally stable, as shown for the airhole-microstructured silica PCF with Germanium-doped core in Fig. 2.7 (d). Near the slow axis (0^o) of this fiber the noise spectrum is virtually identical to the noise of the pump laser (Fig. 2.7(c)), while we continue to observe a strong correlation of noise features and fiber geometry for off-axis pumping. Eventually, we observe complete suppression of noise-amplifying nonlinear processes for extremely birefringent ANDi fiber designs, such as the nanohole suspended core fiber in Fig. 2.7 (e), even when the pump polarization is not aligned to one of the principal fiber axes. In contrast, the noise fingerprint of a comparable polarization-maintaining conventional SC source (Fig. 2.7(f)) is significantly more complex, and shows noise amplification up to a factor of 40. In the test conditions the soliton number is $N \simeq 6$, such that a stable SC is generated when the polarization of the pump pulses is exactly

aligned to a principal axis of the fiber. However, even slight misalignment of the polarization in the order of just 1^o causes a significant rise of the SC noise.

These measurements highlight the importance of the cross-sectional fiber geometry and the homogeneity of the stress profile, in addition to dispersion engineering, for the realization of high-quality, low-noise SC sources. ANDi SC sources designed with these considerations in mind are currently emerging also for other pump wavelengths, providing further experimental evidence for the excellent quality and stability of these broadband coherent light sources [26].

Chapter 3

Hybrid Fibers for Low-Noise Supercontinuum Generation

Parts of this chapter were published in [61] and [62]. Experimental work was conducted in close collaboration with Anupamaa Rampur and Pascal Hänzi, and I led the work on numerical simulations and interpretation of the results

A major challenge in current nonlinear optics research is the development of ultra-low noise broadband coherent SC light sources. Equipped with the brightness of a laser and ultra-broad spectral bandwidths, SC sources based on specialty optical fibers are today an indispensable tool in many scientific and industrial processes [23, 63]. However, for many applications in advanced spectroscopy, microscopy, and ultrafast photonics, the noise of current SC sources has become the predominating factor limiting acquisition speed, sensitivity, or resolution [12]. Significant research efforts are also directed towards understanding the fundamental noise limits of the involved nonlinear spectral broadening dynamics, with continued interest in the development of optical frequency comb technology not only for metrology and spectroscopy [64, 65], but increasingly also for emerging applications in coherent optical communications, microwave photonics, and photonic signal processing [66–68], where ultra-low amplitude- and phase-noise performance is an essential prerequisite.

The predominating noise source during the nonlinear transformation of a narrowband input into a broadband SC spectrum in an optical fiber is the amplification of random quantum fluctuations by incoherent nonlinear effects, which either have a scalar character, such as MI or SRS [14, 16, 42], or a vectorial nature emerging from a coupling of the two orthogonal eigenmodes of the fiber, such as PMI [56, 69]. The occurrence and strength of these processes depend critically on the dispersion and birefringence engineering of the fiber, as well as on the characteristics of the input pulse. Therefore, a considerable effort has been directed towards identifying fiber designs that favor highly coherent spectral broadening dynamics.

Typically, there is a trade-off to be considered when engineering the dispersion landscape of nonlinear fibers. On one hand, recent advances in specialty

optical fiber design and fabrication have facilitated the emergence of a new generation of highly birefringent, polarization-maintaining (PM) ANDi fibers, which are designed to suppress both scalar and vectorial noise-amplifying incoherent nonlinear effects under sub-picosecond pumping [12, 63]. As additional benefit, the nonlinear dynamics are dominated by optical wave-breaking, which is capable of simultaneously delivering low noise, octave-spanning bandwidth, superb spectral flatness, high spectral power densities, and single-cycle temporal waveform support [70]. This new class of SC sources has driven recent advancements of the state-of-the-art in several applications which so far were either not able to use or were limited by conventional fiber SC sources due to their noise or complex spectra and pulse shapes, e.g. in hyperspectral and multimodal imaging, near-field optical microscopy, optical coherence tomography at the shot-noise limit, and ultrafast photonics [13, 71–78].

On the other hand, SC noise is reduced and coherence improved by shorter input pulse durations in any fiber design [14, 39]. Here, anomalous dispersion fibers have a clear advantage as they benefit from an initial stage of soliton compression dynamics, which shorten the injected pulse to a fraction of its initial duration and increase its peak power by up to one order of magnitude before the actual spectral broadening dynamics set in [40]. Hence, conventional SC sources require significantly lower input peak power than ANDi SC sources for the generation of equal spectral bandwidths, and consequently are often the only choice for the nonlinear spectral broadening of lasers with repetition rates of hundreds of megahertz or gigahertz, where the peak power per pulse is limited. Unfortunately, the subsequent soliton-fission dynamics produce rather complex spectral and temporal profiles, and the anomalous dispersion environment provides strong amplification for incoherent nonlinear processes [12].

Inspired by early works with dispersion-flattened and dispersion-decreasing fibers [21, 79], in this article we combine the benefits of nonlinear dynamics in both dispersion regimes, i.e. soliton compression and optical wave-breaking, resulting in an ultra-low noise fiber SC source covering the 930 - 2130 nm range with a spectrally resolved RIN as low as 0.05 % and averaging 0.1 % over a bandwidth of 750 nm. The source is based on a standard ultrafast Er:fiber laser seeding cascaded nonlinear dynamics in two discrete, widely available commercial PM step-index fibers. The individual fibers exhibit anomalous and all-normal dispersion at the pump wavelength, respectively, and are joined together by a low-loss fusion splice to form a hybrid fiber. We show that this hybrid approach not only doubles the generated spectral bandwidth, but also decreases the RIN by up to one order of magnitude compared to direct pumping of the individual fibers. Our measurements reveal that PMIs set a lower limit to the RIN of the directly pumped ANDi SC source, while these dynamics are suppressed in the hybrid fiber such that the SC noise approaches the theoretical limit determined by the noise and pulse shape of the pump laser. We also compare SCG via OWB in this hybrid fiber with two other hybrid fibers that use conventional SCG and find that adding a pre-compression stage in this latter case provides little benefits.

3.1 Methodology

3.1.1 Hybrid Fiber Preparation

The fibers used in this work are two commercial PM step-index fibers produced by Coherent-Nufern, namely PM1550-XP and PM2000D, which exhibit anomalous and all-normal chromatic dispersion at the pump wavelength of 1560 nm, respectively, as shown in the inset of Fig. 3.1 [80]. PM1550-XP has a core-diameter of 8.5 µm and numerical aperture of 0.125, resulting in a zero-dispersion wavelength of 1.34 µm and dispersion parameter $D = 18\,\mathrm{ps/(nm\,km)}$ at 1560 nm. In contrast, the small 2.1 µm diameter core, high NA of 0.37, and highly Germanium (Ge)-doped core material composition of PM2000D were specifically designed to exhibit flat and normal dispersion over the entire near-IR spectral region, with $D = -46\,\mathrm{ps/(nm\,km)}$ at 1560 nm. Both fibers are PANDA-type PM fibers, with birefringence values at the pump wavelength of 3×10^{-4} given by the manufacturer for PM1550-XP, and 2×10^{-5} measured in-house for PM2000D.

In order to exploit cascaded nonlinear dynamics in both fibers, a low-loss fusion splice is an essential requirement, but due to the large core diameter and NA mismatch, losses in the order of 4 dB are to be expected when using a standard splicing recipe. Better results can be obtained with the thermally expanding core technique [81]. Owing to the high Ge content of the PM2000D core material, long arc durations lead to thermal diffusion of Ge from the core to the cladding region, which gradually increases the mode field diameter in the hot zone and thus reduces the splice loss. By monitoring the transmission of a 1550 nm continuous-wave laser in real-time during the splice, we reach a minimum splice loss of 0.7 dB (85 % transmission) with an arc time of 14 s. The splice is executed simply by modifying the arc duration of the standard PM single-mode program of a Fujikura FSM45+ fusion splicer and using auto-alignment of the polarization axes.

3.1.2 Experimental Setup

The experimental setup used to generate and analyze the SC is shown in Fig. 3.1. An ultrafast Er:fiber laser (Toptica FemtoFiber pro) centered at 1560 nm delivers a 90 fs pump pulse train with 40 MHz repetition rate, RIN of 0.05% (measured in the frequency range 100 Hz − 20 MHz), and polarization extinction ration (PER) of 30 dB. A half-wave plate is used to align the polarization state of the input pulses to the fiber's principal birefringence axes. The pump pulses are coupled into the fiber under test (FUT) by an aspheric lens with focal length chosen to match the mode field diameter of the fiber, resulting in a maximum coupled average power of 210 mW. This corresponds to a peak power of 33 kW, calculated using the real pulse shape emitted by the laser measured by time-domain ptychography. The generated SC spectra are recorded using two optical spectrum analyzers (Yokogawa AQ6370 for $\lambda < 1700$ nm and AQ6375 for $\lambda > 1700$ nm). A polarizer is inserted in the beam path in order to analyze the PER of the SC, and also serves for converting possible polarization state fluctuations into amplitude noise that can be detected using the subsequent RIN measurement system.

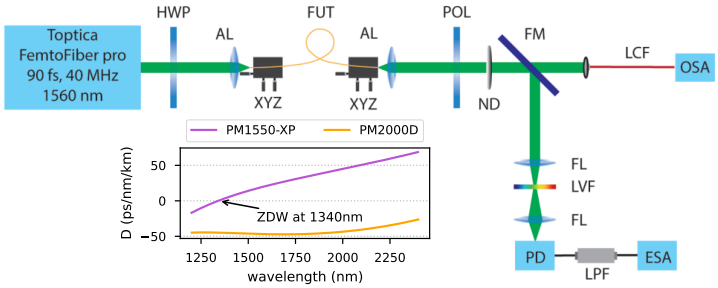

Figure 3.1: Schematic setup for supercontinuum generation and RIN Measurement. HWP: Half wave plate; AL: Aspheric lens; XYZ: Three axis translation stage; FUT: Fiber under test; POL: Polarizer; ND: Neutral density filter; FM: Flip mirror; LCF: Large core fiber patch cord; OSA: Optical spectrum analyzer; FL: Focusing lens; LVF: Linear variable filter 1.3 µm - 2.6 µm; PD: Photo diode; LPF: Low pass filter ($<$ 21 MHz); ESA: Electronic spectrum analyzer. The inset shows the measured chromatic dispersion of the fibers used in this experiment.

3.1.3 RIN Measurement

The spectrally resolved intensity noise is measured by passing the SC through a linear variable bandpass filter with 20 nm bandwidth covering the range 1300 - 2600 nm (Vortex Optical Coatings, UK) and analyzing the resulting pulse train with an amplified photodiode (Thorlabs PDA10D2, bandwidth DC - 25 MHz, 900 - 2600 nm spectral range, 5 kV/A transimpedence gain) connected to an electronic spectrum analyzer (ESA) (Signal Hound USB-SA44B, bandwidth 1 Hz - 4.4 GHz). Additional discrete bandpass filters with similar bandwidths cover the shorter wavelengths below 1300 nm. The photodiode signal is filtered by a 21 MHz low-pass filter to avoid saturation of the ESA at the pulse repetition rate as well as a DC block capacitor with cut-off frequency < 3 Hz. The DC level of the voltage signal (V_0) and the voltage noise PSD $S_V(f)$ [V^2/Hz] are measured, so that the RIN PSD can be obtained by $S_{\mathrm{RIN}}(f) = S_V(f)/V_0^2$ [1/Hz] because the measured voltage V is proportional to the optical power P. The root mean square (RMS) optical intensity fluctuations in percent are then given by the square root of $S_{\mathrm{RIN}}(f)$ integrated from 100 Hz up to the Nyquist frequency of 20 MHz. This value is used in this manuscript when integrated RIN values are referenced.

3.1.4 Simulations

Simulations are carried out using the single mode GNLSE using the integration scheme presented in [34]. Nonlinear effects such as Kerr-induced SPM, self-steepening and delayed Raman effect (as modeled in [82]) are included and the angular frequency dependent nonlinear parameter $\gamma(\omega)$, as formulated in [32], relies on an approximation of the effective mode-field area [83]. A single mode scalar equation implies that polarization effects are ignored, but this approximation is tolerable since only PM fibers are considered. Finally, the shortness of the fibers in use allows us to neglect any kind of loss in all the simulations.

Quantum shot noise is simulated by adding one photon of random phase per frequency bin at the input [84] whereas RIN is simulated by multiplying the intensity of the measured laser field by $1 + \psi$ for each simulation, where ψ is sampled on a normal distribution of mean 0 and standard deviation 0.057 %, which is the measured laser RIN After simulating the propagation of 40 pulses $A_i(\lambda)$, $i = 1, ..., 40$, we compute the RIN as a function of the wavelength λ in a way similar to that used in the experiment, masking the spectra with a Gaussian window and working out the coefficient of variation of the remaining energy :

$$\begin{aligned} \mathrm{RIN}(\lambda) &= \frac{\sqrt{\left\langle \left(E_i(\lambda) - \langle E_j(\lambda)\rangle_j\right)^2 \right\rangle_i}}{\langle E_i(\lambda)\rangle_i} \\ E_i(\lambda) &= \int_{-\infty}^{\infty} |A_i(\lambda')|^2 \exp\left[\left(\frac{\lambda' - \lambda}{\lambda_0}\right)^2\right] \mathrm{d}\lambda' \end{aligned} \tag{3.1}$$

where $\langle\,\rangle_i$ denotes the ensemble average over the 40 simulations and $\lambda_0 = 12.02\,\mathrm{nm}$ corresponds to a window width of 20 nm at half maximum. As consequences of this method, the input RIN is assumed to be frequency-independent and is modeled only between 1 MHz and 20 MHz. This is nevertheless adequate because the measured RIN spectrum is nearly flat in this frequency range and accounts for $> 90\,\%$ of the total measured RIN.

After the splice, the hybrid fiber is cleaved such that it consists of a 6.2 cm length of PM1550-XP at the input followed by 20 cm of PM2000D, where in the former soliton compression and in the latter optical wave-breaking dynamics are exploited. Hence, the length of PM1550-XP is of particular importance in our approach and was carefully optimized using the numerical pulse propagation simulations and experimental time-domain ptychography measurements summarized in Fig. 3.2 [70, 85]. In the fiber, the 110 fs, 32 kW, 40 MHz input pulse supplied by the Er:fiber laser forms a soliton of order $N = 4.3$ that temporally compresses until soliton fission around 6.5 cm breaks it up into its fundamental constituents. The optimized fiber length is chosen such that the resulting pulse is as short as possible while avoiding soliton fission. Fig. 3.2 (b) and (d) show the simulated compressed pulse with 15.9 fs FWHM and the corresponding spectrum, respectively, using the final fiber length of 6.2 cm. Both results are in excellent agreement with the experimental TDP measurements done using a separately prepared PM1550-XP fiber of equal length. The input pulses are therefore compressed by a factor of 7 while the peak power increases by a factor of about 5.3 to 170 kW, with the remaining energy distributed in a low-level pedestal typical of soliton compression. We also note that increasing the fiber length beyond the point of soliton fission does not significantly increase the spectral bandwidth in this case, as shown in Fig. 3.2 (c), apart from the formation of a DW around 1 µm wavelength.

We analyze the stability of the compressed 16 fs pulse train by recording the amplitude noise frequency spectrum from 100 Hz up to the Nyquist frequency of 20 MHz with an ESA. It is indistinguishable from the noise spectrum of the driving Er:fiber laser, as shown in Fig. 3.2 (e), the integrated RIN is 0.06 % in both cases. Hence, the substantial temporal compression and peak power amplification is obtained without incurring any noise penalty. We note that spectrally resolved RIN measurements reveal locally increased RIN up to 0.52 %,

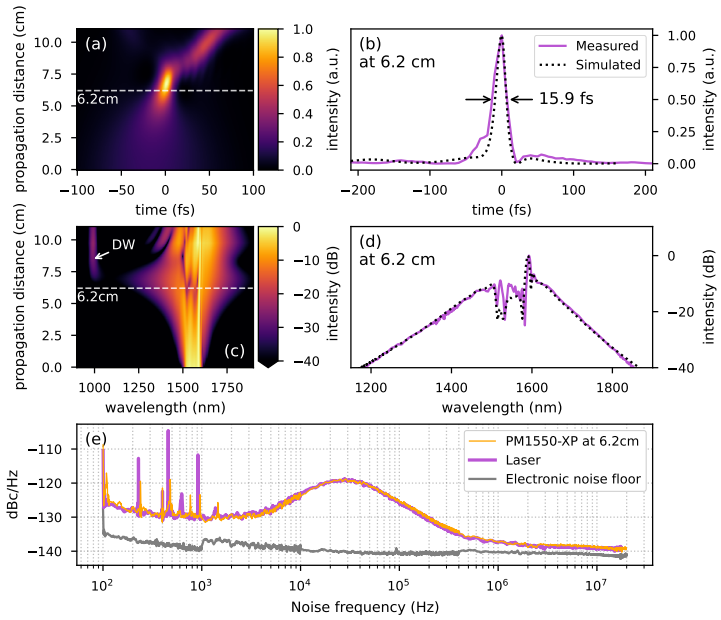

Figure 3.2: Soliton compression in the PM1550-XP fiber pumped with 110 fs, 32 kW input pulses. (a) Simulated temporal intensity profile as function of propagation distance. (b) Simulated (dashed) and measured (solid) pulse shape at 6.2 cm. The measured pulse is recorded after propagating through dispersive elements (thin lens and half-wave plate) and therefore slightly longer (20.6 fs). (c) Simulated spectral evolution; DW: dispersive wave. (d) Simulated (dotted) and measured (solid) spectra at 6.2 cm. (e) Frequency resolved noise measurements of the injected pump and the compressed soliton pulse trains.

but this is less relevant for our purposes since spectral filtering also modifies the temporal characteristics of the pulse.

3.2 Supercontinuum Generation and Relative Intensity Noise

3.2.1 Extension of Spectral Bandwidth

Fig. 3.3 compares the SC spectra generated in the hybrid fiber and the directly pumped PM2000D ANDi fiber. Both measurements were obtained with a coupled pump peak power of 33 kW supplied by a 110 fs Er:fiber laser at 40 MHz repetition rate and with similar overall fiber lengths. The hybrid approach increases the generated -30 dB spectral bandwidth from 76 THz to 183 THz by a factor of $2.4 \simeq \sqrt{5.3}$, which agrees well with the theoretically expected scaling of the SC spectral bandwidth with the square-root of the peak power [70]. The hybrid fiber SC covers the range 930 - 2130 nm while maintaining the typical smooth shape of a SC generated predominantly by optical wave-breaking. The spectral modulation around the pump wavelength, observed in both fibers, can

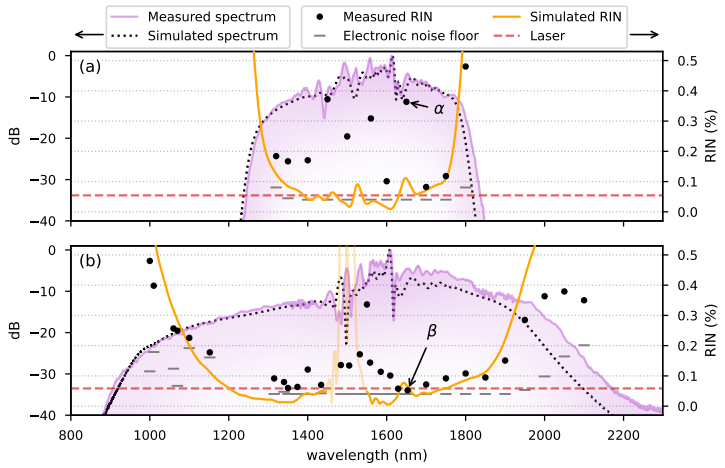

Figure 3.3: Supercontinuum spectra and spectrally resolved RIN in (a) directly-pumped ANDi fiber and (b) hybrid fiber for equal pumping conditions and similar fiber lengths. Left scale: measured (solid) and simulated (dotted) spectra; right scale: spectrally resolved measured RIN (dots) with corresponding electronic noise floor (-) and simulated values using scalar GNLSE simulations (solid yellow). The RIN of the pump laser is indicated by a red-dashed line. Detailed noise-frequency spectra of the RIN measurements at 1650 nm, marked α and β, are shown in Fig. 3.4.

be traced back to low-level temporal sub-structures of the pump pulses emitted by the Er:fiber laser [86]. Both spectra can be reproduced very well with numerical simulations based on the GNLSE, shown in the same Figure.

3.2.2 Reduction of Relative Intensity Noise

The spectrally resolved RIN of both SC is measured by isolating 20 nm sections of the respective spectrum with variable bandpass filters and using an ESA-based detection system sensitive to amplitude and polarization state fluctuations. The results are displayed in Fig. 3.3. We note that both spectral bandpass and polarization filters are important to fully characterize the SC stability. As the intensity noise of SC sources is typically anti-correlated across the spectrum [49, 87], omitting these filters conceals the noise features discussed below by averaging fluctuations of anti-correlated portions of the spectrum leading to lower apparent RIN values. For this reason, our measurements are not directly comparable to studies that did not implement this spectral and polarization selectivity.

For each measured RIN value in Fig. 3.3 the electronic noise floor of the detection system is also displayed so that it can be easily determined whether the detected fluctuations truly stem from the SC pulse train or are limited by the noise of the measurement apparatus. We obtain a typical electronic noise floor of 0.04 % RIN (or -140 dBc/Hz at high Fourier frequencies). This is higher than typically used for ultrafast laser characterization, because we tuned the system not for high sensitivity at the peak wavelength, but for providing a

similar noise floor over as much spectral bandwidth and signal levels as possible. Nevertheless, in most cases the electronic noise floor is sufficiently low to fully resolve the SC noise. We also compare the measured RIN levels to corresponding values retrieved from the scalar GNLSE simulations including quantum noise and technical pump laser fluctuations [50].

Surprisingly, the SC generated in the directly pumped PM2000D ANDi fiber exhibits elevated noise levels especially in the central section of the spectrum between 1400-1700 nm, where RIN values up to 0.4 % are detected. While this is in range with the lowest RIN values reported to date for PM-ANDi SC sources [26], in our case it corresponds to an order-of-magnitude amplification of the pump laser noise, which is unexpected for this fiber design. Importantly, the measured noise levels in the spectral center cannot be reproduced using scalar GNLSE simulations, which predict much lower RIN on the level of the pump laser noise. However, below 1400 nm and particularly above 1700 nm the simulations model the measured noise evolution more accurately, and also reproduce well the increasing RIN on the spectral edges due to the effect of laser peak power fluctuations on the SC bandwidth. This variation in simulation accuracy over the spectral range points towards the presence of incoherent nonlinearities with vectorial nature in the central part of the spectrum, since noise amplification emerging from the nonlinear coupling of polarization eigenmodes is ignored in the scalar numerical model. A more detailed analysis of the origin of the elevated RIN is provided in Section 3.2.3.

In contrast, the intensity noise of the SC generated in the hybrid fiber is significantly lower and in general exhibits an exceptionally low variation with wavelength. The RIN follows very closely the values predicted by the scalar GNLSE simulations and remains mostly confined between 0.05 % and 0.2 % in the range 1150 - 1900 nm, with an average value of approx. 0.1 %. This is quite remarkable when compared to SC generated under very similar pumping conditions in the anomalous dispersion region of a fiber, where the intensity noise varies over at least two orders of magnitude and reaches several percent [87]. The RIN measured in our experiments is also up to one order of magnitude lower than previously reported values obtained from stand-alone ANDi SC sources [26, 51, 88]. Higher noise only occurs at the spectral edges and in the vicinity of sharp spectral features, where small spectral shifts induced by peak power fluctuations lead to a relatively large change in SC signal. The exact spectral position of these features is hard to simulate since they sensitively depend on low-level temporal sub-structures of the input pulse interfering with spectral components generated by SPM [86]. Hence, in Fig. 3.3 (b) the simulated RIN is faded around 1500 nm where the agreement of simulated and measured SC spectrum is less accurate. The intensity noise around these features is not linked to quantum noise amplification by incoherent nonlinearities, but simply arises from the sensitivity of coherent dynamics to the input pulse parameters. Significant additional noise reduction can therefore only be achieved by improving the noise characteristics and the pulse shape of the pump laser.

3.2.3 Suppression of Polarization Modulation Instability

A significant advantage of the ESA-based noise detection over the histogram-based statistical analysis of photodiode traces in recent work [26, 51] is the availability of a full noise frequency spectrum for every measured RIN value,

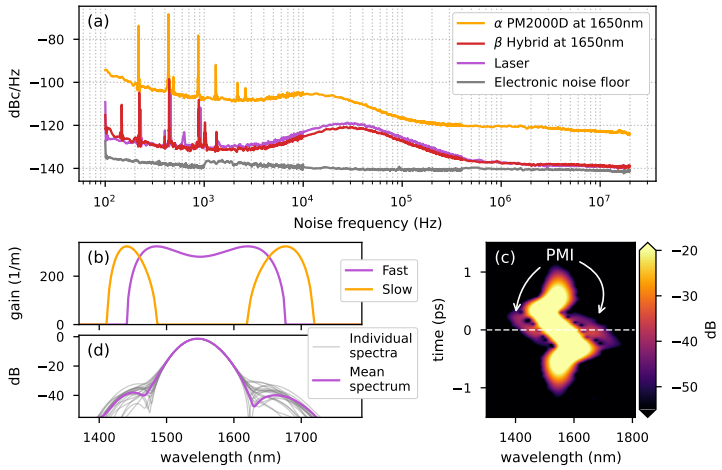

Figure 3.4: (a) Detailed noise-frequency spectra of the RIN measurements at 1650 nm, marked α and β in Fig. 3.3, compared to the pump laser. (b) Analytically calculated PMI gain in PM2000D fiber assuming a 30 kW peak power pulse propagating on slow and fast axis, respectively. (c) Simulated fast axis spectrogram of a 500 fs, 30 kW pulse after 3 cm propagation in PM2000D injected into the slow axis. (d) Spectral slice through the spectrogram in (c) at $t = 0$ for multiple simulations with random noise seeds (gray) and corresponding mean (purple).

which can be used to identify the underlying noise amplification mechanisms. We illustrate this for the RIN measurements recorded at 1650 nm, which are marked α and β in Fig. 3.3 and result in integrated RIN of 0.38 % and 0.05 % for stand-alone ANDi and hybrid fiber SC, respectively. The detailed noise spectra for these two measurements are displayed in Fig. 3.4 (a) and compared directly to the pump laser. The noise spectrum of the stand-alone ANDi SC is shifted upward by about 20 dB with respect to the pump due to the dominance of excess white noise, which is a characteristic signature of quantum noise amplification [16]. This unambiguously confirms the presence of incoherent nonlinear dynamics, which have to be of vectorial nature since they cannot be reproduced by scalar simulations, as discussed above. In contrast, these nonlinearities are suppressed in the hybrid fiber, which even exhibits slightly lower noise than the pump laser in the mid-range frequencies between 1 kHz - 1 MHz.

Fig. 3.4 (b) identifies PMI as the origin of this nonlinear noise amplification in the stand-alone PM2000D ANDi fiber, showing that the analytically calculated PMI gain bands [20] for our experimental conditions overlap exactly with the 1400 - 1700 nm spectral region where the measurements in Fig. 3.3 (a) detect elevated RIN values. In order to illustrate how this PMI gain leads to pulse-to-pulse intensity fluctuations of the generated SC, we conduct vectorial GNLSE simulations taking into account the coherent coupling of the two polarization eigenmodes [89]. Additionally, we increase the input pulse duration to 500 fs, which enhances the visibility of the incoherent PMI dynamics by slowing down the coherent wave-breaking process. The simulated spectrogram in Fig. 3.4 (c) shows clear signatures of PMI after only 3 cm of propagation in the form of

two side bands being generated at spectro-temporal positions outside the main pulse. As these side-bands remain unseeded, random quantum fluctuations serve as the seed and are amplified to become significant. Taking a slice through the spectrogram at $t = 0$ and repeating the simulations several times clearly shows the random amplitude fluctuations introduced by PMI at spectral positions corresponding very well to the analytically calculated PMI gain bands (compare Figs. 3.4 (b) and (d)). While we consider pure slow-axis pumping in this case, in reality we expect a blend of fast- and slow-axis dynamics as we observe also linear coupling of the polarization states in the PM2000D fiber reducing the PER from >30 dB at the input to about 15 dB at the output, even at low power.

In order to understand why PMI occurs in the stand-alone ANDi fiber but is largely suppressed in the hybrid fiber, we consider the characteristic length scales of both coherent and incoherent dynamics. In the case of the stand-alone ANDi fiber, the optical wave-breaking length $L_{\mathrm{WB}} = 1.7\,\mathrm{cm}$ is shorter but comparable to the PMI length $L_{\mathrm{PMI}} = 5.3\,\mathrm{cm}$, indicating a certain balance between the two processes. In the hybrid fiber, two factors suppress PMI. First, the higher birefringence and anomalous dispersion of the PM1550-XP fiber completely suppress PMI during the soliton pre-compression phase for slow axis pumping. Second, upon entering the ANDi fiber, the short duration and high peak power of the pre-compressed pulse reduces L_{WB} to approximately 1 mm, indicating an extremely fast spectro-temporal reshaping of the pulse followed by a fast drop in peak power due to dispersive stretching. This leads to a constant shift of the spectro-temporal positions of the PMI gain bands, such that PMI-amplified noise is not allowed to accumulate and build up from the shot-noise level. Instead, it is spread out over a wide region of the spectrogram and does not become significant. These dynamics are very similar to the suppression of scalar incoherent nonlinearities at short pulse durations discussed in detail in [39].

3.3 Phase Coherence

The dominance of the inherently phase-coherent processes of SPM, soliton compression, and optical wave breaking during nonlinear spectral broadening suggests that the SC generated in the hybrid fiber should also exhibit excellent phase stability. We experimentally quantify the phase fluctuations using a free-space asymmetric Michelson interferometer [90]. The setup shown in Fig. 3.5. The SC pulses exiting the hybrid fiber are collimated using reflective optics and routed into a free-space asymmetric Michelson interferometer. They are split into two arms by a broadband 50:50 beam splitter. One arm of the device is set to provide a delay with respect to the other arm corresponding to the pulse repetition period, such that two subsequent SC pulses interfere at the output of the interferometer. The signal is collected with a single-mode fiber (SMF) and directed to an OSA, where spectral interference fringes are created if the SC pulse train is phase-stable over time intervals exceeding the OSA sweep time. The measurement was performed in sections of approximately 200 nm with optimization of the SMF coupling for each wavelength region. A neutral density filter is used to approximately match the intensity between the two arms in order to obtain good fringe visibility. Two different SMF patch cords (SM1060

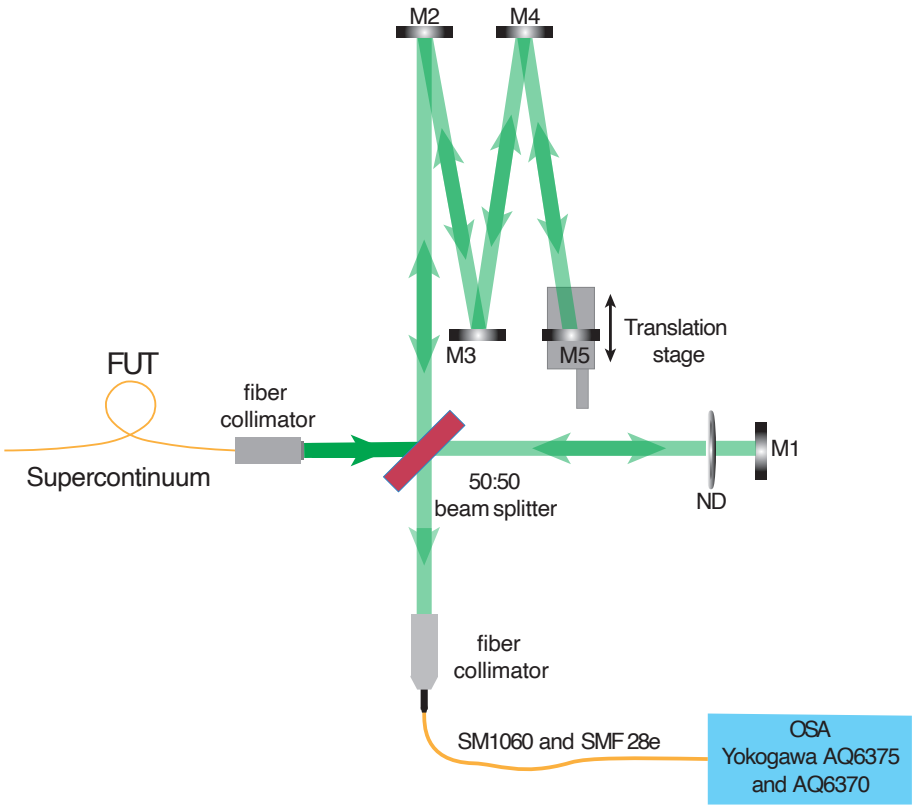

Figure 3.5: Experimental setup for the measurement of the phase coherence of the SC generated in the hybrid fiber with a free-space asymmetric Michelson interferometer. FUT: Fiber under test; M: mirror; ND: Neutral density filter; OSA: Optical spectrum analyzer; SMF: single-mode fiber

and SMF28e) and two OSA (Yokogawa AQ6370 and AQ6375) were employed to cover the full bandwidth of the SC spectrum with adequate signal-to-noise levels while simultaneously ensuring single-mode guidance for good spatial overlap of the interfering signals. The fringe spacing is chosen by fine-tuning the delay time between the interfering pulses using a translation stage located in the long arm. We experimentally verified that the chosen spacing has negligible effect on fringe visibility and extracted coherence as long as the fringes can be well resolved with the OSA.

A single sweep lasts several seconds and thus records the ensemble average of $> 10^8$ interference events, such that the magnitude of the degree of first-order coherence as a function of wavelength becomes measurable as [91]

$$|g_{12}(\lambda)| = \frac{V(\lambda)[I_1(\lambda) + I_2(\lambda)]}{2[I_1(\lambda)I_2(\lambda)]^{1/2}}, \tag{3.2}$$

where $I_1(\lambda)$ and $I_2(\lambda)$ are the measured light intensities in each arm of the interferometer, and $V(\lambda)$ is the fringe visibility given by the maximum and

minimum fringe intensity, $V(\lambda) = [I_{\max}(\lambda) - I_{\min}(\lambda)]/[I_{\max}(\lambda) + I_{\min}(\lambda)]$. Equation (3.2) is equal to the expression routinely used in numerical studies $|g_{12}| = \langle E_1^* E_2 \rangle / [\langle |E_1|^2 \rangle \langle |E_2|^2 \rangle]^{1/2}$ with the spectral field envelopes $E_1(\lambda), E_2(\lambda)$ and ensemble average $\langle . \rangle$, but expressed in experimentally accessible variables. Note that the calculation of $|g_{12}(\lambda)|$ accounts for differences in the interfering intensities, which in practice are difficult to equalize exactly in broadband measurements, and therefore represents a better figure of merit for coherence than the visibility $V(\lambda)$ itself. The fringe spacing, and hence the spectral resolution of the coherence measurement, can be chosen by fine-tuning the temporal delay between the interfering pulses. It is well known that the value of $|g_{12}(\lambda)|$ is primarily sensitive to phase fluctuations and only to a much lesser extend to intensity noise [14, 92], such that it provides a convenient, broadband, self-referenced and high resolution measure of phase-stability complementary to the RIN characterizations performed above.

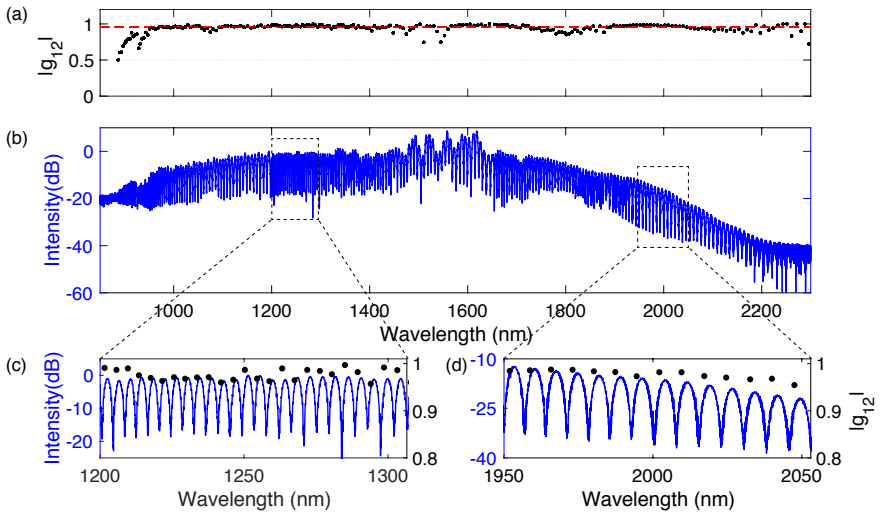

Figure 3.6: Experimental phase coherence measurements of the SC generated in the hybrid fiber using spectral interferometry. (a) Magnitude of first order coherence determined according to Eq. (3.2). The red dashed line indicates the spectrally averaged coherence of $\langle |g_{12}| \rangle = 0.96$. (b) Spectral interference measurement showing high extinction fringes over the entire SC bandwidth. (c), (d) Magnified views of interference fringes and coherence around 1250 nm and 2000 nm.

Fig. 3.6 confirms the excellent phase stability of the generated SC, evident from high contrast interference fringes with visibility in the order of 20 dB measured over the entire bandwidth of the hybrid fiber SC. $|g_{12}(\lambda)|$ is near unity for the majority of the bandwidth, as exemplary highlighted in the magnified views of Fig. 3.6 (c) and (d). The coherence averaged over the full 900 - 2200 nm bandwidth is calculated to $\langle |g_{12}| \rangle = \int |g_{12}(\lambda)| I(\lambda) d\lambda / \int I(\lambda) d\lambda$ =0.96. This ranks among the highest experimentally confirmed magnitude and uniformity of $|g_{12}(\lambda)|$ for fiber- and waveguide-based SC sources to date [48, 93–97]. Slightly degraded coherence is only detected at the spectral edges and around the sharp

spectral features near the pump wavelength, coinciding with the regions of increased RIN in Fig. 3.3 whose origin was already discussed in Section 3.2.2. Near 1800 nm the coherence measurement is disturbed by water vapor absorption lines preventing accurate extraction of visibility and intensities. Using our experimentally determined value of $\langle |g_{12}| \rangle$ and the results of previously published numerical studies [50], we can assign a median shot-to-shot timing jitter $\delta t < 0.5\,\mathrm{fs}$ to the pulse train emitted by the hybrid SC source, revealing stability down to a small fraction of an optical cycle.

3.4 Comparison with Conventional SCG in Hybrid Fibers

So far, only a single hybrid fiber design was investigated. It is yet unknown which highly nonlinear fiber (HNLF) dispersion design is the optimal choice for the hybrid fiber concept for minimizing noise and maximizing spectral bandwidth and flatness of the resulting SC. Separating the initial soliton pulse compression from the subsequent spectral broadening in two discrete fibers, both individually optimized for each task, could also be beneficial for nonlinear fibers with conventional dispersion design pumped near their ZDW, potentially resulting in even broader spectral bandwidth and lower noise.

In this section, we compare the ANDi PM2000D with two other HNLFs with conventional dispersion profiles. HNLF-AD and HNLF-ND exhibit a single ZDW and provide low anomalous and normal dispersion at the pump wavelength, respectively. Therefore, these fibers are ideally suited to experimentally clarify the influence of the fiber dispersion profile on the noise characteristics of the resulting SC under identical pumping conditions.

A summary of geometric, linear and nonlinear optical parameters of all 3 fibers is given in Table 3.1. HNLF-AD (sold by FORC-Photonics as HNLF DS) exhibits anomalous dispersion at the pump wavelength, with a ZDW of $1.47\,\mu\mathrm{m}$ and $D = 3.3\,\mathrm{ps/(nm\,km)}$ at 1550 nm. Its mode field diameter (MFD) is given as $4.2\,\mu\mathrm{m}$ by the manufacturer, and we estimate its nonlinear coefficient to $\gamma = 10.3\ (\mathrm{Wm})^{-1}$. Due to a slightly elliptic core the fiber has a group birefringence of 0.9×10^{-4} relative index units (RIU). On the other hand, HNLF-ND (marketed by OFS as HNLF-PM-M2) provides normal dispersion over the pump spectrum, with a ZDW of 1.62 µm and $D = -1.07\,\mathrm{ps/(nm\,km)}$ at 1550 nm. Birefringence of 2.8×10^{-4} RIU is introduced by an elliptic core, and MFD as well as nonlinear coefficient are similar to HNLF-AD.

Fiber	MFD (µm)	ZDW (nm)	Dispersion (ps/nm/km)	Group birefringence	Nonlinearity ($\mathrm{W^{-1}km^{-1}}$)
PM1550-XP	10.1	1340	18	4.6×10^{-4}	1.4
HNLF-AD	4.2	1469	3.3	0.9×10^{-4}	10.3
HNLF-ND	4	1620	-1.07	2.8×10^{-4}	10.5
PM2000D	3.5	All normal	-46.7	0.2×10^{-4}	13.3

Table 3.1: Geometric, linear, and nonlinear properties of the 3 fibers used. All values except ZDW are given for a wavelength of 1550 nm.

The optimal length of PM1550-XP is determined via cut-back measurements to be 5.7 cm. For a fair comparison, we make a new hybrid PM2000D fiber alongside the two other HNLF fibers with this length of PM1550-XP. Including measurements done with direct pumping, this means that 6 fibers are being compared. The fabrication and measurement techniques are very similar that those used in the sections above. For more detail, see the published article [62].

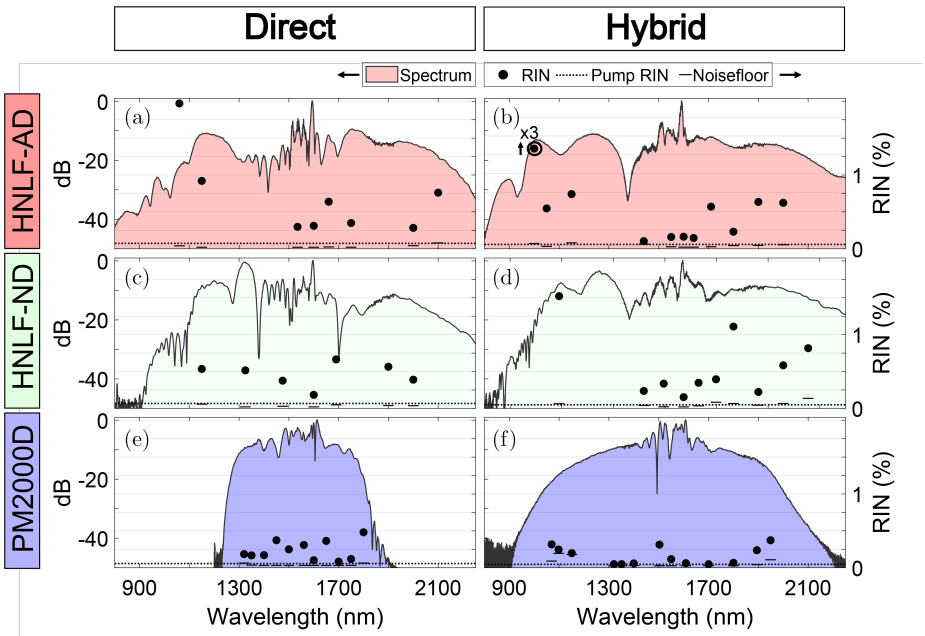

Figure 3.7: Measured SC spectra generated in the six investigated nonlinear fibers and their spectrally resolved RIN under identical pumping conditions. Pump pulses were injected directly into HNLFs (left column) or in their respective hybrid version (right column). Results for HNLF-AD, HNLF-ND, and PM2000D are shown in top, middle, and bottom row, respectively. RIN is measured for spectral slices of 20 nm width (dots) shown with respective noise floor (-) and compared to the pump laser RIN (0.05 %, dashed line).

Figure 3.7 presents the SC spectra generated in the six investigated nonlinear fibers together with measurements of the respective spectrally resolved RIN All measurements were obtained with identical pumping conditions with a coupled pump peak power of 33 kW and 110 fs pulse duration. The pulses were injected into HNLF-AD, HNLF-ND and PM2000D fibers either directly (left column) or in their respective hybrid version (right column). We obtained output SC average powers of 200 mW from the directly pumped HNLFs, which is reduced to about 160 mW from the hybrid fibers due to splice loss. The length of each fiber is adjusted individually in such a way that the full spectral bandwidth can develop, but short enough to avoid unnecessary spectral modulation and build-up of noise.

In general, we observe increased RIN levels near sharp spectral features, such as strong modulations or dips. This is due to the fact that the position of these features depends on the total nonlinear phase shift linked to the pump peak

power, such that small pump fluctuations are translated to a relatively large change in SC signal. Hence, sharp spectral features generally act as amplifier of input intensity noise, and constitute an important link between flatness and noise level of SC sources.

For HNLF-AD, Fig. 3.7(a) and (b), the hybrid fiber generates SC spectra with significantly less fine structure, overall improved spectral flatness, and increased −30 dB spectral bandwidth (176 THz vs. 150 THz). The spectra feature a broad and smooth soliton structure around 2 μm and a massive dispersive wave extending from 1.35 µm down to below 1 µm wavelength, whose position can be tuned by controlling input pulse chirp [98]. In contrast, in the SC spectra emitted by the directly pumped fiber these features are narrower and exhibit stronger spectral modulation. However, the spectrally resolved RIN measurements result in similar values for both fibers, ranging mostly between 0.25 - 1 %. Near the pump wavelength we observe a noise reduction in the hybrid fiber SC to 0.1 - 0.2 %, while the short wavelength dispersive wave peak generally exhibits higher noise, reaching 2 % for the directly pumped fiber and increasing to 4 % in the hybrid fiber, which corresponds to nearly 80 times amplification of the pump laser noise.

Although HNLF-ND exhibits normal dispersion at the pump wavelength, nonlinear self-phase modulation dynamics quickly transfer significant energy to the anomalous dispersion region, where dynamics are very similar to HNLF-AD discussed above, both for the directly pumped and the hybrid fiber. This is evident from the measured spectra shown in Fig. 3.7(c) and (d), which generally resemble the spectra generated in HNLF-AD, but are slightly narrower on the short wavelength edge and, in the case of the directly pumped fiber, even more strongly modulated. The effect of the hybrid approach is also very similar to the previous discussion: we observe a general reduction in spectral fine structure, improved spectral flatness, and an increase in −30 dB spectral bandwidth from 142 THz to 173 THz It is interesting to note that pumping on the normal dispersion side of the ZDW does not have a notable benefit for the stability of the SC, except for the absence of the singular very high noise peaks. In fact, for the conditions investigated in this work there is hardly any significant advantage of HNLF-ND over HNLF-AD, with the latter producing broader SC bandwidth, similar spectral shapes, and similar noise levels.

As discussed in the sections above, PM2000D, shown on Fig. 3.7(e) and (f), clearly benefits the most of all tested fibers from the hybrid approach. While the benefits for HNLF-AD and HNLF-ND are apparently limited to an improved spectral flatness and increased bandwidth without significant change in noise properties, the hybrid PM2000D sees not only a doubling of spectral bandwidth in comparison to direct pumping, but also a significant reduction of RIN down to the limit given by the pump laser.

Soliton compression takes place in the hybrid fibers with a nearly ideal soliton number of $N \simeq 4$, which leads to a much better quality of the compressed pulse as compared to the case of directly injecting the pump pulses into HNLF-AD, where they form a soliton of order $N \simeq 17$. The high quality compression in the hybrid fiber produces a cleaner pulse shape concentrating more energy in the central pulse peak and, therefore, producing higher peak power even after splice losses are taken into account (120 kW vs 70 kW). This directly explains the increased SC bandwidth generated with the hybrid fiber approach. The cleaner pulse shape is also the reason for the reduced spectral modulation observed

in the hybrid fiber SC, because any form of temporal imperfections directly translate to strong spectral interference structures in the generated SC [86].

It is interesting to directly compare the noise levels achieved in the three different hybrid fibers. In all of these cases, the pulse at the point of maximum compression is identical, namely the compressed ~ 20 fs soliton delivered at the end of the SMF section. Under these conditions only the fiber design determines the noise properties of the generated SC. As is evident from our measurements, the SC generated in the hybrid ANDi HNLF exhibits on average significantly lower noise than can be obtained in the other hybrid HNLF with conventional dispersion design pumped near their ZDW. This experimentally confirms the theoretical considerations presented in Section 2.2 suggesting that the gain for noise-amplifying nonlinear effects in ANDi fibers is suppressed by up to one order magnitude with respect to fibers in which a significant part of the SC spectrum overlaps with the anomalous dispersion regime.

3.5 Conclusions

We demonstrate that the stability of nonlinear spectral broadening dynamics in normal dispersion fibers is ultimately limited by the occurrence of modulational polarization instabilities, even in commercial-grade, PANDA-style polarization-maintaining step-index designs pumped by 100 fs pulses. This limitation can be overcome in a hybrid fiber approach that combines soliton compression with optical wave-breaking dynamics, uniting the most coherent aspects of nonlinear dynamics in anomalous and normal dispersion regions, respectively. This approach converts a standard ultrafast Er:fiber laser in an octave-spanning SC source covering the 930 - 2130 nm with up to one order of magnitude lower RIN over a broader spectral bandwidth than could be previously obtained with any fiber-based SC source, and requiring less than 1/5th of the injected peak power that would be necessary to obtain equal spectral bandwidth in the stand-alone ANDi fiber. The fibers required to reproduce our experiments are commercially available from an online catalog at a combined cost of $50.

In contrast, for HNLFs with conventional dispersion design pumped near their ZDW, either in normal or anomalous dispersion regime, the benefit of the hybrid approach is limited to an improved spectral flatness and increased bandwidth, while they exhibit on average about an order of magnitude higher noise with much stronger wavelength dependence than can be obtained with the hybrid ANDi HNLF.

We note that the hybrid scheme can be scaled for lasers with pulse repetition rates of hundreds of megahertz or gigahertz with limited peak power per pulse. The soliton compression factor and pulse quality solely depend on the soliton number N, and keeping $N \simeq 5$ typically yields a good compromise between the two factors [40]. Hence, by choosing a pre-compression fiber with suitable nonlinearity and dispersion, e.g. from the range of highly nonlinear fibers available from several manufacturers, a wide range of laser pulse peak powers and durations can be accommodated [98]. Similarly, choosing an ANDi fiber with dispersion closer to zero enhances the wave-breaking-dominated spectral broadening [53, 99]. Hence, the low-noise nonlinear spectral broadening dynamics presented here are readily transferable to various laser platforms.

We anticipate this work to be particularly relevant for high-precision applications where intensity noise critically matters, including hyperspectral and multimodal imaging, dual-comb spectroscopy, seeding of optical amplifiers, arbitrary optical waveform generation, and photonic signal processing such as analog-to-digital converters, where peak-to-peak power fluctuations of $<0.1\%$ are required for achieving 10-bit resolution [100]. High amplitude stability also minimizes indirect system performance degradation by noise coupling processes, such as amplitude-to-phase noise conversion in photodiodes or intensity-to-f_{ceo} noise conversion in optical frequency combs [101, 102]. Since the nonlinear dynamics are dominated by self-phase modulation and optical wave-breaking, we also expect excellent phase-noise performance with relative synchronization between different spectral components on time scales much shorter than an optical cycle [103].

Chapter 4

Shot-Noise-Limited Dual-Comb Supercontinuum Generation

Parts of this chapter are included in an article submitted for publication [104]. Experimental work was led by Sandro Camenzind and Christopher R. Phillips in the group of Ursula Keller at ETH Zurich, while I led the work on numerical simulations

Dual OFC laser systems combine two OFCs [105–107] with slightly different repetition rates, enabling dual-comb interferometry (DCI) measurements that uniquely combine the advantages of fast measurements in the electronic domain with high temporal and spectral resolution in the optical domain [9, 108–110]. The DCI technique is attractive for a wide variety of applications including absorption spectroscopy in the mid-infrared [109], laser ranging [111], microscopy [112], sensing of traces gases across open-air paths [113], and digital holography [114]. Dual-comb lasers are also well-suited to nonlinear measurement techniques including pump-probe sampling [115, 116], and Raman imaging [117].

To address the many situations when dual-comb applications require or benefit from a broad optical bandwidth, dual-comb lasers can be used to drive coherent SCG in an optical fiber [63] or waveguide [94, 118], resulting in a dual-comb SC source with ultra-broad bandwidth. However, as mentioned in the Chapter 1, many applications are also very sensitive to the noise introduced by the nonlinear broadening process. While ANDi fibers are preferred for low-noise SCG, as shown in Section 2.2, they require a substantially higher pump peak power to achieve comparable bandwidth to that of conventional SCG. A solution to this problem is offered in Chapter 3. This solution involves fabricating a hybrid fiber where high peak powers are reached in an anomalous fiber, but SCG is dominated by coherent OWB to minimize noise-amplifying dynamics. Yet, the 1053 nm laser source used in this work makes conceiving such a fiber challenging because of the smaller assortment of commercially available fibers designed for this wavelength. Therefore, a single PM ANDi fiber is used

here to achieve dual-comb SCG and demonstrate shot-noise limited dual-comb interferometry from a gigahertz repetition rate SC pumped by a single-cavity dual-comb laser.

To reach this milestone, a high-power 1-GHz dual-comb oscillator is combined with a PM ANDi PCF. The oscillator is similar to the configuration presented in [119]: it uses a Yb:CALGO gain medium and achieves dual-comb operation with low timing jitter by using spatial multiplexing to generate both combs in the same free-running laser cavity [120]. Since the oscillator delivers up to 2.6 W average power per comb to the fiber input, it can drive the SC process directly without an amplification step that would degrade its noise properties, and without requiring a hybrid fiber approach. 1.6 W average power of each oscillator comb is coupled into one of the orthogonal polarization axes of a single PM ANDi fiber (with $> 60\,\%$ coupling efficiency) to obtain a dual-comb SC spanning 820 -1280 nm (-20 dB). Its noise properties are investigated by studying several individual spectral bands of the SC, each having a width of ≈ 15 nm (-10 dB), and confirm shot-noise limited DCI across the entire SC bandwidth. Each band also reaches a RIN power spectral density below -160.9 dBc/Hz, which is around 10 dB lower compared to previous results with ANDi fibers [61, 76, 77]. In the central region of the SC spectrum the noise from the pump laser is suppressed by more than 20 dB, *i.e.*, most of the SC spectrum has less noise than the pump laser.

Additionally, the DCI measurements are performed at a repetition rate difference of $\Delta f_{\mathrm{rep}} \approx 3.95$ kHz, which supports the resolution of the whole SC in parallel without spectral aliasing. By phase-tracking one comb line with a 1064-nm CW laser and correcting the relative timing jitter between the two combs, all spectral bands can be coherently averaged, including field components with a large time or frequency offset from the main interferograms. When filtering the SC to a bandwidth of ≈ 4 THz, the peak spectral SNR reaches 38.7 dB $\sqrt{\mathrm{Hz}}$. The corresponding dual-comb spectroscopy figure of merit (FOM) [121] is $> 1.1 \times 10^7 \sqrt{\mathrm{Hz}}$ in all spectral bands [104].

To the best of our knowledge, this work marks several important milestones: (i) the first shot-noise limited DCI from a SC source, (ii) the broadest SC from an ANDi fiber driven by a GHz laser, (iii) the lowest RIN from any SC source, (iv) the largest suppression of input noise by a SC process, and (v) the highest spectrally-resolved dual-comb FOM from a SC source. This is also achieved with a simple setup comprised of a single laser cavity and a single PCF.

4.1 Relative Intensity Noise

The two pulse trains are combined in a cross-polarized state using a thin-film polarizer so that with an aspheric lens they can be coupled simultaneously into the orthogonal principal birefringence axes of single PM ANDi fiber (NL-PM-1050-NEG, NKT Photonics) with collapsed air-holes on the input side for increased coupling efficiency. This ANDi fiber has a length of 26 cm, a specified mode field diameter of 2.6 ± 0.5 µm and a dispersion parameter of $D = -8 \pm 6$ ps/nm/km at 1050 nm (group velocity dispersion 4.7 ± 3.5 fs^2/mm). It has borosilicate stress rods and a slightly elliptical core to introduce a birefringence $> 1.7 \times 10^{-4}$ nm. A half-wave plate (HWP) is used to align the polarization

state of the input pulses along the fiber's principal birefringence axes to suppress depolarization-induced noise.

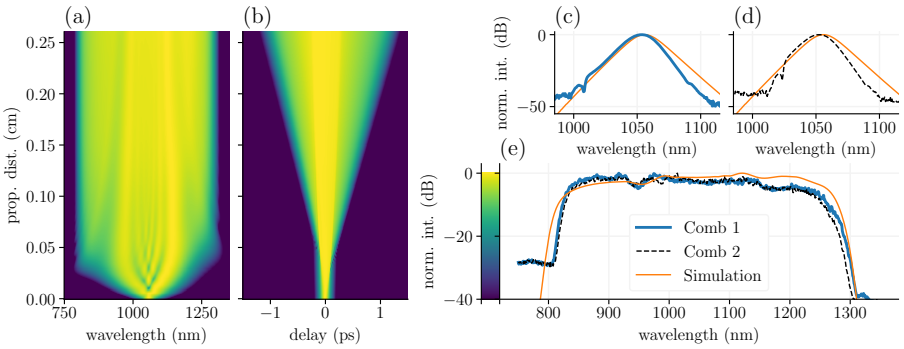

Figure 4.1: Supercontinuum generation in the ANDi fiber. (a) Simulated spectral evolution. (b) Simulated temporal evolution. (c) Measured SC spectra of both combs and simulated spectrum.

The high peak power of the oscillator is sufficient to broaden the optical spectra to several hundred nanometers of bandwidth (126 THz). To understand this SC process we perform numerical pulse propagation simulations using a scalar, GNLSE model (see Chapter 2.1.5). For the simulations, we assume transform-limited sech^2 pulses whose width is matched to the measured spectra. Spectra of the pumps are shown on Fig. 4.1(c) and (d). A simulation of the SC dynamics at maximum input power is shown in Fig. 4.1(a) (spectral domain) and 4.1(b) (time domain). The resulting broadband and flat-top optical spectrum the dual-comb SC are shown in Fig. 4.1(e). The simulated SC spectra show good agreement with the experimental measurements. The spectra are also remarkably flat, even around the oscillator wavelength of 1053 nm. This flatness results from the combination of OWB dynamics in the ANDi SC process [99] and pumping the fiber directly with the output of a bulk solid-state oscillator operating in the soliton modelocking regime [122], which provides near-ideal transform-limited pulses.

4.1.1 Impact of RIN on Sensitivity

The noise sources relevant for the sensitivity of DCI measurements are noise equivalent power (NEP), shot noise, source RIN, and dynamic range of the digitizer as discussed in [123]. The shot noise term dominates that of NEP provided sufficient optical power is detected, for example a few hundred microwatts for near-infrared detection. Care must be taken to avoid nonlinearities [124], but by suitable choice of detector and avoiding excessive gain this can be managed up to powers well over a milliwatt [121]. Digitizer dynamic range, if it is a limiting factor, can be avoided by chirping one of the interferograms to introduce a differential optical chirp between the two combs [125]. These considerations suggest that unless the measurement is shot-noise limited, RIN directly affects the integration time required to reach a given SNR and hence the sensitivity of the measurement [123]. Furthermore, the nonlinear broadening process couples

RIN and pulse timing noise [50], so a high RIN also leads to increased timing jitter thereby degrading the coherence of the pulse train.

While low-frequency technical RIN components can generally be suppressed, the broadband RIN due to additive amplified spontaneous emission (ASE) and noise-amplifying incoherent dynamics is more problematic. Even the use of balanced detection only halves this broadband RIN term rather than canceling it down to the shot noise limit as would apply for non-interferometric measurements. It is thus a key parameter for assessing the suitability of a laser system for sensitive measurements.

To analyze the noise of SC sources, it is critical to measure the RIN in a spectrally-resolved fashion since its intensity noise is typically anti-correlated across the spectrum [49, 87], meaning that without spectral filtering we cannot quantify this effect and might thus underestimate the true RIN. For example, the standard $\chi^{(3)}$ modulation instability adds noise but conserves energy in the pulse, so that the total pulse energy may have similar RIN to the input. However, the spectrally-resolved RIN of SC sources can exhibit noise that is many orders of magnitude above that of the input pulses [15, 16].

4.1.2 Measurement and Simulation of RIN

For assessing the RIN, we couple only one pulse train (comb 1) into the ANDi fiber to prevent distortions of the measurement by periodic interferograms or intensity modulations. After passing through the monochromator, the spectrally filtered light is detected on an InGaAs photodiode (modified DET10N2, Thorlabs). To enable high sensitivity for a wide range of noise frequencies, the resulting photocurrent is analyzed in a baseband measurement by an ESA (E5052B, Keysight Technologies) with two different measurement schemes, one for low noise frequencies and one for high noise frequencies, which are stitched together as described in [120].

We record the SC RIN in several $\approx 15\,\mathrm{nm}$ wide spectral bands from 850 nm up to 1250 nm in 50 nm increments. We adjusted the power on the photodetector with an iris from around 11 mW at 850 nm down to 7 mW at 1250 nm according to the wavelength-dependent photodetector responsivity to ensure that the shot noise (SN)-limit is similar for all spectral bands and to prevent saturation effects. The selected filter bandwidth allows for sufficient optical power at the detector to achieve shot-noise levels below -160 dBc/Hz for all spectral bands, while still preserving the structure of the spectrally resolved RIN according to our numerical simulations. The oscillator RIN is recorded as well in order to determine its relation to the RIN of the spectrally filtered SC The one-sided RIN PSDs are shown in Fig. 4.2(b). The oscillator has a noise plateau of around -130 dBc/Hz until about 30 kHz when it begins decreasing until reaching SN limited performance for sideband frequencies beyond 1 MHz. For the SC the spectrally-resolved RIN measurements reach the SN limit for all spectral bands, including the spectral wings of the supercontinuum and remain shot-noise limited up to the Nyquist frequency. This confirms the ultra-low noise performance and indicates that there is no degradation of the coherence from the SC process.

In particular, the RIN of each band reaches a noise floor below -160.9 dBc/Hz, which marks a ≈10 dB improvement compared to previous low-noise results with ANDi fibers [61, 76, 77]. This also manifests itself in the record-low integrated RIN achieved with this source. At the lowest-noise spectral band

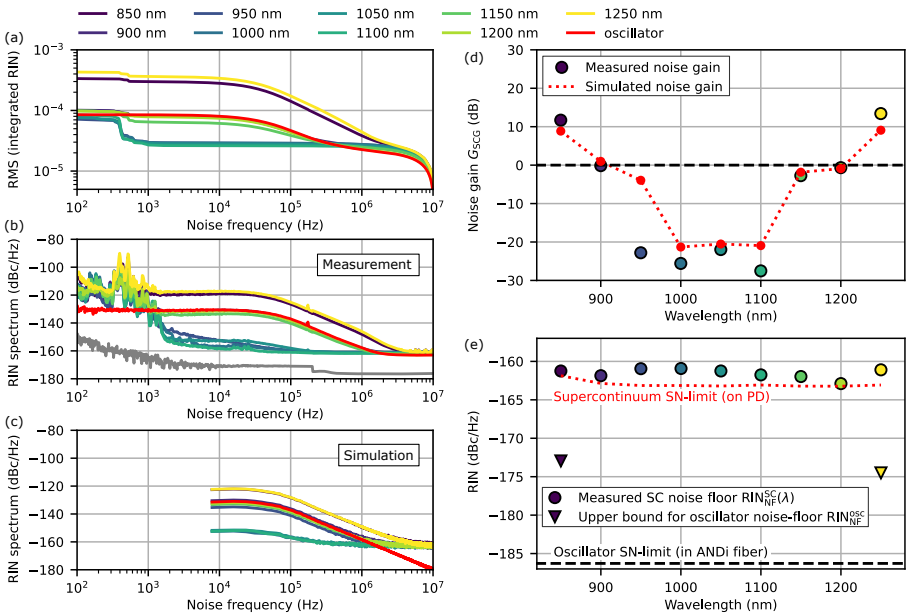

Figure 4.2: (a) Spectrally-resolved integrated RIN for around 15-nm-wide spectral bands at different wavelengths and (b) corresponding one-sided RIN PSD. The measurement noise floor (gray) was determined by blocking the incident light on the photodetector and scaling the resulting PSD with the typical DC photocurrent of around 6.2 mA in the unblocked case. (c) Simulation of the RIN PSD according to the laser parameters and oscillator RIN. To mimic the expected noise properties of the solid-state oscillator, its high-frequency RIN is extrapolated down to the shot-noise limit corresponding to the fiber-coupled average power of 1.6 W, which is approximately 25 dB lower than the photodetector shot-noise limit, as shown in (e). (d) Noise gain transfer function inferred for the measured and simulated RIN PSD (e) Noise floor of the measured spectrally-resolved SC RIN (dots) together with the theoretical shot-noise limit for the corresponding power on the photodetector. This measured SC noise floor together with the noise gain transfer function gives an upper bound for the oscillator noise floor (triangles). The theoretical shot-noise limit of the oscillator for the fiber-coupled average power of 1.6 W is indicated by the dashed black line.

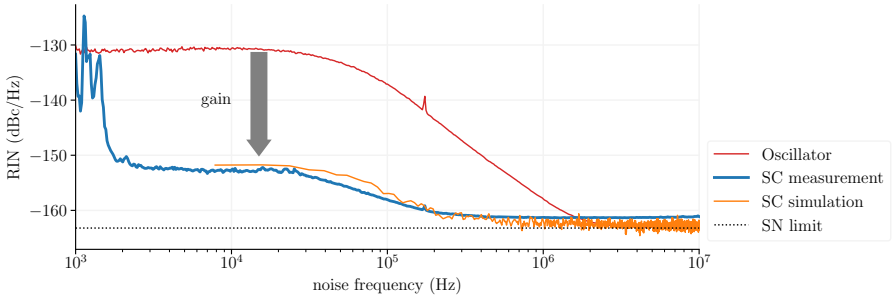

Figure 4.3: Detailed RIN PSDs for a slice centered at 1050 nm. Both simulated and measured PSDs are shown, together with the measured oscillator RIN to help visualize the noise gain.

(1100 nm ± 8 nm), for example, we obtain an integrated RIN of 2.7×10^{-5} for the integration range [1 kHz, 10 MHz] (Fig. 4.2(b)), which is an unprecedented level for a SC source.

When integrating the noise down to 100 Hz the RIN increases slightly due to additional low-frequency features on the noise spectrum. Inspection of Fig. 4.2(b) shows that these features are not on the oscillator spectrum, so their presence on the SC spectra can be explained by environmental fluctuations that lead to small amplitude noise when coupling into the small-core ANDi fiber.

Another interesting aspect of the RIN measurements can be seen from the noise plateau. Remarkably, Fig. 4.2(b) shows that for the spectral bands near the oscillator wavelength, the spectrally-resolved SC RIN is suppressed by more than 20 dB compared to the oscillator RIN. Further away from the oscillator wavelength, the noise suppression decreases and becomes positive towards the wings of the supercontinuum spectrum due to the influence of laser peak power fluctuations on the SC bandwidth. To quantify this noise suppression we introduce a noise gain parameter G_{SCG} which the oscillator pulses experience during the spectral broadening in the ANDi fiber as illustrated in Fig. 4.2(d). This noise gain transfer function is computed as the average gain factor between the measured oscillator and supercontinuum RIN PSDs of the various spectral bands for noise frequencies between 10 kHz and 20 kHz.

To better understand the observed noise gain transfer function, we use the scalar GNLSE model to simulate the RIN PSD of the supercontinuum. The overall strategy is to mimic the physical system by constructing a time series of simulation input pulse energies having statistics that match the experimentally measured RIN PSD (see Chapter 5). Since the oscillator is a soliton mode-locked laser the pulse duration τ_0 decreases with increasing pulse energy E, and this needs to be accounted for in the simulations. We observe experimentally that, for small changes around the nominal laser operating point, the pulse duration scales as $\tau_0 \propto E^{-1/2}$ (slightly different from the standard E^{-1} behavior for soliton modelocking). Therefore, for each input pulse energy E_j in the time series, we assume a corresponding pulse duration $\tau_{0,j} = \tau_{0,\mathrm{ref}} \times (E_j/E_{\mathrm{ref}})^{-1/2}$ (where subscript 'ref' refers to the nominal laser operating point). This yields a time series of input parameter pairs $[(E_1, \tau_{0,1}), (E_2, \tau_{0,2}), ..., (E_N, \tau_{0,N})]$ for $N \gtrsim 5 \times 10^6$. We simulate the pulse propagation for each parameter pair,

calculate the output optical spectrum, and then select the same spectral bands as we used in the experiments. For each spectral band in the SC, we thereby obtain a time series of pulse energies from which a RIN PSD can be calculated.

The simulated RIN PSDs (Fig 4.2(c)) agree well with the measured spectra (Fig 4.2(b)). A detailed plot of the 1050 nm slice is shown on Fig. 4.3 as well, where it is easy to visualize how the measured noise gain is defined. For a more detailed version of Fig. 4.3 from a simulation perspective, see Fig. 5.4 in Section 5.5. To determine the noise gain G_{SCG} for the simulated RIN PSDs we use the same procedure as for the RIN measured in the experiment, *i.e.* comparing the RIN of the (spectrally filtered) SC to that of the oscillator; for this comparison we use the values of the simulated RIN at 15.7 kHz. The resulting simulation of the noise gain transfer function in Fig. 4.2(d) is consistent with the experimentally observed noise suppression around the central wavelength. This noise suppression can be explained by (i) a redistribution of the oscillator RIN to the spectral wings of the supercontinuum resulting in a coupling of the pump pulse intensity fluctuations to the SC bandwidth and (ii) the anti-correlation between the pulse duration and peak power of the oscillator pump pulses [126].

Our simulation predicts that the SC RIN reaches the SN limit for all spectral bands, in agreement with our measurement results. This is also illustrated in Fig. 4.2(e), which shows the noise floor of the measured relative intensity noise $\mathrm{RIN}_{\mathrm{NF}}^{\mathrm{SC}}(\lambda)$ together with the theoretical SN limit for the corresponding power on the photodetector.

In the spectral wings of the supercontinuum, the noise gain transfer function is positive, implying that the SC has higher noise than the oscillator. Despite this, we still observe SN-limited performance in these spectral bands (850 nm and 1250 nm). This indicates that the low RIN of the solid-state oscillator at high noise frequencies enables the SN-limited SC We can even predict an upper bound for the oscillator noise floor $\mathrm{RIN}_{\mathrm{NF}}^{\mathrm{osc}}$ that is needed for SN-limited SC measurements at a spectral band around the wavelength λ:

$$\mathrm{RIN}_{\mathrm{NF}}^{\mathrm{osc}} \leq \mathrm{RIN}_{\mathrm{NF}}^{\mathrm{SC}}(\lambda) - G_{\mathrm{SCG}}(\lambda). \tag{4.1}$$

The predicted upper bound for $\mathrm{RIN}_{\mathrm{NF}}^{\mathrm{osc}}$ is indicated with a triangle in Fig. 4.2(e) for spectral bands where it is below the measured oscillator RIN noise floor at -163 dBc/Hz. This is the case for $\lambda = 850$ nm with $\mathrm{RIN}_{\mathrm{NF}}^{\mathrm{osc}} \leq$ -173 dBc/Hz and for $\lambda = 1250$ nm with $\mathrm{RIN}_{\mathrm{NF}}^{\mathrm{osc}} \leq$ -175 dBc/Hz. A lower-bound for the fiber-coupled oscillator RIN is given by its SN-limit of -186 dBc/Hz (for 1.6 W average power), which suggests that the SC RIN could potentially still be SN-limited even for a significantly higher noise gain. This analysis highlights the value of using powerful laser oscillators (with $\gg 100$ mW directly from the oscillator) to drive highly nonlinear processes while maintaining SN-limited performance. It also demonstrates the potential of using nonlinear processes to infer bounds on laser noise that would otherwise be inaccessible: while saturation of the photodiode limits our RIN measurements to about -165 dBc/Hz, we can infer lower RIN values by measuring the output of a noise-amplifying nonlinear process with known noise gain transfer function. This is a step towards experimentally accessing the true noise floor of the oscillator [18].

4.2 Shot-Noise-Limited Dual-Comb Interferometry

Both combs are combined, spectrally filtered, and detected on a fast free-space InGaAs photodiode (DET08CL, Thorlabs) resulting in interferograms (IGMs). An important aspect for high-sensitivity DCI measurements is sufficiently low relative timing and phase noise between the combs to allow for coherent averaging without loss of information and over long timescales. For free-running dual-comb lasers, this can generally be achieved by increasing the repetition rate difference Δf_{rep} between the combs until the timing and phase fluctuations are sampled fast enough to correct them unambiguously [119, 127]. There is however one limitation: to avoid spectral aliasing for a given optical bandwidth $\Delta\nu_{\mathrm{opt}}$, Δf_{rep} cannot be increased beyond the point where the RF bandwidth occupied by the interferograms is larger than $f_{\mathrm{rep}}/2$, i.e.

$$\Delta f_{\mathrm{RF}} = \Delta\nu_{\mathrm{opt}} \times \frac{\Delta f_{\mathrm{rep}}}{f_{\mathrm{rep}}} < \frac{f_{\mathrm{rep}}}{2}. \tag{4.2}$$

For the individual spectral bands, this condition requires $\Delta f_{\mathrm{rep}} \lesssim 90$ kHz, but using such a large value would require adjusting Δf_{rep} for each individual spectral band to position the IGM spectrum around $f_{\mathrm{rep}}/4$. On the other hand, avoiding aliasing over the full supercontinuum bandwidth of more than 120 THz requires $\Delta f_{\mathrm{rep}} \lesssim 4.2$ kHz. We therefore set $\Delta f_{\mathrm{rep}} \approx 3.95$ kHz so that the system is compatible with simultaneous measurement of the whole spectrum on one or multiple detectors. As a result, we can tune the monochromator across the entire supercontinuum spectrum resulting in electronic dual-comb signals between DC and $f_{\mathrm{rep}}/2$.

To complement the RIN measurement of the single-comb presented in Fig. 4.2(b), we compare the noise floor of the dual-comb IGM measurements to their shot noise limit. To do so, we investigate the RMS voltage noise of the dual-comb IGMs in the time domain. For this purpose, we record DCI signals for each spectral band with a zoom-in on the vertical axis of the oscilloscope to reduce the impact of the oscilloscope noise on the measured voltage noise. We then coherently average the DCI signals for $T = 9.6$ ms (*i.e.* 38 IGM periods) with an alternating sign for subsequent segments so that the coherent signals cancel and only the noise remains. More details on the coherent averaging process can be found in the publication [104]. The RMS voltage noise is then computed for a 50 µs time window and displayed in Fig. 4.4 relative to the theoretical shot noise limit.

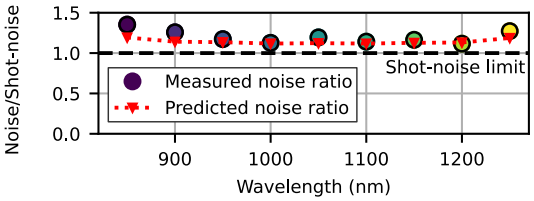

Figure 4.4: RMS voltage noise relative to shot noise of the DCI measurements.

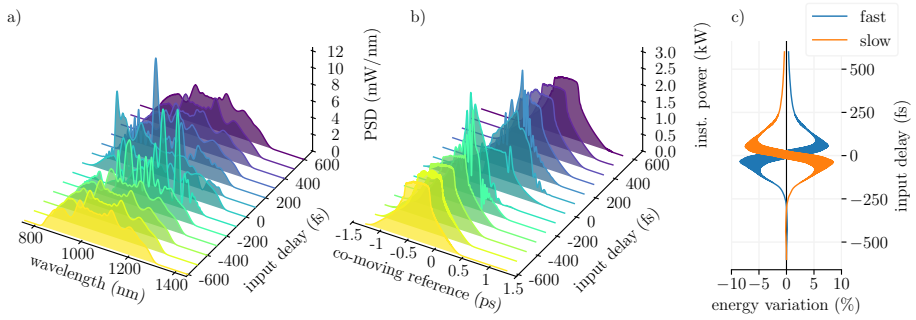

Figure 4.5: Spectral (a) and temporal (b) envelope of comb 1 after propagation of both combs in the ANDi fiber as function of input delay. (c) Energy variation in % of initial energy after propagation for both fast axis (comb 1) and slow axis (comb 2).

To develop such a system for which shot noise is the dominant noise term, it is crucial to understand and minimize the contribution of the other relevant noise sources [128, 129]. Thus, we modeled the influence of shot noise, quantization noise, Johnson noise, and specified excess noise from the amplifier, photodiode, and oscilloscope used on the ratio between RMS voltage noise and theoretical shot noise. This calculation is in close agreement with the measured noise/shot-noise ratio (see Fig. 4.4), which confirms that our supercontinuum source is indeed shot noise limited.

4.3 Mitigating the Impact of Cross-Phase Modulation

In our setup, we use a single, highly birefringent nonlinear fiber to broaden a dual frequency comb source, whereby the combs have orthogonal linear polarization states, and one comb is injected into each of the polarization axes of the fiber. Since the two combs have slightly different repetition rates differing by Δf_{rep}, the temporal offset between the pulses propagating on each axis changes from shot-to-shot. Due to the short pulse duration and fiber length, most pulses do not temporally overlap in the fiber and no nonlinear coupling between the two combs occurs, leading to the generation of identical SC spectra on both fiber axes.

However, when temporal overlap occurs in the fiber, nonlinear interaction between the combs leads to temporal and spectral envelopes that are highly dependent on the temporal offset, i.e. drastic changes occur from shot to shot and the spectra generated on slow and fast axis are no longer identical. Using a vectorial, dual-polarization GNLSE simulation [130], we investigated this interaction and found it to be dominated by cross-phase modulation (XPM). Since XPM is a highly coherent process, it leads to deterministic and periodic intensity and phase modulations of the pulse trains with frequency Δf_{rep}. Hence, while periodicity is lost on the level of each individual comb for the period of

temporal overlap, it is maintained on the level of Δf_{rep} in the sense that two pulses separated by $\Delta T = 1/\Delta f_{\text{rep}}$ are identical.

The drastic effect of XPM can bee seen on Fig. 4.5, where we plot spectral and temporal envelopes of comb 1 at the output of the fiber for a few input delays. The spectral and temporal modulations are only severe when both pulses enter the fiber within $\sim 250\,\text{fs}$ of each other. Fig. 4.5(c) shows the energy lost or gained during the interaction of both pulses as function of input delay. Because total energy is conserved, the plot is symmetric about the y-axis.

To prevent these periodic modulations from compromising the DCI measurements, a temporal delay line is added to one of the combs after the nonlinear fiber. The resulting DCI signal is shown on Fig. 4.6(a). This ensures that only undistorted pulses contribute to the formation of the important central part of the dual-comb interferogram (Fig. 4.6(c)), while the artifacts introduced by XPM interaction, such as that shown on Fig. 4.6(b), are pushed into the wings where they can be removed in post-processing. Fig. 4.7 shows another perspective, where it is clear that modulated optical spectra can be separated temporally, thus guarantying that only identical SC spectra overlap temporally.

4.4 Conclusions

In this chapter, we report the first shot-noise-limited dual-comb supercontinuum with >1 W average power. Each spectral band measured in the 820 nm to 1280 nm SC is SN-limited. Moreover, we observe up to 20 dB of RIN suppression near the pump wavelength, with a record low 1 kHz–10 MHz integrated RIN of 2.7×10^{-5} at 1100 nm. These measurements are validated both by measuring the noise floor of the IGM signal and by numerical simulations. The latter is made possible by a new simulation method that can generate a realistic, noisy pulse train based on the measured RIN PSD of the oscillator. By numerically accessing the true noise floor of the generated SC, we open up new possibilities for measuring ultra-low noise levels that are otherwise challenging to quantify experimentally.

Such low noise is achieved by using a high power, dual-comb oscillator with 2.6 W per comb, a single cavity and single fiber approach to maximize the mutual coherence of both combs, and an appropriate ANDi PCF. This eliminates the need for (i) any amplification stage, thus reducing the impact of additive ASE, or (ii) fabrication of a suitable hybrid fiber such as that presented in Chapter 3, which has not yet been tested with polarization-multiplexed, co-propagating pulses, and would be a technical challenge at this pump wavelength.

Thanks to the $> 60\,\%$ coupling efficiency, $> 1\,\text{W}$ per comb is available at the fiber output, resulting in a theoretical shot noise limit of $-186\,\text{dBc/Hz}$, making it the ideal platform to drive highly nonlinear processes without incurring noise penalties. The artifacts caused by the nonlinear interaction of both combs while co-propagating in the fiber can be easily mitigated by adding a delay line after the fiber for one of the comb, which has been both experimentally and numerically verified.

In summary, our GHz system enables high-sensitivity and broadband DCI measurements and is thus highly attractive for dual-comb sensing applications such as broadband spectroscopy, hyperspectral LiDAR and imaging, and multicolor pump-probe measurements. In addition, the low-noise SC is ideal for

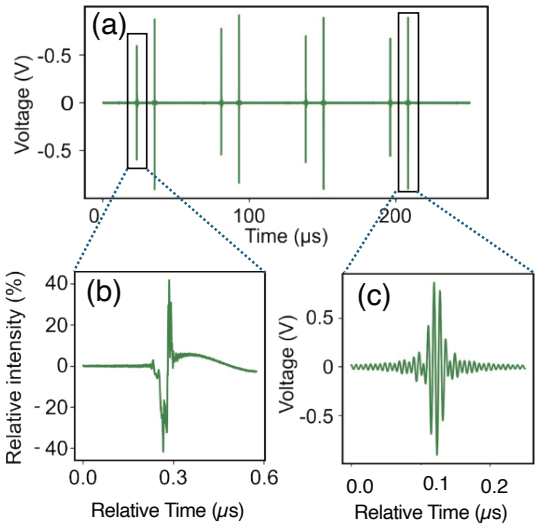

Figure 4.6: (a) IGM trace at 1103 nm. (b) Zoom in on artifact caused by cross-phase modulation (XPM) modulations. (c) Undisturbed interferogram.

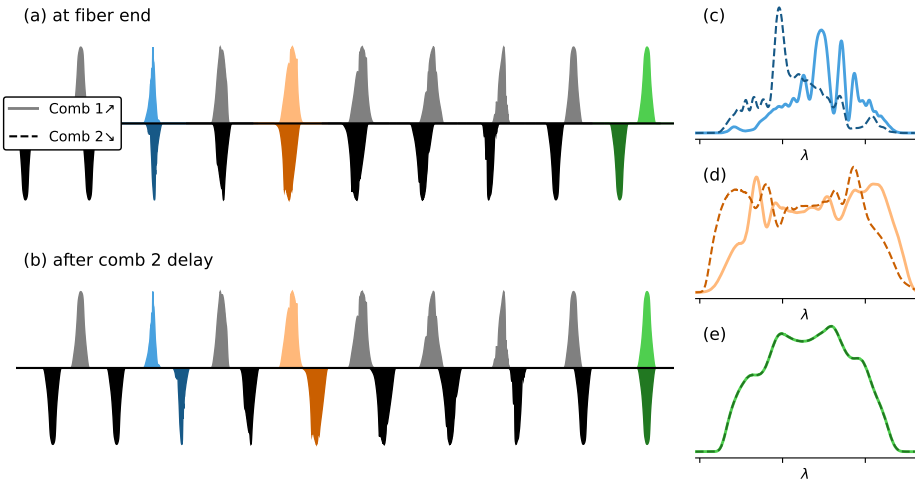

Figure 4.7: Schematic illustration of the effect of nonlinear interaction between two combs propagating in a single nonlinear optical fiber. (a) Pulse trains from both combs at the output of the fiber. Highlighted spectra in (c) and (d) show modulated, temporally overlapped pulses. (b) Same pulse trains as in (a) but comb 2 is delayed. Only undistorted pulses with identical spectra, shown in (e), overlap in time.

generating a strong carrier-envelope offset beat signal for frequency comb stabilization, and the bandwidth achieved in this work would already be sufficient for $2f - 3f$ interferometry.

Chapter 5

Accurate Simulations of Noise Evolution in Optical Fibers

This chapter will be submitted as a standalone article for publication.

Numerical modeling is essential for understanding the complex nonlinear dynamics involved in laser system design. Several models of ultrashort nonlinear pulse propagation have been developed to analyze a wide range of scenarios [20, 34]. These models can handle even complex phenomena such as nonlinear coupling of multiple spatial modes, the interaction of gain and nonlinearity, or plasma effects due to photoionization in gas-filled hollow-core fibers. In contrast, and despite its importance, there has been surprisingly little focus on accurately modeling the evolution of noise during nonlinear pulse propagation. This assessment, together with the remarkable experimental results of Chapter 4, prompted us to develop a more complete numerical model of noise propagation in nonlinear fibers.

Ultrashort pulse trains emitted by lasers and amplifier systems, which drive nonlinear processes, exhibit various types of noise, such as fluctuations in pulse energy, duration, center frequency, and timing jitter, which can be coupled to each other in various ways. This noise can be accurately quantified using PSDs, which are commonly used in experimental noise measurements. For example, the RIN PSD, $\hat{S}_I(f)$, represents the spectrum of the pulse energy fluctuations relative to their average value. Here, f denotes the noise frequency rather than the optical frequency. Fluctuations in the pulse train occur at frequencies between zero and half the repetition rate, i.e. typically in the RF range. In real laser systems, the noise power distribution is highly frequency dependent, resulting in complex and highly nonlinear noise PSDs. Yet, many numerical studies in literature use oversimplified noise models. These studies typically only consider shot noise, thus completely ignoring systemic laser noise sources, or they assume a Gaussian noise distribution, resulting in a frequency-independent white-noise PSD. Such simplifications fail to capture critical nonlinear dynamic phenomena, such as amplitude-phase noise coupling, and also fail to differentiate between low- and high-frequency noise components - the former can often be

managed with electronic feedback loops, while the latter accumulate and can lead, for instance, to the described coherence loss in frequency comb systems. Consequently, an accurate modeling framework for nonlinear noise propagation is still lacking.

This chapter introduces a set of tools for the realistic numerical simulation of noise in ultrafast nonlinear optics. An outline of the four steps involved is illustrated in Fig. 5.1. These are 1. Acquisition of an input noise PSD 2. Generation of a pulse train whose noise statistics match said PSD 3. Propagation of each pulse individually 4. frequency-domain analysis of the resulting pulse train. Presented as general guiding principles rather than a strict recipe, our approach allows for maximum flexibility. Many noise types can be simulated, even multiple at once. As discussed below, some decisions involved in the pulse train generation process must be physically motivated, thereby tailoring the model to each specific situation. Moreover, this model is not constrained to the GNLSE; any propagation equation, such as the unidirectional pulse propagation equation (UPPE) can be used.

In the following sections, the distinction between the single-shot and the multi-shot domains is first established. This will allow for the exploration of different types of noise and the frequency scales at which they exist, thus providing some motivation for a framework capable of simulating realistic, multi-shot noise evolution. Next comes an overview of the Welch method, a technique used to estimate PSDs from a temporal signal. Inspired by this technique, it is possible to develop a procedure to generate a pulse train with realistic noise properties from an experimental noise PSD measurement and to track the PSD evolution in numerical pulse propagation simulations, which is the core of the approach presented here. Once the model is established, it will be compared with 2 other current approaches seen in the literature. Finally, to demonstrate the applicability of this model, it will be applied to analyze the strong noise suppression dynamics during the nonlinear spectral broadening of GHz optical frequency combs in all-normal dispersion photonic crystal fibers, showing excellent agreement with experimental data.

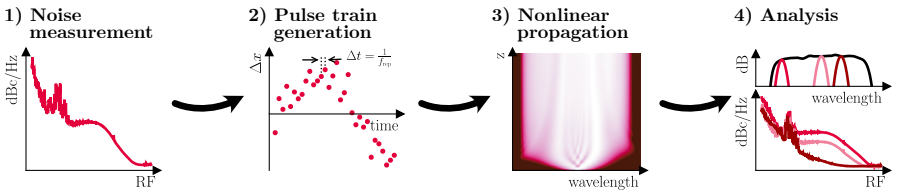

Figure 5.1: Summary of the simulation pipeline proposed in this work.

5.1 Noise in Numerical Simulations

In a typical nonlinear pulse propagation simulation, the aim is to model the spectral and temporal transformation of an ultrashort pulse in a nonlinear medium. The initial pulse, delivered by an ultrafast laser system, has measurable parameters such as pulse duration and energy, which are used as input for the simulation. The pulse is then numerically propagated through the nonlinear

medium by solving one of the many available propagation equations, e.g. the GNLSE or the UPPE. These simulations are typically single-shot, meaning they track the evolution of a single ultrashort pulse.

To account for noise in a simulation, noise terms can be added to the propagation equation in order to model certain dynamics. For example, the literature contains various versions of the GNLSE that include noise arising from linear and nonlinear loss, gain or spontaneous Raman scattering [14, 18, 20].

Noise can also be added as part of the initial conditions. This can be done either in form of global parameter fluctuations, such as changes in pulse energy, or the addition of a noisy spectrum to the initial one, as is done when adding shot noise. As simple as this approach is, it nevertheless allows modeling of complex noise dynamics such as modulational instabilities or incoherent cloud formation, even if the propagation equation contains no noise terms. Only noise at the initial conditions is considered in the rest of this chapter.

Noise is a statistical quantity and cannot be measured on a single pulse. Therefore, a simulation is repeated N times using different noise seeds. The result is evaluated statistically and compared with the input pulse ensemble. This provides the data necessary to evaluate the influence of the nonlinear dynamics on the noise properties of the pulse train. Although this general approach is straightforward, defining an input pulse ensemble that realistically reflects the noise properties of real laser systems is a non-trivial challenge that must be addressed. Doing so will enable a reliable comparison between simulations and experimental data. Here, this problem is solved by generating the input pulse train from experimental noise PSD measurements.

Using this approach requires us to distinguish between two different time / frequency scales: (i) the single-shot or optical domain, where the temporal and spectral properties of a single pulse are defined, typically measured on scales of femto- or picoseconds and tens to hundreds of THz, respectively; and (ii) the multi-shot or RF domain, defined by the repetition time and frequency of the pulse train, i.e. typically on time scales of micro- to nanoseconds and frequencies in the kHz – GHz range. Both domains and their relationships are schematically illustrated in Fig. 5.2.

Optical domain. Taking the formalism of the GNLSE as an example, a single pulse in the time domain is represented as the complex envelope $A(\tau)$. The letter τ is used to distinguish the *optical delay axis* from longer scale pulse-to-pulse dynamics. With the help a frequency shifted Fourier transform $\mathcal{F}_{\mathrm{opt}}$, the complex envelope can be turned into a spectral envelope $\tilde{A}(\omega)$ where $|\tilde{A}(\omega)|^2$ is the optical PSD of the pulse:

$$\begin{aligned} \tilde{A}(\omega) &= \mathcal{F}_{\mathrm{opt}}\{A(\tau)\} = \int_{-\infty}^{\infty} A(\tau) \exp\left(-i(\omega-\omega_0)\tau\right) \mathrm{d}\tau, \\ A(\tau) &= \mathcal{F}_{\mathrm{opt}}^{-1}\{\tilde{A}(\omega)\} = \frac{1}{2\pi} \int_{-\infty}^{\infty} \tilde{A}(\omega) \exp\left(i(\omega-\omega_0)\tau\right) \mathrm{d}\omega, \end{aligned} \tag{5.1}$$

where ω_0 is the central angular frequency of the pulse.

Typical examples of noise sources occurring in the optical domain are shot noise and ASE noise, which manifest as a broadband noise floor and noisy ripples in both time and frequency domains, as schematically illustrated for a single Gaussian pulse in Fig. 5.2(a) and (c), respectively.

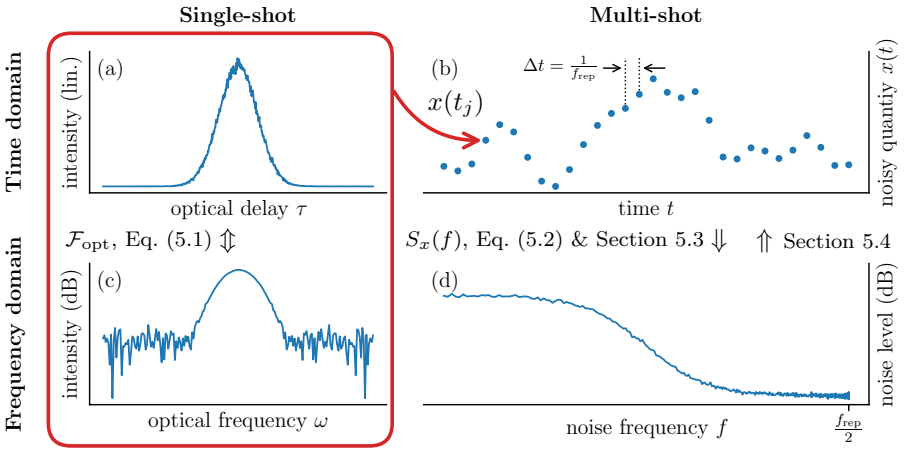

Figure 5.2: Clarification of the different domains used in our discussion. (a) single pulse in the time domain. (b) multiple pulses in the time domain represented each as a single number $x(t_j)$. (c) single pulse in frequency domain. (d) multiple pulses in the RF domain, represented as the PSD estimation of $x_{(t_0)}, \ldots, x_{(t_{N-1})}$.

RF domain. An ensemble of N single-shot simulations and the *multi-shot* time axis t are required to model pulse-to-pulse fluctuations of a particular parameter in a pulse train. In the multi-shot picture, each single-shot simulation $j = 0, \ldots, N-1$ is represented as a single data point $x_j = x(t_j) = x\left(A_j(\tau)\right)$, where x is the noisy pulse parameter of interest, e.g. the pulse energy, duration, arrival time, etc. This is illustrated by the orange arrow in Fig. 5.2(b) relating the single-shot domain to a single data point in the multi-shot time series $x(t)$. t is intrinsically discrete and its grid spacing corresponds to $\Delta t = \frac{1}{f_{\mathrm{rep}}}$, where f_{rep} is the repetition rate of the pulse train.

The time series $x(t)$ can be further analyzed in its corresponding frequency domain f to find the contribution of different noise frequencies to the overall noise power (Fig. 5.2(d)). Although going from the time domain to the frequency domain should simply involve a Fourier transform, as is the case in the optical domain, $x(t)$ is a virtually infinite, aperiodic signal. Because there isn't a value of t above/below which $x(t)$ is always 0, the integral in the Fourier transform doesn't converge. Therefore, a slight modification is required in order to define the one-sided noise PSD $S_x(f)$:

$$S_x(f) = \lim_{T\to\infty} \frac{2}{T} \left| \int_{-T/2}^{T/2} x(t) e^{-i2\pi f t} \mathrm{d}t \right|^2, \quad f \geq 0 \tag{5.2}$$

where f is the noise frequency axis. Because x is real, S_x is symmetric around $f = 0$. Therefore, the factor 2 accounts for the PSD at negative frequencies, which is ignored by definition in a one-sided PSD. This is a commonly made arbitrary choice that is kept throughout this work, but it may differ from the formalism used elsewhere in the literature. The maximum noise frequency is given by the Nyquist frequency $f_{\mathrm{rep}}/2$, while the lowest resolvable noise frequency is limited by the size of the multi-shot ensemble to f_{rep}/N.

It is often useful to consider relative noise quantities normalized to their long-term mean. This is common practice for RIN, and similar normalized noise quantities can also be used for other pulse parameters of interest, such as the pulse duration or the optical center frequency. Only for the phase noise, which is related to timing jitter, such a normalization is not practical because it does not typically oscillate around a steady mean.

In the literature, noisy parameters are often expressed through their standard deviation σ_x. It is very common for RIN, where the RMS RIN σ_E is the standard deviation of $E(t)$, a relative measure of pulse energy fluctuations.

$$\sigma_x = \sqrt{\int_{f_0}^{f_1} S_x(f)\mathrm{d}f}. \tag{5.3}$$

Note that this implies that specifying RIN as a number in percent should always be accompanied by an integration range. When this is not done, it is often implied that f_0 is low enough that it doesn't significantly affect σ_E, and that $f_1 = \frac{f_{\mathrm{rep}}}{2}$. Since $E(t)$ is a signal sampled at a frequency of f_{rep} (one sample per pulse), the Nyquist-Shannon sampling theorem states that this signal contains no information beyond $\frac{f_{\mathrm{rep}}}{2}$. Therefore, f_1 must never be greater than half the repetition rate, contrary to what is suggested in [131].

5.2 Decomposition of Noise Measurements

As highlighted above, noise has to be accounted both in the optical and RF domains. This section presents how these two domains combine into a single noise PSD. Understanding how noise from one domain manifests in the other is crucial to generate a realistic input pulse train whose noise statistics match that of an experimentally measured PSD.

Typically, the following noise contributions can be distinguished:

- Noise in the optical domain, such as SN or ASE, appears as frequency-independent white noise PSD in the RF domain.
- Pulse-to-pulse fluctuations, such as intensity or timing jitter, appear in the RF domain and their PSD can vary strongly with noise frequency. Such fluctuations can be, for example, the result of quantum noise effects associated with laser gain and cavity losses, or technical excess noise, such as vibrational, electronic, or pump diode noise.

The relationship between noise in the optical and RF domain is illustrated in Fig. 5.3 using the relative intensity noise of an ultrafast Erbium-doped fiber master-oscillator power-amplifier (MOPA) system as example. The system emits 40 fs pulses with 300 mW average power at $f_{\mathrm{rep}} = 40$ MHz. The real temporal and spectral pulse shape have no significance for the following discussion, so that an optical spectrum with Gaussian shape is assigned for simplicity.

The RIN PSD of the system was measured with a photodiode detecting the power of the pulse train connected to a RF spectrum analyzer, and is displayed as the red curve in Fig. 5.3(a) in logarithmic units of dBc/Hz in the frequency range from 5 kHz up to the Nyquist frequency of 20 MHz. It exhibits a relatively broad relaxation oscillation peak around 30 kHz, and then drops steadily until

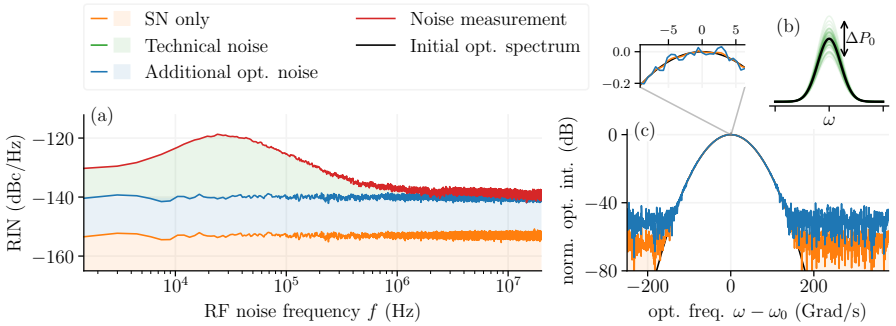

Figure 5.3: Illustration of the correspondence between noise in the RF domain and noise in the optical domain. Fig. (a) shows frequency-resolved RIN in the RF domain. The red line shows the measured RIN PSD of a typical 40 MHz fiber laser. It is the result of adding SN (orange line and shading), additional optical noise (blue line and shading) and technical noise (green shading). Technical noise consists of pulse-to-pulse fluctuations, illustrated in (b) as peak intensity variations. Fig. (c) shows correspondence with the optical domain. The black line is a normalized optical intensity spectrum of a single, noiseless Gaussian pulse. The orange line shows the same pulse with SN added to it. Finally, the blue line shows the effect of amplifying SN to approximate ASE. The inset shows those same curves around the peak of the spectrum.

it reaches a plateau at high noise frequencies above 3 MHz. The integrated RMS RIN value over the measured RF range (Eq. (5.3)) is 0.06%.

The measured noise PSD can be considered as the sum of several noise contributions. The following discussion decomposes it into its individual components by examining the possible noise sources and their manifestation in both optical and RF domains.

Shot noise. To start, it is realistic to include shot noise in the optical domain, as it is a fundamental property of light. The following formula can model SN by adding a random complex number $\tilde{A}(\omega_\ell)$ into each optical frequency bin ω_ℓ:

$$\delta A_{\mathrm{sn}}(\omega_\ell) = \frac{1}{\sqrt{2}}(a + ib), \quad a, b \sim \mathcal{N}\left(0, \sqrt{\frac{\hbar\omega_\ell}{2\Delta\omega}}\right). \tag{5.4}$$

Note that this model, taken from [18], yields a shot noise spectrum with a variance of $\frac{\hbar\omega}{2\Delta\omega}$ where $\Delta\omega$ is the optical frequency bin spacing of the simulation. Therefore, this model differs by a factor 2 from the "one photon per mode" model used elsewhere in the literature [84]. The resulting optical spectrum is plotted in orange on Fig. 5.3(d), where a spectrum of noiseless Gaussian pulses is plotted in black for comparison. Shot noise adds a broadband noise floor, located at approx. -75 dB below the peak in this case, which is important for the accurate simulation of noise-seeded nonlinear effects, such as Raman scattering or modulational instabilities. The RF RIN PSD of a pulse train with SN only is estimated empirically and plotted on Fig. 5.3(a) as a yellow line and shading. It's level average value of $-173\,\mathrm{dBc/Hz}$ matches the theoretical value

[18]:

$$S_{\mathrm{sn}}(f, \omega_0, \langle P \rangle) = \frac{2\hbar\omega_0}{\langle P \rangle}, \tag{5.5}$$

where $\hbar$ is the reduced Planck constant and $\langle P \rangle$ is the average power of 300 mW. Note how the theoretical S_{sn} does not depend on f and is thus a constant line in the RF domain.

Noise at high frequencies. The RIN PSD of most solid-state mode-locked laser oscillators is expected to approach the SN-limit at high noise frequencies, typically above a few MHz. This behavior has its origin in the interplay between the long upper state lifetime of the gain medium and the long cavity damping time, which leads to relaxation oscillations at typical frequencies of tens to hundreds of kHz. In this measurement, the relaxation oscillation peak is located around 30 kHz. Above this cutoff frequency, intensity noise is damped, corresponding to a PSD proportional to f^{-1}, like any driven harmonic oscillator, until the shot-noise limit is reached.

The measured RIN PSD shown on Fig. 5.3(a) forms indeed a plateau above approx. 1 MHz, but at −139 dBc/Hz, it lies more than 30 dB above the shot-noise limit. Following the above arguments, it would be unphysical to model such high-frequency fluctuations simply as pulse-to-pulse peak power variations in the multi-shot picture. Instead, excess noise at high frequencies is often associated with additional noise sources in the optical domain degrading the optical signal-to-noise ratio (OSNR).

In this case, the amplifier of the MOPA system adds ASE noise, modeled in a first approximation simply by multiplying the shot noise δA_{sn} by a factor η, so that its PSD matches the high-frequency noise plateau of the measurement, as indicated by the blue trace in Fig. 5.3(a). η can be determined from the value of the measured RIN PSD $\hat{S}_I$ at the Nyquist frequency $f_{\mathrm{rep}}/2$,

$$\eta = \sqrt{\frac{\hat{S}_I\left(\frac{f_{\mathrm{rep}}}{2}\right)}{S_{\mathrm{sn}}}}. \tag{5.6}$$

For this example, $\eta = 4.34$. In the optical domain, adding this excess ASE noise corresponds to a noise floor raised by 12.8 dB above the SN limit, thus decreasing the OSNR. It also leads to a significant noisier optical spectrum, even at the peak, as shown by the blue trace in Fig. 5.3(d). This higher noise floor has important consequences, because it lowers the threshold for the onset of noise-seeded incoherent nonlinear effects and, therefore, generally increases the noise and degrades the coherence properties of the light exiting the nonlinear medium.

If required, the treatment of ASE can easily be extended to include a frequency dependence in the optical domain, e.g. based on a measured optical spectrum with sufficient dynamic range.

Noise at low frequencies. Because the combined effect in the RF domain of SN and ASE yields a flat PSD that matches the plateau of the measured one above 1 MHz, the remaining noise power, shaded in green in Fig. 5.3(a), is distributed only at low frequencies below 1 MHz. It can be accounted for by adding pulse-to-pulse variations to the multi-shot simulations. In our RIN example, this is done by altering the peak power of each pulse (and thus its energy) with a random variable whose PSD matches the shape of the region

shaded in green. The details of the procedure and this particular examples are given in Section 5.4.

5.3 Power Spectral Density Estimation

This section provides a brief summary of numerical PSD estimations, more precisely the Welch method [132], because they are crucial for understanding our model and its limitations. A Welch method implementation is already provided in most numerical libraries, but a better understanding of PSD estimations in general can be gained by reading chapter 13 in [133].

Given a vector $x = (x_0, \ldots, x_{N-1})$ of N equidistant samples of a noise signal $\hat{x}$ taken at interval $\Delta\tau = 1/f_{\mathrm{rep}}$, we want to numerically implement Eq. (5.2) and compute an estimation S of the true PSD $\hat{S}_x$ of the signal. $\hat{x}$ can represent any noisy, measurable value that satisfies the wide-sense stationary (WSS) process definition. Examples of WSS processes in the context of laser noise include RIN, pulse duration noise, etc. However, extra care must be taken when making PSD estimations of a signal that is not a WSS process. Phase noise is a notable example because it is tied to timing jitter, which is not a quantity that oscillates around a steady mean. The problem is especially severe close to the zero frequency, as the typical $1/f$-like PSD of timing jitter suggests a singularity around $f = 0$. Ref. [18] goes into more details about how to mitigate this when it comes PSD estimations.

A crude way to estimate the PSD of the sequence x is simply to take the absolute value squared of its discrete Fourier transform (DFT). This is called a periodogram, and there are two main problems with this simple approach:

1. The periodogram has a variance of 100%. In other words, the value of the periodogram in each frequency bin has a variance equal to itself.

2. Because $\hat{x}$ is not periodic, taking the DFT of a finite portion is akin to masking it with a rectangular window, which creates leakage from one frequency bin to their neighboring ones due to the frequency response of a rectangular window.

The second issue is the easier one to deal with. We simply need to choose a better window than a rectangular one. For our use case, the Hann window is suitable. A detailed analysis of the properties of many different window families is available in [133].

With a fixed number N of points (corresponding to N single-shot simulations as explained in Section 5.2), it is possible to trade frequency resolution for reduction in variance. A straightforward approach is to take some average, either across several frequency bins, or across several periodograms. Those two approaches are mathematically very similar, and for cases where it is not difficult to repeat the single-shot simulations many times it is then easy to compute the periodograms to the desired frequency resolution and average them.

However, we can get even more variance reduction for a given number of points. From a sequence of $N = (K + 1)M$ points, we create K overlapping segments of $2M$ points compute their periodogram and average them together. Each segment consists of the points $(x_{jM}, \ldots, x_{(j+2)M-1})$, $j = 0, ..., K-1$. The variance of the final, averaged periodogram is reduced by about $9K/11$ compared

to not segmenting the data at all [132]. However, the smallest measurable nonzero frequency increases from f_{rep}/N to $f_{\mathrm{rep}}/2M$.

5.4 Generating a Pulse Train from a Noise Measurement

In a procedure that is loosely equivalent to inverting Eq. (5.2), it is possible to generate a pulse train from a measured noise PSD. Because PSDs discard any phase information, this problem is a version of the famous 1D phase retrieval problem, which has no unique general solution. Indeed, there are infinitely many time domain signals that share the same PSD. However, as the ultimate goal is to be able to analyze PSDs of simulated pulses, any one of these signal will work for our purposes.

To decide the size N of the simulated pulse train, we must bear in mind that the final PSD estimations will resolve only $M+1$ frequency points, spread uniformly between $f = 0$ and $f = f_{\mathrm{rep}}/2$. Therefore, two different grids are used: a fine grid with a frequency spacing of f_{rep}/N, which will be used to generate the initial pulse train, and a coarse grid with spacing of $f_{\mathrm{rep}}/2M$, which is the grid of the PSD estimation. Both grids are identical if $K = 1$, but we strongly advise using a higher value of K to get smoother PSD estimations. M must be determined such that all nonzero frequency points of the coarse grid are covered by the measurement. K can then be freely determined to get the final number $N = (K+1)M$ of simulations. Note that this procedure is written assuming N is even, but it can be adapted for an odd N. We can now interpolate the measured PSD at $\frac{N}{2}+1$ uniformly spaced points from zero to the Nyquist frequency $f_{\mathrm{rep}}/2$. This yields $\mathbf{S} = (S_0, \ldots, S_{N/2})$. Points interpolated at $0 \leq f < f_{\mathrm{rep}}/2M$ not cover by the measurement can be set to 0 without loss of generality.

As explained in Section 5.2, certain noise sources need to be added in the optical domain rather than in the RF domain. Typically, only the remaining low-frequency fluctuations are added as pulse-to-pulse variations in the multi-shot picture.

Hence, we must first find the total contribution S_{opt} of all optical domain noise sources in the RF domain and subtract it from the measured noise PSD. In our example, this applies to SN and ASE noise, such that $S_{\mathrm{opt}} = \eta^2 S_{\mathrm{sn}}$ (Eqs. (5.5) and (5.6)).

Before inverting $\mathbf{S}$ into the time domain, we need to add a phase spectrum to it. This is the stage where we choose one of the infinitely many possible signals whose PSDs match the measurement. The simplest way to pick a phase is to consider no correlation between each frequency bin and simply sample a random phase ϕ_k on a uniform distribution $\mathcal{U}[0, 2\pi)$. Note the exceptions $\phi_0 = \phi_{\frac{N}{2}} = 0$ because the DFT of a real signal is always real at the zero and Nyquist frequencies.

Lastly, because most inverse fast Fourier transform routines require a two-sided spectral amplitude, we must add a factor $1/2$. This yields the final spectral amplitude vector ρ, whose components are

$$\rho_k = \sqrt{\frac{\max(S_k - S_{\mathrm{opt}}, 0)}{2}} e^{i\phi_k}, \tag{5.7}$$

where we ensure that the argument of the square root is non-negative, as noisy input data could lead to negative values.

We can now generate the signal $x = (x_0, \ldots, x_{N-1})$ by computing the inverse DFT of the vector ρ.

$$x_j = \sqrt{N f_{\text{rep}}}\ \mathrm{F}^{-1}[\rho]_j. \tag{5.8}$$

The normalization factor guarantees that the average power $P_{\text{avg}} = \frac{E_{\text{tot}}}{T}$ over any period $T = N/f_{\text{rep}}$ is preserved.

Since x is real and ρ is already scaled as if it were a two-sided amplitude, we can take advantage of functions dedicated to real signals, such as `irfft` in Numpy [36], to compute F^{-1}. For numerical tool kits that do not implement this shortcut version, we can create a complete two-sided version of ρ,

$$\hat{\rho}_k = \begin{cases} \rho_k\,, & k = 0, \ldots, \frac{N}{2} \\ \rho^*_{N-k}\,, & k = \frac{N}{2}+1, \ldots, N-1, \end{cases} \tag{5.9}$$

where * denotes the complex conjugate. The inverse DFT is then computed as

$$\mathrm{F}^{-1}[\rho]_j = \frac{1}{N} \sum_{k=0}^{N-1} \hat{\rho}_k \exp\left(\frac{i2\pi jk}{N}\right). \tag{5.10}$$

This method is very versatile and yields a sequence x whose periodogram is the original PSD. This means that it inherits its units in the following way: $[S_k] = \mathrm{u}^2/\mathrm{Hz} \implies [x_j] = \mathrm{u}$. In particular, a PSD in dBc/Hz yields a unitless signal. Although it can be delicate to compute PSD estimations of timing jitter due to the issue raised in the previous section, the inverse process of finding a pulse train from a PSD measurement is typically not problematic. This is because the limited feasible number of simulations imposes a limit on the lowest simulated frequency. Moreover, in our framework, the value of the PSD at $f = 0$ can always be set to 0 without loss of generality.

As an example, let us generate a pulse train starting with the RIN measurement of Fig. 5.2(a). First, the measured RIN level at the Nyquist frequency of 40 MHz is -140.29 dBc/Hz. This is S_{opt} that we subtract from the original measurement in Eq. (5.7). The SN sits at xxdBc/Hz for our 1550 nm, 300 mW laser system, which yields $\eta = xx$ that we use to add the appropriate amount of noise in the optical domain. We choose to write the energy of each pulse $E_j = \langle E \rangle (1 + x_j)$ where $\langle E \rangle$ is the mean pulse energy. To translate this variation of energy into the shape of each pulse, we assume a simple model where only the peak power varies while the pulse width τ_0 remains constant. Therefore, assuming a Gaussian pulse, each initial pulse envelope $A_j(\tau)$ is given by

$$A_j(\tau) = \sqrt{\frac{\langle E \rangle (1 + x_j)}{\sqrt{\pi/2}\ \tau_0}} \exp\left(-\left(\frac{\tau}{\tau_0}\right)^2\right) + \eta \delta A_{\text{sn},j} \tag{5.11}$$

with the pulse duration's FWHM equal to $\tau_0\sqrt{2\ln 2}$. $\delta A_{\text{sn},j}$ is generated according to Eq. (5.4) with a different noise seed for each pulse.

5.4.1 Dealing with Measurement Limitations

A common issue in noise measurements is that experimental setups often restrict the detection of noise to levels significantly higher than those of the laser system

itself. For instance, when detecting the power of a pulse train with a photodiode for intensity or phase noise measurements, the power level must be kept sufficiently low to avoid photodiode saturation. If the laser system's power exceeds this threshold, attenuation is required, which inherently introduces additional quantum noise. Consequently, the SN limit of the measurement becomes higher than the actual SN limit of the light being measured.

If the measured noise PSD is limited by the noise floor of the measurement system, which may occur especially at high noise frequencies, there is no universal model to correct for this. However, in certain cases, additional physical considerations can help mitigate the issue. For example, the noise in many parameters of mode-locked laser oscillators is expected to reach its fundamental quantum limit at high noise frequencies [134]. This physical insight provides a rationale to extrapolate the measured PSD down to the SN limit, such as in the case of RIN to the level predicted by Eq. (5.5). Section 5.5 provides an example of this approach. If no corrective model is available, the measurement can still be used as a worst-case scenario assessment.

5.4.2 Attenuation Adds Noise

In experiments, attenuation may also be used to analyze the noise properties of the light exiting the nonlinear system. The quantum noise introduced by this attenuation must be considered in the numerical simulation as well to ensure accurate comparison with the experiment [18]. This consideration also applies to situations when the output of the nonlinear system is spectrally filtered. For example, the RIN of supercontinuum light generated in nonlinear fibers is often analyzed by dividing it into multiple narrow spectral bands to reveal wavelength-dependent fluctuations. Consider, for instance, a Gaussian bandpass filter $b_C(\lambda)$ centered at λ_C and of FWHM $\Delta\lambda$,

$$b_C(\lambda) = \sqrt{T} \exp\left[- \left(2 \ln\left(1+\sqrt{2}\right) \frac{\lambda - \lambda_C}{\Delta\lambda} \right)^2 \right], \tag{5.12}$$

where the wavelength $\lambda = 2\pi c/\omega$ and the parameter T is the peak transmission of the filter. The introduction of the filter is accounted for by generating a new shot noise spectrum $\delta\tilde{A}_{\mathrm{sn}}(\omega)$ according to Eq. (5.4) and combining it with the output of the filter to produce the filtered spectrum $\tilde{A}_{k,C}$,

$$\tilde{A}_{k,C}(\omega) = b_C(\lambda)\tilde{A}_k(\omega) + \sqrt{1 - b_C(\lambda)^2}\ \delta A_{\mathrm{sn}}(\omega), x \tag{5.13}$$

where c is the speed of light.

5.4.3 High Repetition Rate Lasers

A quick back of the envelope calculation yields that for GHz lasers, PSD estimations down to the kHz range with sufficiently low variance necessitate millions of individual simulations. While this is certainly not impossible to accomplish, there are a couple of tricks one might use to reduce the amount of simulations needed to achieve a certain minimum frequency.

The technique used to simulate big frequency ranges consists of propagating pulses that are too similar. After all initial pulses are created, they can be sorted

into a histogram. Exactly what metric is used to create the histogram depends on what kind of noise is simulated. For example, if only RIN is considered, we make a histogram where pulses are binned according to their total energy. For each bin, we choose one single pulse to represent the bin and be propagated. We then perform the PSD estimation on the full sequence $x_{g(k)}, k = 0, \ldots, N-1$ where g maps any pulse onto the representative of its bin. The suitable number of bins can be determined empirically by considering more and more of them until all PSD estimations of interest don't change significantly anymore. When working with a uniform distribution of bins, the number of pulses to propagate can be smaller than the number of bin because some bins will contain 0 pulses.

5.5 Supercontinuum Generation from a Single-Cavity Dual-Comb Laser

The method detailed in this chapter is used to corroborate the noise suppression dynamics observed in Chapter 4.

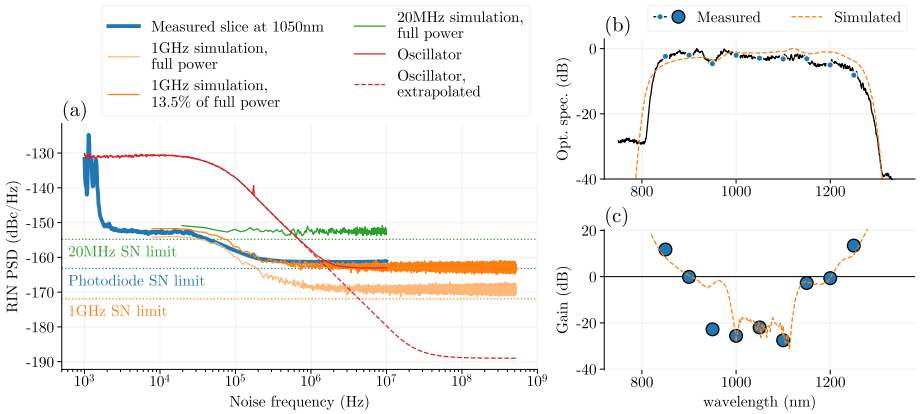

Figure 5.4: Comparison between measured and simulated RIN PSDs for 15 nm spectral slices. (a) Detailed PSDs for a slice centered at 1050 nm. We show in solid red the measured oscillator RIN PSD, dashed red the extrapolated curve used for the 1 GHz simulations and in solid, thick blue the measurement of the SC slice. In light orange is the PSD of the 1 GHz simulation at full power ($T = 1$ in Eq. (5.12)) while the attenuated one ($T = 0.135$) is shown in darker orange. A simulated 20 MHz repetition rate version of the experiment is shown in solid green. Dotted lines show the SN limit of each situation. (b) Measured and simulated optical spectra after nonlinear broadening in the ANDi fiber. Markers are placed on the simulated spectrum at the center wavelength of each slice. (c) Measured and simulated gain coefficients, which is the ratio of the mean PSD in the $[10\,\text{kHz}, 20\,\text{kHz}]$ interval between the oscillator each spectral slice.

Fig. 5.4 shows a detailed comparison between numerical and experimental results. The solid red curve in (a) shows the RIN PSD of the laser, measured after some attenuation. Attenuation raises the SN limit of the measurement, but is necessary because the 3 W of the laser far exceed the power ratings of the

photodiode. Without it, we would expect the PSD to hit a much lower noise floor, as projected by the dashed, red curve. As explained in Section 4.1.1, RIN must be measured in a spectrally resolved way. The measured wavelengths are highlighted in blue on Fig. 5.4(b), where we see good agreement between the measured and simulated optical spectra.

Because of the high repetition rate, we make use of the technique introduced in Section 5.4.3. Seeing that the highest measured noise frequency is only 10 MHz, it might be tempting to scale down average power and repetition rate in order to simulate a 20 MHz laser. However, it is clear by looking at Eq. (5.5) that doing so increases the shot noise limit of the simulation by 50 times. While this may be a viable solution in noisier situations, the initial noise measurement from the laser is already SN-limited, so increasing the SN limit is out of the question. We illustrate this by running such a simulation and plotting the results in green in Fig. 5.4(a). The simulated PSD is clamped by a noise floor so high that it is not possible to compare it with the measurement.

Instead of scaling down the repetition rate of the simulation, we aim to cover the range from 7.9 kHz to 1 GHz at once. Since the original noise PSD measurement doesn't extend past 10 MHz, we extrapolate it by extending its mean slope around 300 kHz down to the predicted noise floor of the laser at full power. Because of the huge frequency range to cover as well as the high number of segments ($K = 79$) necessary to sufficiently reduce the variance of the PSD estimations, the number of pulses to propagate using the GNLSE would exceed 5 millions. Yet, using the binning technique described above, we aimed to reduce this number to 16 000. Because of empty energy bins, the actual number of propagated pulses is 14 222. We also run a similar simulation targeting 10 000 pulses only and notice no difference in the resulting PSD estimations, confirming that 14 222 is adequate.

Using Eq. (5.12) with $T = 1$ to simulate a bandpass filter, we process each simulated pulse, compute their energy and create a signal of which we can estimate the PSD. An example is shown in Fig. 5.4(a) where the detailed PSDs of the slice around 1050 nm are shown. As illustrated by the faded orange curve, the SN limit of the $T = 1$ simulations is lower than that of the measurement shown in blue. Consequently, we also process the same set of simulated pulses with a lower value of T to match the experimental noise floor of each slice, as shown by the dark orange curve. This SN-matched simulation is in very good agreement with the experimental curve over the full overlapping frequency range.

To better summarize the relation between measurements and simulations, we compute the noise gain coefficient of each slice by dividing the mean RIN PSD of each slice between 10 kHz and 20 kHz by that of the oscillator in the same RF range. This coefficient is plotted in Fig. 5.4(c). For all slices except that at 950 nm, correspondence between measurements and simulations is excellent. Numerical simulations make it possible to easily estimate the noise gain function with high resolution. Thanks to the high resolution of the simulated noise gain function, it is clear that there exists a central section of the optical spectrum spanning 900 nm to 1200 nm where the noise gain is expected to be 0 or less.

To illustrate the origin of the noise suppression, the numerical model is used to show how the spectrally resolved noise gain evolves as the SC spectrum develops in the fiber. Fig. 5.5(a) shows the evolution of the noise gain as function of wavelength and propagation distance. In the first few centimeters, spectral

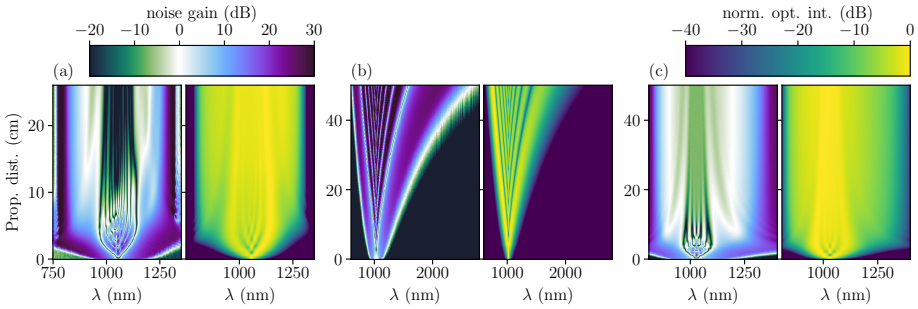

Figure 5.5: Simulated evolution of the noise gain spectrum as function of propagation distance. In each example, a sech^2, noisy pulse train is generated and propagated in a different fiber. The plot on the left shows the noise gain in dB as function of wavelength and distance while the plot on the right shows the normalized optical intensity for reference. (a) Same simulation as in Fig. 5.4. (b) Dispersion and other nonlinear effects are turned off to keep only SPM. (c) Same as (b) but with normal, second order dispersion.

peaks created by SPM are still visible. Aligned with those peaks are very localized regions of RIN suppression. After OWB occurs, the central part of the optical spectrum gets progressively smoother, which in turn creates a smooth region of noise suppression. One might presume that the true origin of this noise suppression is SPM alone, which acts to translate fluctuations in peak intensity into fluctuations in spectral width. This hypothesis accounts for the fact the spectral edges see substantial noise gain. However, it is incomplete, as shown on Fig. 5.5(b). When only SPM is simulated, the small regions of noise suppression never get smoothed out. When simply adding normal, second order dispersion ($\beta_2 > 0$), the entire noise gain evolution plays out in a manner almost identical to Fig. 5.5(a). This concludes that SPM and normal dispersion are the key ingredients to achieve substantial RIN suppression in SCG OFC at low RF frequencies.

5.6 Comparison with Other Models

As illustrated in Section 5.3, it is essential to distinguish between noise occurring at RF frequencies and noise occurring at optical frequencies. Measuring the RIN of a system as a single number in % is not a complete enough description of its noise properties. We would like to develop this idea further by comparing our model with two RF-agnostic models commonly found in the literature. First, as a baseline, we run a set of simulations using only shot noise [16, 39]. Then, we will use a "technical white noise (TWN)" approach where all noise except SN is considered to be technical [50, 126, 135, 136]. This is the approach used in Chapter 3. Finally, we will run a set of simulations using our new model by allocating noise as shown on Fig. 5.3.

For this test, 150 fs pulses are propagated through 18 cm of conventional fiber by solving Eq. (2.12) which includes arbitrarily high order dispersion, SPM, self-steepening and delayed Raman scattering using a measured gain spectrum [137]. We consider a 40 MHz laser with a center wavelength of 1550 nm, an average

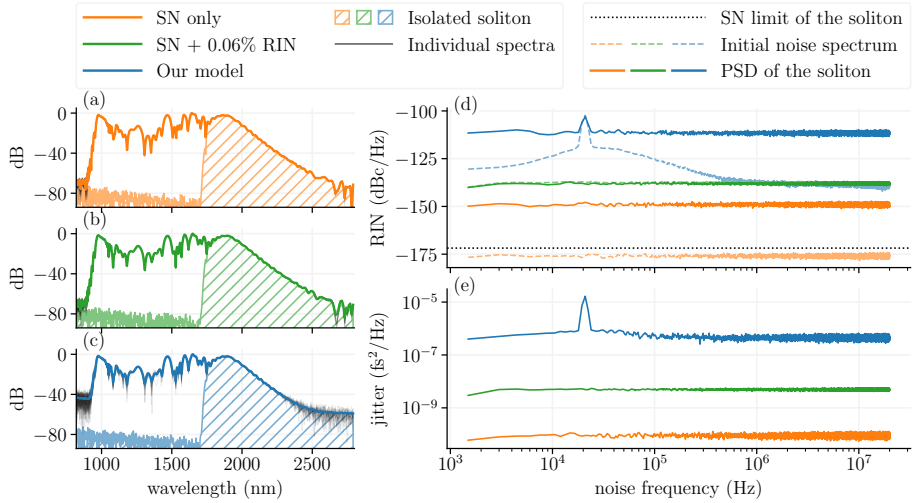

Figure 5.6: Results of different multi-shot simulation models on the same pulse and fiber parameters. (a) Optical spectra after propagation using a pulse train with SN only. We draw individual spectra as think black lines with their empirical mean in thick, colored lines. A longpass filtered soliton is highlighted with a hatched pattern. (b) and (c): same for inputs with 0.06 % technical white noise (TWN) and our model, respectively. Mean coherence $\langle|g_{12}|\rangle$ of the full spectrum is displayed on the upper right of each plot. (d) Faded, dashed lines show the RIN PSD of each initial pulse train while solid line show that of the soliton after propagation. A dotted black line indicates the SN limit of the soliton (Eq. (5.5)). (e) Timing jitter PSD of the soliton.

power of 100 mW (15.7 kW peak power) and enough simulations to cover low frequencies down to 1.5 kHz with a good reduction in variance ($K = 70$). For all three models, we used again the approach explained in Section 5.4.3 where only ~ 3000 pulses are propagated, instead of all 950 264 of them.

Optical spectra for all three models are shown on Fig. 5.6(a), (b) and (c). As expected from this combination of pump wavelength and fiber dispersion, the optical spectrum has a lot of complex structures, including a prominent soliton centered around 1880 nm. We isolate it using a 1750 nm longpass filter for further analysis, as shown by the hatched pattern. Notice how the attenuation does not get rid of the shot noise floor in the optical domain, as explained in Section 5.4.2. The RMS RIN and timing jitter σ_τ, of the input, the full SC spectrum and the isolated soliton, for every method, are displayed in Table 5.1. Together with the mean coherence $\langle|g_{12}|\rangle$, they are calculated according to:

$$\mathrm{RIN}_{\mathrm{RMS}} = \frac{\sqrt{\langle|E - \langle E\rangle|^2\rangle}}{\langle E\rangle}, \quad \tau_c = \frac{\int_{-\infty}^{\infty} \tau|A(\tau)|^2 \mathrm{d}\tau}{\int_{-\infty}^{\infty} |A(\tau)|^2 \mathrm{d}\tau}, \quad \sigma_\tau = \sqrt{\langle|\tau_c - \langle\tau_c\rangle|^2\rangle},$$
$$|g_{12}(\omega)| = \left|\frac{\langle \tilde{A}_j^*(\omega)\tilde{A}_k(\omega)\rangle_{j\neq k}}{\langle|\tilde{A}(\omega)|^2\rangle}\right|, \quad \langle|g_{12}|\rangle = \frac{\int_0^{\infty} |g_{12}(\omega)| \cdot \langle|\tilde{A}(\omega)|^2\rangle \mathrm{d}\omega}{\int_0^{\infty} \langle|\tilde{A}(\omega)|^2\rangle \mathrm{d}\omega} \tag{5.14}$$

RMS RIN			
	SN only	SN + 0.06 % RIN	Our model
Initial	$< 0.01\,\%$	$0.07\,\%$	$0.07\,\%$
Full spectrum	$< 0.01\,\%$	$0.07\,\%$	$0.17\,\%$
Soliton	$0.02\,\%$	$0.07\,\%$	$1.18\,\%$
Jitter			
	SN only	SN + 0.06 % RIN	Our model
Initial	< 1 as	< 1 as	28.1 as
Full spectrum	34.8 as	269.2 as	2494.4 as
Soliton	42.4 as	371.4 as	3015.7 as

Table 5.1: Summary of RMS RIN and timing jitter figures for all 3 models

where $\langle\,\rangle_{j\neq k}$ means that the empirical average is computed considering all possible combinations of 2 distinct pulses.

The input pulses of the SN-limited set of simulations is exactly that of Eq. (5.11) with $\eta = 1$. The corresponding RIN PSD is a straight line at the shot noise limit given by Eq. (5.5) and is shown on Fig. 5.6(d) as a faded, dashed orange line. We show the resulting optical spectra as well as the mean spectrum on Fig. 5.6(a).

For the next model, we target an RMS RIN of 0.06 %, which is the total RMS RIN of the measurement shown in Fig. 5.3(a). Because this is essentially TWN, the RIN PSD is flat and, with the laser parameters given above, its level is about -140 dBc/Hz, shown as the dashed, faded green line in Fig. 5.6(d). This level is reached by multiplying the peak power of each pulse by a number sampled on a normal distribution of mean 1 and standard deviation of 0.06 %.

Finally, we run the same simulations using our model, using $\eta \approx 18.3$ to amplify noise in the optical domain, and using the procedure of Section 5.4 to create a realistic sequence of peak power variations. The final RIN PSD of the input pulse train matches the measurement of Fig. 5.3(a), as shown on Fig. 5.6(d) in faded, dashed blue. The only difference with Fig. 5.3(a) is an artificial spike added at 20 kHz.

In the optical domain, it is clear that adding only technical noise on top of SN doesn't affect the OSNR, while our approximation of ASE does. With our model, the optical noise floor is about 25 dB higher, matching the $\eta^2 \approx 10^{25/10}$ of the input. Accordingly, spectra with ASE appear nosier, with more extreme excursions from the mean, resulting in a low coherence. While less dramatic, the TWN also shows slightly stronger fluctuations on the long wavelength side of the spectrum, but is overall very similar to the results of the SN-only simulations.

As previously mentioned, resolving RIN across the optical spectrum is necessary to get a full picture of the noise dynamics. For this artificial example, it is natural to do so by isolating the redshifted soliton around 1880 nm with a longpass filter. The RIN PSD of this soliton is plotted in solid lines for all 3 models on Fig. 5.6(d). The SN limit of this filtered pulse train is indicated with a dotted, black line. First, we notice a 25 dB gain in the RIN of the SN-limited simulations. Similar gain is observed in the high frequency end of the simulations performed with our model. However, no significant noise amplification is seen in the TWN simulations. We can conclude that technical noise is not amplified in this situation. Even though the same SN level is present at

the input, its amplification, as seen in the pure SN case, is not visible because of its low level relative to the technical noise. Finally, our model can demonstrate these two behaviors at the same time, which is where the added spike at 20 kHz comes in handy. Unlike the strong amplification of incoherent noise on the high frequency side, the top of the spike, consisting mainly of technical noise, does not experience significant gain. In other words, the conventional SCG process is responsible for a strong amplification of quantum noise, which results in a higher, flattened RIN PSD in the RF domain, especially at high RF frequencies. Nevertheless, when the majority of the RIN present in a particular frequency band consists of mainly technical noise, the impact of SCG on this noise is different, which our model demonstrates.

Although no timing jitter is explicitly introduced into the simulation, we find that both optical domain noise and pulse-to-pulse fluctuations induce a significant timing jitter. Therefore, the shape of the RIN PSD is imprinted on the timing jitter PSD. Although our RF-resolved model makes the coupling between RIN and timing jitter more visually explicit, it can also be inferred by looking at Table 5.1. Typically, noisier inputs exhibit higher jitter, in both the full SC spectrum and in the isolated soliton. This again highlights the importance of distinguishing between noise in the optical domain and pulse-to-pulse fluctuations: even though the RMS RIN at the input is identical, our model predicts about an order of magnitude higher timing jitter after nonlinear broadening, which can have a large impact on coherence [50].

5.7 Conclusions

We presented a set of numerical tools that allow existing pulse propagation processes to simulate and analyze the evolution of noise PSDs. Although noise analysis via PSD estimation and other statistical methods is already a mature subject and can be used in the context of SCG, we identified a lack of tools that would allow researchers to simulate an entire pulse train. We contributed a flexible, physically motivated procedure that turns a measured noise PSD into a realistic pulse train that can be propagated using any suitable equation. We provided detailed formulas and explanations of our method, focusing mainly on RIN due to its relevance in a wide range of applications. Because our framework is fairly general, it is easy to integrate it in existing pulse propagation software. Furthermore, we emphasize that the techniques presented here can be applied to many different types of noise, including several at the same time.

We foresee our method being applied in many ultrafast domains, including to the study of coupling between RIN and phase noise in the context of electro-optic and parametric frequency combs. Typical applications of these are very sensitive to phase noise, which can be induced by RIN, which itself originates from electronic noise in the modulators. Understanding the interplay between these two types of noise is critical to achieving octave-spanning combs with minimal linewidth over a wide spectral range. In addition, our approach allows researchers to numerically estimate how much noise can be suppressed given its distribution across RF frequencies.

Chapter 6

Supercontinuum Generation in Hollow-Core Fibers

Experimental work in this chapter was performed in collaboration with Anupamaa Rampur.

As the name implies, hollow-core (HC) fibers consist of a hollow core, usually filled with air, surrounded by a more or less complex cladding structure. While a simple, hollow silica tube can be considered the simplest type of HC fiber, researchers have developed numerous sophisticated cladding structures in order to reduce transmission and bend losses and to favor single-mode operation. Their advantages over conventional, solid-core fibers are numerous. (i) In telecommunications, their reduced dispersion and nonlinearities as well as their low refractive index mean that data can be transmitted at higher rates with lower latency [138]. (ii) In industrial applications, their low material absorption and high damage threshold make them a practical, flexible alternative to free-space optics for high power delivery [139, 140]. (iii) In the field of sensing, their ability to be filled with different gases while guiding light enables new gas sensing schemes [141, 142].

Moreover, in the field of photonics itself, they enable an attractive new regime of high power pulse compression and SCG [143, 144]. Of particular interest are the simple hollow capillary tubes. When held perfectly straight, their unparalleled broadband transmission window, coupled with their potentially very large core, enables the generation and transmission of high peak power deep UV pulses [19, 145, 146], which can be used in applications such as ultrafast spectroscopy.

The aim of this project was to become familiar with working with hollow-core fibers and capillary tubes. Given the very high power and low repetition rate of these systems, reproducing some of the recent results in HC SCG would have opened the door to a new regime of noise analysis. Unfortunately, problems with laser availability and general technical challenges slowed down this project considerably and only preliminary results are available.

6.1 Dispersion and Nonlinearities in Hollow-Core Fibers

Guiding in hollow capillary tubes is described by the Marcatili model [147]. For a core radius of a, the effective refractive index and attenuation coefficient of the HE_{nm} mode are given by:

$$\begin{aligned} n_{\mathrm{eff}}(\omega) &= \sqrt{n_{\mathrm{gas}}^2 - \left(\frac{u_{km}c}{\omega a}\right)} \\ \alpha(\omega) &= \frac{\chi_e + 2}{\sqrt{\chi_e}} \left(\frac{u_{km}c}{\omega}\right)^2 \frac{1}{a^3} \end{aligned} \tag{6.1}$$

where u_{km} is the mth root of the Bessel function of the first kind of order $k-1$, and $\chi_e = n_{\mathrm{clad}}^2 - 1$ is the electric susceptibility of the cladding material. The refractive index of the gas n_{gas} as well as its nonlinear refractive index can be pressure and temperature adjusted based on number densities calculated with an equation of state, such as the ideal gas law [144]. It is then possible to compute the dispersion parameters with Eq. (2.1).

Fig. 6.1 shows the dispersion of a capillary according to this model for a selection of core diameters and gas pressures. This illustrates that the ZDW of HC fibers can be easily tuned by adjusting gas pressure.

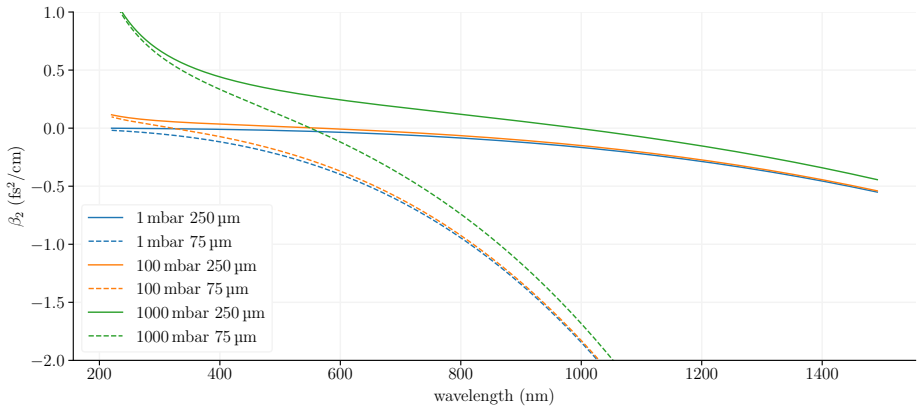

Figure 6.1: Prediction, according to the Marcatili model, of the GVD of an Argon-filled capillary considering 2 different core diameters and 3 different pressure points.

6.2 Gas Cell Design

Unlike solid-core, Silica fibers, HC fibers don't benefit from a thriving ecosystem of fiberized components. Therefore, a robust but flexible system is required to integrate them into a free-space setup, with the specific requirement that this system must isolate the interior of the fiber from its external environment. It is possible to control the type and the pressure of the gas inside the fiber, allowing fine-tuning of dispersion and nonlinearities.

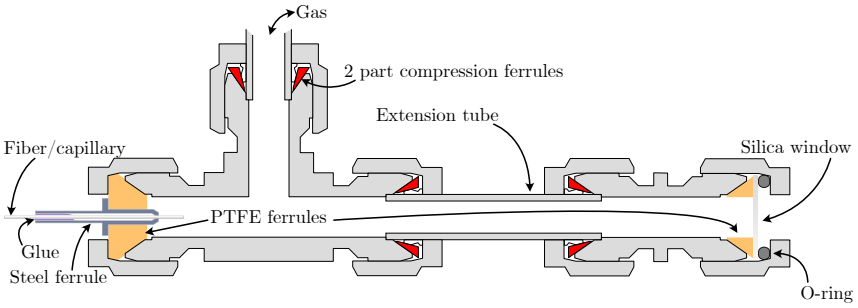

Figure 6.2: Schematic side cut of the gas cell design.

Since this work is rather exploratory, our intention is to design a gas cell that works with HC fibers and capillaries of all sizes and that is affordable. Special attention will be given to the following requirements:

- Swapping fibers of different length and diameters must be easy and quick.
- Mechanical precision of the alignment of the fiber must be on par with standard components made for solid-core optical fibers.
- The system must be airtight and must have the capability to maintain a pressure gradient across the fiber.
- As many parts as possible must be commercially available.

The goal of this system is to be able to work with HC fibers and capillaries at pressures ranging from rough vacuum to multiple bars. A schematic of the fiber holding design is shown in Fig. 6.2. The main component is a standard, steel T-junction (Swagelok SS-6M0-3) designed for gas pipes. Its intended use is to fit 6 mm tubes at each end. This is done with the help of a two-part ferrule together with a screw-in cap. At the gas inlet, we use this intended design with a flexible, 6 mm PFA tube and the stock compression fittings.

On the other side of the gas cell, a Silica window is sandwiched between an O-ring and a PTFE ferrule. This ferrule has a hole of 6 mm, such that it does not obstruct the beam. Again, we obtain a tight seal when the cap is screwed in and compresses the O-ring, window and ferrule against the conical opening. The choice of windows, especially their thickness, is motivated by the difficult to find balance between nonlinearities and mechanical robustness. On the one hand, high peak intensity beams focused on a narrow spot experience a lot of nonlinearities in the glass, such as spectral broadening and self-focusing. This is undesirable because it means that in order to achieve a good coupling of the beam in the fiber, we must always work with the beam at full power, which is likely to damage the fiber end facet if the alignment is not perfect. On the other hand, because this work emphasizes the use of standard components, the fit between the window and the other components is not perfect. As a result, the

window experiences more stress than would be ideal and is more susceptible to breakage. For the experiments presented here, mechanical robustness is favored, and a 0.5 mm window is chosen.

To install the fiber in the system, we first glue it into a 2.5 mm outer diameter steel ferrule. A short piece of fiber sticks out of the ferrule to facilitate this process and can be cleaved later. This steel ferrule then fits snugly into a PTFE ferrule, which, when the cap is screwed tight, creates an airtight seal between the gas cell and the steel ferrule. A simpler design would be to fit the fiber directly into a PTFE ferrule with the appropriately sized hole. However, in our experience, some HC fibers, especially those with a thin cladding, can deform when compressed too much. With the help of this steel ferrule and the glue, direct compression of the fiber is no longer necessary to achieve an airtight seal while holding the fiber firmly in place. The gas cell can then be fixed onto a standard mounting plate (Thorlabs MMP1/M and similar) with a simple, custom-made bracket, to then be installed on a 5-axis stage.

A disadvantage of this system is that we don't get the best mechanical stability. The reason is that the fiber is still indirectly resting on a PTFE part. Since PTFE is easily deformed, tightening the cap to create a good seal will inevitably move the fiber around. This is particularly relevant for capillaries, as they must be kept as straight as possible to minimize loss, although the operating range of the stages we use largely eliminate this problem.

Most parts can be directly bought from a supplier and those that can't are fairly easy to manufacture. Please note that PTFE ferrules wear off quickly, and that steel ferrules are glued to the fiber. Therefore, these parts should be considered as consumables and having a good stock of them is convenient.

6.3 Experiment

In this work, we use two HC Silica fibers. The first one is an antiresonant, 59 cm revolver-type HC-PCF nicknamed B05. An scanning electron microscope image of its cross-section is shown in Fig. 6.3(a). Its 75 µm core is formed by a ring of 7 evenly spaced 47 µm capillaries. It was produced in the Photonics and Optoelectronics institute at the University of Southampton. The second one, CAP250, is a 92 cm polyimide coated 250 µm hollow capillary tube. Its 665 µm outer diameter makes it rigid, thus minimizing the typically massive bend from which hollow capillary tube suffer.

The pump used for SCG consists of a 800 nm, 1 kHz Ti:sapphire laser that we spectrally broaden by tightly focusing its beam in free space, such that the Kerr effect broadens its spectrum. We then use a pair of chirped mirror to compress these pulses down to 10.5 fs (measured with frequency-resolved optical gating [148]). This compression setup is a simplified version of that used in [149], as the tight focusing in air is enough and no thin Silica plate is required. The available pulse energy is 410 µJ.

Fig. 6.4 shows a schematic of the experiment. Because of the short pulse duration and high peak intensity, use of transmissive optical components must be limited. Therefore, we couple the compressed pulses into the FUT with a spherical mirror. We choose a 300 mm focal length mirror for the B05 antiresonant fiber and a 750 mm mirror for the hollow capillary tube. Care must be taken to minimize the angle of incidence on the spherical mirror to avoid aberrations.

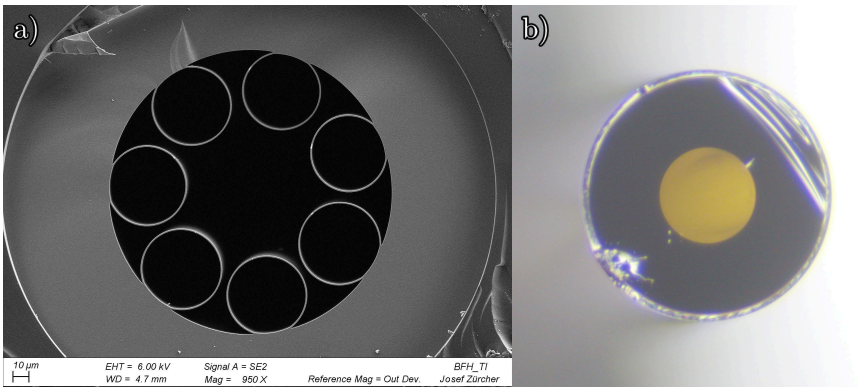

Figure 6.3: End view of both fibers used in this work. (a) scanning electron microscope image of the B05 hollow-core photonic crystal fiber. (b) Microscope image of the 250 µm capillary.

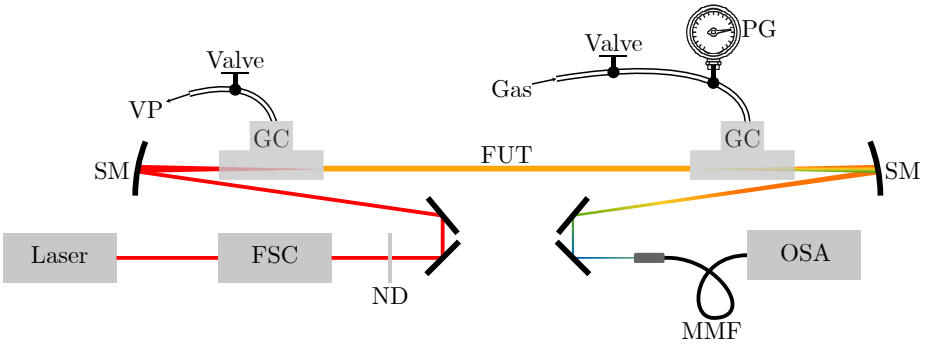

Figure 6.4: Schematic of the experiment. FSC: free space compressor; FUT: fiber under test; GC: gas cell; MMF: multimode fiber; ND: variable neutral density filter; OSA: optical spectrum analyzer; PG: pressure gauge SM: spherical mirror; VP: vacuum pump.

Our gas cell design helps here: the compression fitting and the O-ring secure the window without taking a lot of space laterally. We can adjust the power coupled into the fiber with a transmissive, variable neutral denstiy filter placed before the spherical mirror. At the fiber output, we use a spherical mirror to focus the SC light onto a large core multimode fiber connected to a spectrometer (ASEQ Instruments LR1).

The gas cell that houses the fiber input is connected to a vacuum pump. To control the gas pressure in the fiber, two needle valves are placed on the gas line close to the input and output gas cells. After flushing the fiber with the desired gas, pressure gradients can be achieved across it by turning on the pump while gas is flowing in the other gas cell. This system only allows for pressure gradients in one direction, with lower pressure at the optical input. This allows the dispersion and nonlinear refractive index of the fiber to be adjusted axially, similarly to a solid-core fiber taper.

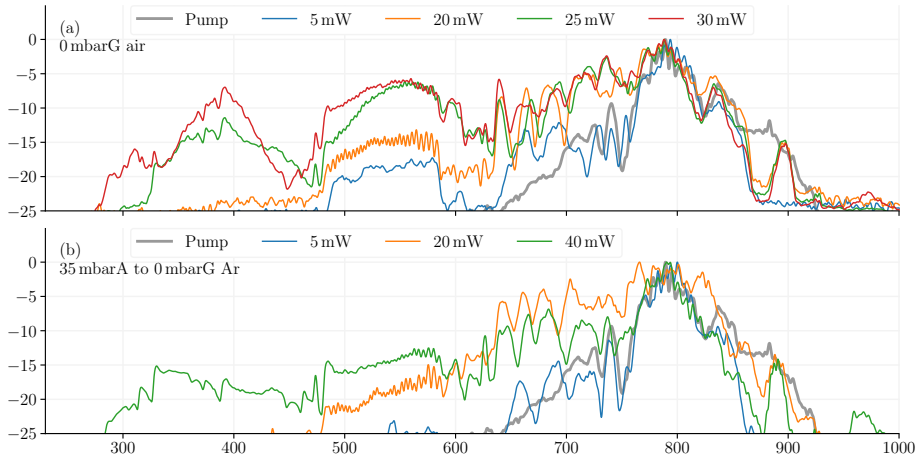

Figure 6.5: SC spectra generated in B05 at different pump powers. (a) The fiber is filled with atmospheric pressure air. (b) Argon is flown through the fiber to achieve a pressure gradient over the interaction length. The input of the fiber is at 35 mbarA and the output at atmospheric pressure.

Fig. 6.5 shows SC spectra generated in the B05 fiber. The spectrum of the input compressed pulse, with its already fairly complex structure, is shown in faded gray for comparison. Spectra on Fig. 6.5(a) are generated in atmospheric pressure air. Unfortunately, we observe no spectral broadening in the long wavelength side due to the poor sensitivity of the available spectrometer. Compared to the pump, we see that 5 mW of power is already enough to generate features around 500 nm. Going from 5 mW to 20 mW doesn't expand the spectral bandwidth by a lot, but power between 600 nm and 750 nm increases. Then, a small step up in pump power to 25 mW results in a substantial increase of SC bandwidth, which is expanded a bit further going to 30 mW. We suspect that self-focusing close to the fiber input is changing the coupling efficiency with changing pump power. This would explain the reduction from 62 % coupling efficiency at 5 mW down to 41 % at 30 mW.

For the next set of measurements, we flush the fiber with Argon and establish a pressure gradient with the help of the vacuum pump. The pressure at the fiber input is maintained at 35 mbarA and increases up to atmospheric pressure at the output. Although the nonlinear refractive index of Argon is 2 to 4 times lower than that of air [150], their dispersion profile is very similar [151] and therefore, we expect to require slightly higher pump power to obtain similar spectra as in the previous experiment. This is confirmed by Fig. 6.5(b): 40 mW are required to get a spectrum comparable to that achieved with 30 mW in atmospheric pressure air. Surprisingly, the SC bandwidth at 20 mW is identical in both experiments. Because we observe the same decrease in coupling efficiency as with the previous experiment, we argue that self-focusing is primarily taking place in the silica window.

We conduct a similar set of experiments with CAP250. Because it is a capillary with no guiding structure, it must be kept perfectly straight. This is made easier by choosing a capillary with a thick cladding, resulting in a very

stiff fiber. By applying a little bit of tension, we avoid the fiber sagging over its 92 cm length and achieve a 50 % coupling efficiency at 5 mW pump power. Like with the B05 fiber, this efficiency drops as we increase power and reaches a minimum of 25 % at 410 mW. After flushing this fiber with Argon, we drop the pressure to 23 mbarA. With a constant 256 mW pump power, we increase the pressure up to 1.7 barA. As shown on Fig. 6.6(a), even at the lowest pressure, we can observe a little bit of spectral broadening. Changing the pressure to 488 mbarA increases the nonlinear refractive index by a factor of ~ 20, which results in a broader spectrum. However, more than tripling this pressure does not cause further impact.

We run a final experiment where the pressure is kept at 1707 mbarA, and we vary the pump power from 10 mW to 410 mW. Spectra are similar to the previous ones presented above. We also capture an image of the far field at the output of the fiber blocking the beam with a piece of white paper. The color pattern shown on Fig. 6.6(c) demonstrates that chromatic aberration and the highly multimode nature of such a large core fiber play an important role.

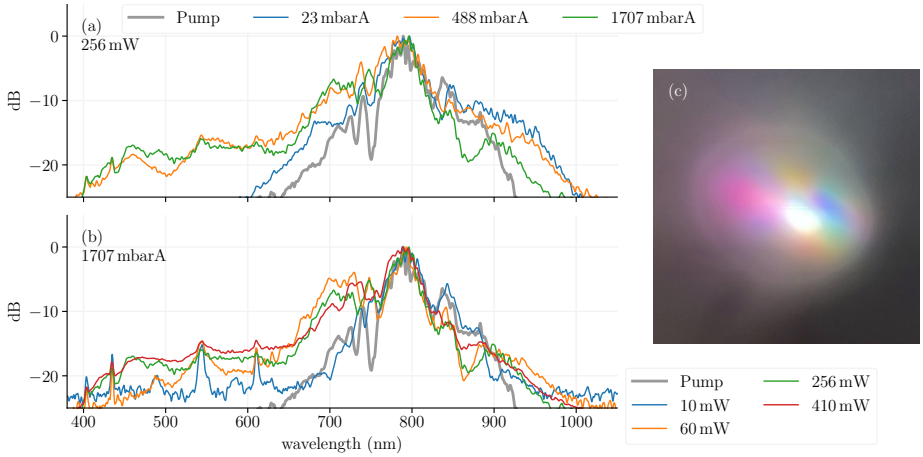

Figure 6.6: SC spectra generated in an Argon-filled CAP250. (a) Pressure ramp with a constant 256 mW pump. (b) Power ramp with a constant 1707 mbarA pressure. (c) Picture of the far field at the fiber output.

6.4 Conclusions

This chapter explored the surface of SCG in HC fibers. It shed light on the fact that a good gas cell design is essential for conducting HC SCG experiments. Indeed, at high pulse energies, self-focusing occurring in the input window can affect coupling efficiencies, which in turns impacts the resulting SC spectra. In an effort to facilitate easy and cost-effective reproducibility, this work has taken an approach that favors commercially available parts, even if they are not necessarily designed for use in optical experiments. Nevertheless, broad SC spectra were obtained in both a hollow capillary tube and an antiresonant HC-PCF.

This system proved difficult to adapt to the high pulse energies required for such large core fibers. Because of its compactness, its input window must be placed relatively close to the fiber entrance, which increases the likelihood of coupling losses due to self-focusing. Therefore, future experiments performed with this system should use lower pulse energies in conjunction with smaller core fibers. This approach would mitigate the negative effects of self-focusing and lead to improved results.

Chapter 7

Conclusions and Outlook

The primary objective of this thesis was to push the limits of low noise supercontinuum generation. Recently, researchers in ultrafast optics have paid more attention to the noise performance of these light sources. Applications of SC-based OFCs, such as ultra-high resolution optical coherence tomography or multimodal nonlinear imaging, benefit greatly from low noise sources. This thesis contributes two significant developments in this area. First, it presents a hybrid fiber approach as a solution to the trade-off between conventional and ANDi SCG: it uses anomalous pumping to compress the input pulse and reach high peak powers, then OWB to obtain a flat and smooth SC spectrum, all of that while keeping RIN exceptionally low.

Achieving this goal required a thorough numerical understanding of the noise properties of ultrafast pulses and their evolution as they propagate and broaden in nonlinear optical fibers. Despite its importance, little research had previously been done in this area. Consequently, this work placed a strong emphasis on the development of high-quality numerical simulations, culminating in the creation of a new framework for simulating realistic, noisy pulse trains. This model is the second major result of this thesis. Its development was prompted by the demonstration of SN-limited dual-comb supercontinuum generation with >1 W average power, which involved a suppression of RIN by up to 20 dB in parts of the optical spectrum. Numerical simulations using this new model were able to reproduce these measurements and provide an insight into their physical origin. Undoubtedly, this numerical framework is poised to become an essential tool for the advancement of future OFC technologies. As these devices find more and more applications across various fields, their stability, bandwidth, and power requirements are also increasing.

Future research in this area will focus on adapting the hybrid fiber concept of Chapter 3 to other wavelength ranges or pump parameters. For example, using the numerical model developed in Chapter 5, it may be possible to design a hybrid fiber for 1 µm pumping that results in SN-limited OFCs, like the results presented in Chapter 4, but with an even broader optical spectrum, or lower pump power requirements. This may pave the way to more compact, yet exceptionally fast and performant spectroscopic or ranging devices.

Bibliography

[1] T. W. Hänsch. "Passion for precision (Nobel lecture)". In: *ChemPhysChem* 7.6 (2006), pp. 1170–1187.

[2] J. L. Hall. "Nobel Lecture: Defining and measuring optical frequencies". In: *Reviews of modern physics* 78.4 (2006), pp. 1279–1295.

[3] NobelPrize.org. *The Nobel Prize in Physics 2023*. `https://www.nobelprize.org/prizes/physics/2023/press-release/`. Consulted 30 Sept. 2024. Oct. 2023.

[4] S. A. Diddams, K. Vahala, and T. Udem. "Optical frequency combs: Coherently uniting the electromagnetic spectrum". In: *Science* 369.6501 (2020), eaay3676.

[5] T. Fortier and E. Baumann. "20 years of developments in optical frequency comb technology and applications". In: *Communications Physics* 2.1 (2019), pp. 153–168. DOI: 10.1038/s42005-019-0249-y.

[6] J. Riemensberger et al. "Massively parallel coherent laser ranging using a soliton microcomb". In: *Nature* 581.7807 (2020), pp. 164–170.

[7] C. Prayoonyong et al. "Frequency comb distillation for optical superchannel transmission". In: *Journal of Lightwave Technology* 39.23 (2021), pp. 7383–7392.

[8] Z. Wang et al. "Magnonic frequency comb through nonlinear magnon-skyrmion scattering". In: *Physical Review Letters* 127.3 (2021), p. 037202.

[9] I. Coddington, N. Newbury, and W. Swann. "Dual-comb spectroscopy". In: *Optica* 3.4 (2016), pp. 414–426.

[10] A. J. Metcalf et al. "Stellar spectroscopy in the near-infrared with a laser frequency comb". In: *Optica* 6.2 (2019), pp. 233–239.

[11] P. Russell. "Photonic crystal fibers". In: *science* 299.5605 (2003), pp. 358–362.

[12] A. Rampur et al. "Perspective on the next generation of ultra-low noise fiber supercontinuum sources and their emerging applications in spectroscopy, imaging, and ultrafast photonics". In: *Applied physics letters* 118.24 (2021), p. 240504. URL: https://doi.org/10.1063/5.0053436.

[13] M. Jensen et al. "Noise of supercontinuum sources in spectral domain optical coherence tomography". In: *J. Opt. Soc. Am. B* 36.2 (Feb. 2019), A154–A160. DOI: 10.1364/JOSAB.36.00A154. URL: http://josab.osa.org/abstract.cfm?URI=josab-36-2-A154.

[14] J. Dudley, G. Genty, and S. Coen. "Supercontinuum generation is photonic crystal fiber". In: *Rev. Mod. Phys.* 78 (Oct. 2006), pp. 1135–1184. DOI: 10.1103/RevModPhys.78.1135.

[15] N. R. Newbury et al. "Noise amplification during supercontinuum generation in microstructure fiber". In: *Optics letters* 28.11 (2003), pp. 944–946.

[16] K. L. Corwin et al. "Fundamental Noise Limitations to Supercontinuum Generation in Microstructure Fiber". In: *Phys. Rev. Lett.* 90.11 (Mar. 2003), p. 113904. DOI: 10.1103/PhysRevLett.90.113904.

[17] A. S. Mayer et al. "Offset-Free Gigahertz Midinfrared Frequency Comb Based on Optical Parametric Amplification in a Periodically Poled Lithium Niobate Waveguide". In: *Phys. Rev. Appl.* 6 (5 Nov. 2016), p. 054009. DOI: 10.1103/PhysRevApplied.6.054009. URL: https://link.aps.org/doi/10.1103/PhysRevApplied.6.054009.

[18] R. Paschotta. "Noise of mode-locked lasers (Part I): numerical model". In: *Applied Physics B* 79 (2004), pp. 153–162.

[19] J. C. Travers et al. "High-energy pulse self-compression and ultraviolet generation through soliton dynamics in hollow capillary fibres". In: *Nature Photonics* 13.8 (2019), pp. 547–554.

[20] G. P. Agrawal. *Nonlinear Fiber Optics*. 3rd ed. Academic Press, 2007. Chap. 2. ISBN: 0-12-045143-3.

[21] G. Genty, S. Coen, and J. M. Dudley. "Fiber supercontinuum sources (Invited)". In: *J. Opt. Soc. Am. B* 24.8 (Aug. 2007), pp. 1771–1785. DOI: 10.1364/JOSAB.24.001771. URL: http://josab.osa.org/abstract.cfm?URI=josab-24-8-1771.

[22] J. M. Dudley and J. R. Taylor. *Supercontinuum generation in optical fibers*. Cambridge University Press, 2010.

[23] R. Alfano, ed. *The supercontinuum laser source (3rd edition)*. Springer, New York, 2016.

[24] Z. Eslami et al. "Low-noise octave-spanning mid-infrared supercontinuum generation in a multimode chalcogenide fiber". In: *arXiv preprint arXiv:2003.03864* (2020).

[25] C. R. Smith et al. "Low-noise tunable deep-ultraviolet supercontinuum laser". In: *Scientific Reports* 10.1 (2020), p. 18447.

[26] E. Genier et al. "Ultra-flat, low-noise, and linearly polarized fiber supercontinuum source covering 670–1390 nm". In: *Optics Letters* 46.8 (2021), pp. 1820–1823.

[27] T. Brabec and F. Krausz. "Nonlinear optical pulse propagation in the single-cycle regime". In: *Physical Review Letters* 78.17 (1997), p. 3282.

[28] N. Karasawa et al. "Comparison between theory and experiment of nonlinear propagation for a-few-cycle and ultrabroadband optical pulses in a fused-silica fiber". In: *IEEE Journal of Quantum Electronics* 37.3 (2001), pp. 398–404.

[29] M. J. Weber, D. Milam, and W. L. Smith. "Nonlinear Refractive Index Of Glasses And Crystals". In: *Optical Engineering* 17.5 (1978), p. 175463. DOI: 10.1117/12.7972266. URL: https://doi.org/10.1117/12.7972266.

[30] T. Georges, D. Le Guen, and F. Favre. *Optical fiber transmission system with chromatic dispersion compensation*. US Patent 6,487,005. Nov. 2002.

[31] C. Finot et al. "Beneficial impact of wave-breaking for coherent continuum formation in normally dispersive nonlinear fibers". In: *J. Opt. Soc. Am. B* 25.11 (Nov. 2008), pp. 1938–1948. DOI: 10.1364/JOSAB.25.001938. URL: http://josab.osa.org/abstract.cfm?URI=josab-25-11-1938.

[32] J. Lægsgaard. "Mode profile dispersion in the generalized nonlinear Schrö dinger equation". In: *Opt. Express* 15.24 (Nov. 2007), pp. 16110–16123. DOI: 10.1364/OE.15.016110. URL: http://www.opticsexpress.org/abstract.cfm?URI=oe-15-24-16110.

[33] J. Hult. "A Fourth-Order Runge–Kutta in the Interaction Picture Method for Simulating Supercontinuum Generation in Optical Fibers". In: *J. Lightwave Technol.* 25.12 (Dec. 2007), pp. 3770–3775. URL: http://jlt.osa.org/abstract.cfm?URI=jlt-25-12-3770.

[34] A. Rieznik et al. "Optimum integration procedures for supercontinuum simulation". In: *IEEE Photonics Journal* 4.2 (2012), pp. 552–560.

[35] S. Balac. "High order embedded Runge-Kutta scheme for adaptive step-size control in the Interaction Picture method". In: *Journal of the Korean Society for Industrial and Applied Mathematics* 17.4 (2013), pp. 238–266.

[36] C. R. Harris et al. "Array programming with NumPy". In: *Nature* 585.7825 (Sept. 2020), pp. 357–362. DOI: 10.1038/s41586-020-2649-2. URL: https://doi.org/10.1038/s41586-020-2649-2.

[37] P. Virtanen et al. "SciPy 1.0: Fundamental Algorithms for Scientific Computing in Python". In: *Nature Methods* 17 (2020), pp. 261–272. DOI: 10.1038/s41592-019-0686-2.

[38] J. D. Hunter. "Matplotlib: A 2D graphics environment". In: *Computing in Science & Engineering* 9.3 (2007), pp. 90–95. DOI: 10.1109/MCSE.2007.55.

[39] A. M. Heidt et al. "Limits of coherent supercontinuum generation in normal dispersion fibers". In: *J. Opt. Soc. Am. B* 34.4 (Apr. 2017), pp. 764–775. DOI: 10.1364/JOSAB.34.000764. URL: http://josab.osa.org/abstract.cfm?URI=josab-34-4-764.

[40] C.-M. Chen and P. L. Kelley. "Nonlinear pulse compression in optical fibers: scaling laws and numerical analysis". In: *J. Opt. Soc. Am. B* 19.9 (Sept. 2002), pp. 1961–1967. DOI: 10.1364/JOSAB.19.001961. URL: http://josab.osa.org/abstract.cfm?URI=josab-19-9-1961.

[41] M. Nakazawa et al. "Coherence Degradation in the Process of Supercontinuum Generation in an Optical Fiber". In: *Opt. Fiber Technol.* 4.2 (1998), pp. 215–223. ISSN: 1068-5200. DOI: https://doi.org/10.1006/ofte.1998.0253. URL: https://www.sciencedirect.com/science/article/pii/S106852009890253X.

[42] U. Møller and O. Bang. “Intensity noise in normal-pumped picosecond supercontinuum generation, where higher-order Raman lines cross into anomalous dispersion regime”. In: *Electron. Lett.* 49.1 (2013), pp. 63–65.

[43] N. Bloembergen and Y. Shen. “Coupling between vibrations and light waves in Raman laser media”. In: *Physical Review Letters* 12.18 (1964), p. 504.

[44] S. Coen et al. “Supercontinuum generation by stimulated Raman scattering and parametric four-wave mixing in photonic crystal fibers”. In: *JOSA B* 19.4 (2002), pp. 753–764.

[45] S. Coen, D. A. Wardle, and J. D. Harvey. “Observation of Non-Phase-Matched Parametric Amplification in Resonant Nonlinear Optics”. In: *Phys. Rev. Lett.* 89 (27 Dec. 2002), p. 273901. DOI: 10.1103/PhysRevLett.89.273901. URL: https://link.aps.org/doi/10.1103/PhysRevLett.89.273901.

[46] F. Vanholsbeeck, P. Emplit, and S. Coen. “Complete experimental characterization of the influence of parametric four-wave mixing on stimulated Raman gain”. In: *Opt. Lett.* 28.20 (2003), p. 1960. ISSN: 0146-9592. DOI: 10.1364/ol.28.001960.

[47] N. Nishizawa et al. “Octave Spanning Coherent Supercontinuum Comb Generation Based on E r-Doped Fiber Lasers and Their Characterization”. In: *IEEE Journal of Selected Topics in Quantum Electronics* 24.3 (2018), pp. 1–9.

[48] N. Nishizawa and J. Takayanagi. “Octave spanning high-quality supercontinuum generation in all-fiber system”. In: *J. Opt. Soc. Am. B* 24.8 (2007), pp. 1786–1792. URL: http://josab.osa.org/abstract.cfm?URI=josab-24-8-1786.

[49] M. Klimczak et al. “Direct comparison of shot-to-shot noise performance of all normal dispersion and anomalous dispersion supercontinuum pumped with sub-picosecond pulse fiber-based laser”. In: *Sci. Rep.* 6.1 (2016), p. 19284.

[50] B. Sierro and A. M. Heidt. “Noise amplification in all-normal dispersion fiber supercontinuum generation and its impact on ultrafast photonics applications”. In: *OSA Continuum* 3.9 (2020), pp. 2347–2361.

[51] S. Rao D.S. et al. “Ultra-low-noise supercontinuum generation with a flat near-zero normal dispersion fiber”. In: *Opt. Lett.* 44.9 (May 2019), pp. 2216–2219. DOI: 10.1364/OL.44.002216. URL: http://ol.osa.org/abstract.cfm?URI=ol-44-9-2216.

[52] M. Klimczak et al. “Coherent supercontinuum generation in soft glass photonic crystal fibers”. In: *Photonics Res.* 5.6 (2017), pp. 710–727.

[53] K. Tarnowski et al. “Polarized all-normal dispersion supercontinuum reaching 2.5 μm generated in a birefringent microstructured silica fiber”. In: *Opt Express* 25.22 (2017), pp. 27452–27463.

[54] A. Hartung et al. “Design and fabrication of all-normal dispersion nanohole suspended-core fibers”. In: *J. Opt. Soc. Am. B* 36.12 (2019), pp. 3404–3410.

[55] Y. Liu et al. “Suppressing short-term polarization noise and related spectral decoherence in all-normal dispersion fiber supercontinuum generation”. In: *J. Lightwave Technol.* 33.9 (2015), pp. 1814–1820.

[56] I. B. Gonzalo, R. D. Engelsholm, and O. Bang. “Noise study of all-normal dispersion supercontinuum sources for potential application in optical coherence tomography”. In: *2nd Canterbury Conference on OCT with Emphasis on Broadband Optical Sources*. Vol. 10591. International Society for Optics and Photonics. 2018, p. 105910C.

[57] G. P. Agrawal, P. L. Baldeck, and R. R. Alfano. “Modulation instability induced by cross-phase modulation in optical fibers”. In: *Phys. Rev. A* 39 (7 Apr. 1989), pp. 3406–3413. DOI: 10.1103/PhysRevA.39.3406. URL: https://link.aps.org/doi/10.1103/PhysRevA.39.3406.

[58] E. Genier et al. “Cross-phase modulation instability in PM ANDi fiber-based supercontinuum generation”. In: *Opt. Lett.* 45.13 (July 2020), pp. 3545–3548. DOI: 10.1364/OL.397106. URL: http://ol.osa.org/abstract.cfm?URI=ol-45-13-3545.

[59] J. S. Feehan and J. H. Price. “Decoherence due to XPM-assisted Raman amplification for polarization or wavelength offset pulses in all-normal dispersion supercontinuum generation”. In: *JOSA B* 37.3 (2020), pp. 635–644.

[60] J. S. Feehan et al. “Noise-related polarization dynamics for femto and picosecond pulses in normal dispersion fibers”. In: *Opt. Express* 28.15 (July 2020), pp. 21447–21463. DOI: 10.1364/OE.396404. URL: http://www.opticsexpress.org/abstract.cfm?URI=oe-28-15-21447.

[61] B. Sierro et al. “Reducing the noise of fiber supercontinuum sources to its limits by exploiting cascaded soliton and wave breaking nonlinear dynamics”. In: *Optica* 9.4 (2022), pp. 352–359.

[62] P. Hänzi et al. “Benefits of cascaded nonlinear dynamics in hybrid fibers for low-noise supercontinuum generation”. In: *Optics express* 31.7 (2023), pp. 11067–11079.

[63] T. Sylvestre et al. “Recent advances in supercontinuum generation in specialty optical fibers [Invited]”. In: *Journal of the Optical Society of America B* 38.12 (Oct. 2021), F90. DOI: 10.1364/josab.439330.

[64] D. M. Lesko et al. “A six-octave optical frequency comb from a scalable few-cycle erbium fibre laser”. In: *Nat. Photonics* 15 (2021), pp. 281–286.

[65] U. Elu et al. “Seven-octave high-brightness and carrier-envelope-phase-stable light source”. In: *Nature Photonics* 15.4 (Dec. 2021), pp. 277–280. DOI: 10.1038/s41566-020-00735-1.

[66] L. Lundberg et al. “Phase-coherent lightwave communications with frequency combs”. In: *Nature Communications* 11.1 (Jan. 2020), p. 201. DOI: 10.1038/s41467-019-14010-7.

[67] C. Deakin and Z. Liu. “Dual frequency comb assisted analog-to-digital conversion”. In: *Optics Letters* 45.1 (2020), p. 173. DOI: 10.1364/ol.45.000173.

[68] E. Temprana et al. “Overcoming Kerr-induced capacity limit in optical fiber transmission”. In: *Science* 348.6242 (June 2015), pp. 1445–1448. DOI: 10.1126/science.aab1781.

[69] S. Wabnitz. “Modulational polarization instability of light in a nonlinear birefringent dispersive medium”. In: *Phys Rev A* 38.4 (1988), p. 2018.

[70] A. M. Heidt et al. “Improved retrieval of complex supercontinuum pulses from XFROG traces using a ptychographic algorithm”. In: *Opt Lett* 41.21 (2016), pp. 4903–4906.

[71] P. Abdolghader et al. “All normal dispersion nonlinear fibre supercontinuum source characterization and application in hyperspectral stimulated Raman scattering microscopy”. In: *Opt. Express* 28.24 (2020), pp. 35997–36008.

[72] K. J. Kaltenecker et al. “Near-infrared nanospectroscopy using a low-noise supercontinuum source”. In: *APL Photonics* 6.6 (2021), p. 066106. ISSN: 2378-0967. DOI: 10.1063/5.0050446.

[73] S. Rao D.S. et al. “Shot-noise limited, supercontinuum-based optical coherence tomography”. In: *Light: Science & Applications* 10.1 (2021), p. 133. DOI: 10.1038/s41377-021-00574-x. eprint: 2010.05226 (physics.optics).

[74] H. Tu et al. “Stain-free histopathology by programmable supercontinuum pulses”. In: *Nat. Photonics* 10.8 (2016), p. 534. DOI: https://doi.org/10.1038/nphoton.2016.94.

[75] K. P. Herdzik et al. “Multimodal spectral focusing CARS and SFG microscopy with a tailored coherent continuum from a microstructured fiber”. In: *Applied Physics B* 126 (2020), pp. 1–13.

[76] A. M. Heidt et al. “Low noise all-fiber amplification of a coherent supercontinuum at 2 μm and its limits imposed by polarization noise”. In: *Sci. Rep.* 10.1 (2020), p. 16734.

[77] A. Rampur et al. “Ultra low-noise coherent supercontinuum amplification and compression below 100 fs in an all-fiber polarization-maintaining thulium fiber amplifier”. In: *Opt. Express* 27.24 (2019), pp. 35041–35051.

[78] N. M. Israelsen et al. “Real-time high-resolution mid-infrared optical coherence tomography”. In: *Light: Science & Applications* 8.1 (2019), p. 11.

[79] T. Hori et al. “Flatly broadened, wideband and low noise supercontinuum generation in highly nonlinear hybrid fiber”. In: *Opt. Express* 12.2 (Jan. 2004), pp. 317–324. DOI: 10.1364/OPEX.12.000317. URL: http://www.opticsexpress.org/abstract.cfm?URI=oe-12-2-317.

[80] P. Ciąćka et al. “Dispersion measurement of ultra-high numerical aperture fibers covering thulium, holmium, and erbium emission wavelengths”. In: *J. Opt. Soc. Am. B* 35.6 (June 2018), pp. 1301–1307. DOI: 10.1364/JOSAB.35.001301. URL: http://josab.osa.org/abstract.cfm?URI=josab-35-6-1301.

[81] S. Preble. *UHNA Fiber – Efficient Coupling to Silicon Waveguides. Nufern Application Note NuApp-3*. 2016. URL: https://www.coherent.com/content/dam/coherent/site/en/resources/application-note/components-and-accessories/specialty-optical-fibers/uhna-fiber-efficient-coupling-to-silicon-waveguides.pdf.

[82] Q. Lin and G. P. Agrawal. "Raman response function for silica fibers". In: *Opt. Lett.* 31.21 (Nov. 2006), pp. 3086–3088. DOI: 10.1364/OL.31.003086. URL: http://ol.osa.org/abstract.cfm?URI=ol-31-21-3086.

[83] D. Marcuse. "Gaussian approximation of the fundamental modes of graded-index fibers". In: *JOSA* 68.1 (1978), pp. 103–109.

[84] R. G. Smith. "Optical power handling capacity of low loss optical fibers as determined by stimulated Raman and Brillouin scattering". In: *Applied optics* 11.11 (1972), pp. 2489–2494.

[85] D. Spangenberg et al. "Time-domain ptychography". In: *Phys. Rev. A* 91 (2 Feb. 2015), p. 021803. DOI: 10.1103/PhysRevA.91.021803. URL: http://link.aps.org/doi/10.1103/PhysRevA.91.021803.

[86] A. Rampur et al. "Temporal fine structure of all-normal dispersion fiber supercontinuum pulses caused by non-ideal pump pulse shapes". In: *Opt. Express* 28.11 (2020), pp. 16579–16593.

[87] A. Klose et al. "Tunable, stable source of femtosecond pulses near 2 um via supercontinuum of an Erbium mode-locked laser". In: *Optics Express* 22.23 (Nov. 2014), p. 28400. DOI: 10.1364/oe.22.028400.

[88] B. Resan et al. "1% rms amplitude noise from a 30 fs continuum based source tunable from 800 to 1250 nm". In: *Opt. Express* 24.13 (June 2016), p. 14960. DOI: 10.1364/oe.24.014960.

[89] F. Poletti and P. Horak. "Description of ultrashort pulse propagation in multimode optical fibers". In: *J. Opt. Soc. Am. B* 25.10 (Oct. 2008), pp. 1645–1654. DOI: 10.1364/JOSAB.25.001645. URL: http://josab.osa.org/abstract.cfm?URI=josab-25-10-1645.

[90] J. W. Nicholson and M. F. Yan. "Cross-coherence measurements of supercontinua generated in highly-nonlinear, dispersion shifted fiber at 1550 nm". In: *Opt. Express* 12.4 (2004), p. 679. DOI: 10.1364/opex.12.000679.

[91] X. Gu et al. "Experimental studies of the coherence of microstructure-fiber supercontinuum". In: *Opt. Express* 11.21 (2003), pp. 2697–2703. URL: http://www.opticsexpress.org/abstract.cfm?URI=oe-11-21-2697.

[92] D. Türke et al. "Coherence of subsequent supercontinuum pulses generated in tapered fibers in the femtosecond regime". In: *Opt. Express* 15.5 (2007), p. 2732. DOI: 10.1364/oe.15.002732.

[93] N. Singh et al. "Octave-spanning coherent supercontinuum generation in silicon on insulator from 1.06μm to beyond 2.4μm". In: *Light Sci. Appl.* 7.1 (2018), pp. 17131–17131. DOI: 10.1038/lsa.2017.131.

[94] A. R. Johnson et al. “Octave-spanning coherent supercontinuum generation in a silicon nitride waveguide”. In: *Optics letters* 40.21 (2015), pp. 5117–5120.

[95] M. Närhi et al. “Experimental Measurement of the Second-Order Coherence of Supercontinuum”. In: *Phys. Rev. Lett.* 116.24 (2016), p. 243901. DOI: 10.1103/physrevlett.116.243901.

[96] K. Tarnowski et al. “Compact all-fiber source of coherent linearly polarized octave-spanning supercontinuum based on normal dispersion silica fiber”. In: *Scientific reports* 9.1 (2019), pp. 1–8.

[97] J. W. Nicholson et al. “Coherence of supercontinua generated by ultrashort pulses compressed in optical fibers”. In: *Opt. Lett.* 33.18 (2008), pp. 2038–2040. URL: http://ol.osa.org/abstract.cfm?URI=ol-33-18-2038.

[98] D. Brida et al. “Ultrabroadband Er: fiber lasers”. In: *Laser & Photonics Reviews* 8.3 (2014), pp. 409–428.

[99] A. M. Heidt. “Pulse preserving flat-top supercontinuum generation in all-normal dispersion photonic crystal fibers”. In: *J. Opt. Soc. Am. B* 27.3 (2010), pp. 550–559. URL: http://josab.osa.org/abstract.cfm?URI=josab-27-3-550.

[100] J. Kim and Y. Song. “Ultralow-noise mode-locked fiber lasers and frequency combs: principles, status, and applications”. In: *Advances in Optics and Photonics* 8.3 (Aug. 2016), p. 465. DOI: 10.1364/aop.8.000465.

[101] E. Ivanov, S. Diddams, and L. Hollberg. “Study of the excess noise associated with demodulation of ultra-short infrared pulses”. In: *IEEE Transactions on Ultrasonics, Ferroelectrics and Frequency Control* 52.7 (July 2005), pp. 1068–1074. DOI: 10.1109/tuffc.2005.1503992.

[102] N. Newbury and B. Washburn. “Theory of the frequency comb output from a femtosecond fiber laser”. In: *IEEE Journal of Quantum Electronics* 41.11 (Nov. 2005), pp. 1388–1402. DOI: 10.1109/jqe.2005.857657.

[103] Y. Hua et al. “Femtosecond two-color source synchronized at 100-as-precision based on SPM-enabled spectral selection”. In: *Opt. Lett.* 45.13 (2020), pp. 3410–3413.

[104] S. L. Camenzind et al. “Shot-noise limited dual-comb supercontinuum”. (submitted to Opt. Express).

[105] H. R. Telle et al. “Carrier-envelope offset phase control: A novel concept for absolute optical frequency measurement and ultrashort pulse generation”. In: *Applied Physics B* 69 (1999), pp. 327–332. URL: https://doi.org/10.1007/s003400050813.

[106] D. J. Jones et al. “Carrier-envelope phase control of femtosecond mode-locked lasers and direct optical frequency synthesis”. In: *Science* 288 (2000), pp. 635–639. DOI: 10.1126/science.288.5466.635. URL: https://www.science.org/doi/abs/10.1126/science.288.5466.635.

[107] A. Apolonski et al. “Controlling the phase evolution of few-cycle light pulses”. In: *Phys. Rev. Lett* 85 (2000), pp. 740–743. DOI: 10.1103/PhysRevLett.85.740. URL: https://link.aps.org/doi/10.1103/PhysRevLett.85.740.

[108] S. Schiller. “Spectrometry with frequency combs”. In: *Opt. Lett.* 27.9 (May 2002), pp. 766–768. DOI: 10.1364/OL.27.000766. URL: https://opg.optica.org/ol/abstract.cfm?URI=ol-27-9-766.

[109] F. Keilmann, C. Gohle, and R. Holzwarth. “Time-domain mid-infrared frequency-comb spectrometer”. In: *Opt. Lett.* 29.13 (July 2004), pp. 1542–1544. DOI: 10.1364/OL.29.001542. URL: https://opg.optica.org/ol/abstract.cfm?URI=ol-29-13-1542.

[110] B. Bernhardt et al. “Cavity-enhanced dual-comb spectroscopy”. In: *Nature Photonics* 4 (2010), pp. 55–57. DOI: 10.1038/nphoton.2009.217. URL: https://doi.org/10.1038/nphoton.2009.217.

[111] I. Coddington et al. “Rapid and precise absolute distance measurements at long range”. In: *Nature Photonics* 3 (2009), pp. 351–356. DOI: 10.1038/nphoton.2009.94. URL: https://doi.org/10.1038/nphoton.2009.94.

[112] M. Brehm, A. Schliesser, and F. Keilmann. “Spectroscopic near-field microscopy using frequency combs in the mid-infrared”. In: *Opt. Express* 14.23 (Nov. 2006), pp. 11222–11233. DOI: 10.1364/OE.14.011222. URL: https://opg.optica.org/oe/abstract.cfm?URI=oe-14-23-11222.

[113] G. B. Rieker et al. “Frequency-comb-based remote sensing of greenhouse gases over kilometer air paths”. In: *Optica* 1.5 (Nov. 2014), pp. 290–298. DOI: 10.1364/OPTICA.1.000290. URL: https://opg.optica.org/optica/abstract.cfm?URI=optica-1-5-290.

[114] E. Vicentini et al. “Dual-comb hyperspectral digital holography”. In: *Nature Photonics* 15 (2021), pp. 890–894. DOI: 10.1038/s41566-021-00892-x. URL: https://doi.org/10.1038/s41566-021-00892-x.

[115] P. A. Elzinga et al. “Pump/probe method for fast analysis of visible spectral signatures utilizing asynchronous optical sampling”. In: *Appl. Opt.* 26.19 (Oct. 1987), pp. 4303–4309. DOI: 10.1364/AO.26.004303. URL: https://opg.optica.org/ao/abstract.cfm?URI=ao-26-19-4303.

[116] K. Weingarten, M. Rodwel, and D. Bloom. “Picosecond optical sampling of GaAs integrated circuits”. In: *IEEE Journal of Quantum Electronics* 24.2 (1988), pp. 198–220. DOI: 10.1109/3.115.

[117] T. Ideguchi et al. “Coherent Raman spectro-imaging with laser frequency combs”. In: *Nature* 502 (2013), pp. 355–358. DOI: 10.1038/nature12607. URL: https://doi.org/10.1038/nature12607.

[118] Y. Fang et al. “Recent Progress of Supercontinuum Generation in Nanophotonic Waveguides”. In: *Laser & Photonics Reviews* 17.1 (2023), p. 2200205. DOI: https://doi.org/10.1002/lpor.202200205. eprint: https://onlinelibrary.wiley.com/doi/pdf/10.1002/lpor.202200205. URL: https://onlinelibrary.wiley.com/doi/abs/10.1002/lpor.202200205.

[119] C. R. Phillips et al. “Coherently averaged dual-comb spectroscopy with a low-noise and high-power free-running gigahertz dual-comb laser”. In: *Optics Express* 31.5 (2023). 1GHz Dual Comb, pp. 7103–7119.

[120] J. Pupeikis et al. “Spatially multiplexed single-cavity dual-comb laser”. In: *Optica* 9.7 (July 2022), pp. 713–716. DOI: 10.1364/OPTICA.457787. URL: https://opg.optica.org/optica/abstract.cfm?URI=optica-9-7-713.

[121] P. Guay et al. “Linear dual-comb interferometry at high power levels”. In: *Opt. Express* 31.3 (Jan. 2023), pp. 4393–4404. DOI: 10.1364/OE.481671. URL: https://opg.optica.org/oe/abstract.cfm?URI=oe-31-3-4393.

[122] F. Kartner, I. Jung, and U. Keller. “Soliton mode-locking with saturable absorbers”. In: *IEEE Journal of Selected Topics in Quantum Electronics* 2.3 (1996), pp. 540–556. DOI: 10.1109/2944.571754.

[123] N. R. Newbury, I. Coddington, and W. Swann. “Sensitivity of coherent dual-comb spectroscopy”. In: *Optics Express* 18.8 (Mar. 2010), p. 7929. DOI: 10.1364/oe.18.007929.

[124] P. Guay et al. “Understanding photodetection nonlinearity in dual-comb interferometry”. In: *OSA Continuum* 4.9 (Sept. 2021), pp. 2460–2467. DOI: 10.1364/OSAC.435015. URL: https://opg.optica.org/osac/abstract.cfm?URI=osac-4-9-2460.

[125] J. Roy et al. “Continuous real-time correction and averaging for frequency comb interferometry”. In: *Opt. Express* 20.20 (Sept. 2012), pp. 21932–21939. DOI: 10.1364/OE.20.021932. URL: https://opg.optica.org/oe/abstract.cfm?URI=oe-20-20-21932.

[126] E. Genier et al. “Amplitude noise and coherence degradation of femtosecond supercontinuum generation in all-normal-dispersion fibers”. In: *J. Opt. Soc. Am. B* 36.2 (Feb. 2019), A161–A167. DOI: 10.1364/JOSAB.36.00A161. URL: http://josab.osa.org/abstract.cfm?URI=josab-36-2-A161.

[127] N. B. Hébert et al. “Self-Correction Limits in Dual-Comb Interferometry”. In: *IEEE Journal of Quantum Electronics* 55.4 (2019), pp. 1–11. DOI: 10.1109/JQE.2019.2918935.

[128] M. Walsh, P. Guay, and J. Genest. “Unlocking a lower shot noise limit in dual-comb interferometry”. In: *APL Photonics* 8.7 (July 2023), p. 071302. ISSN: 2378-0967. DOI: 10.1063/5.0153724. eprint: https://pubs.aip.org/aip/app/article-pdf/doi/10.1063/5.0153724/18030889/071302_1_5.0153724.pdf. URL: https://doi.org/10.1063/5.0153724.

[129] M. Walsh et al. “Mode-resolved, shot noise limited, dual-comb spectroscopy with independent free running lasers”. In: *Optica Sensing Congress 2023 (AIS, FTS, HISE, Sensors, ES)*. Optica Publishing Group, 2023, JTh1A.1. DOI: 10.1364/AIS.2023.JTh1A.1. URL: https://opg.optica.org/abstract.cfm?URI=AIS-2023-JTh1A.1.

[130] A. Azari et al. “Polarization Dependence in Nonlinear Fiber Optics: Modeling and Experiment”. Consulted 2024-04-04. 2006. URL: https://ece.umd.edu/merit/archives/merit2006/merit_fair06_papers/Paper_16_Azari+Pleban.pdf.

[131] C. R. Smith, R. D. Engelsholm, and O. Bang. “Pulse-to-pulse relative intensity noise measurements for ultrafast lasers”. In: *Optics Express* 30.5 (2022), pp. 8136–8150.

[132] P. Welch. “The use of fast Fourier transform for the estimation of power spectra: a method based on time averaging over short, modified periodograms”. In: *IEEE Transactions on audio and electroacoustics* 15.2 (1967), pp. 70–73.

[133] W. H. Press. *Numerical recipes 3rd edition: The art of scientific computing*. 2007.

[134] R. Paschotta. “Noise of mode-locked lasers (Part II): timing jitter and other fluctuations”. In: *Applied Physics B* 79 (2004), pp. 163–173.

[135] R. D. Engelsholm and O. Bang. “Supercontinuum noise reduction by fiber undertapering”. In: *Optics express* 27.7 (2019), pp. 10320–10331.

[136] I. Bravo Gonzalo et al. “Polarization noise places severe constraints on coherence of all-normal dispersion femtosecond supercontinuum generation”. In: *Scientific reports* 8.1 (2018), p. 6579.

[137] R. H. Stolen et al. “Raman response function of silica-core fibers”. In: *JOSA B* 6.6 (1989), pp. 1159–1166.

[138] M. Kuschnerov et al. “Transmission of commercial low latency interfaces over hollow-core fiber”. In: *Journal of Lightwave Technology* 34.2 (2016), pp. 314–320.

[139] G. Humbert et al. “Hollow core photonic crystal fibers for beam delivery”. In: *Optics express* 12.8 (2004), pp. 1477–1484.

[140] M. Michieletto et al. “Hollow-core fibers for high power pulse delivery”. In: *Optics express* 24.7 (2016), pp. 7103–7119.

[141] R. Yu et al. “Hollow-core photonic crystal fiber gas sensing”. In: *Sensors* 20.10 (2020), p. 2996.

[142] J. Li et al. “Structure design and application of hollow core microstructured optical fiber gas sensor: A review”. In: *Optics & Laser Technology* 135 (2021), p. 106658.

[143] J. C. Travers et al. “Ultrafast nonlinear optics in gas-filled hollow-core photonic crystal fibers [Invited]”. In: *J. Opt. Soc. Am. B* 28.12 (Dec. 2011), A11–A26. DOI: 10.1364/JOSAB.28.000A11. URL: https://opg.optica.org/josab/abstract.cfm?URI=josab-28-12-A11.

[144] C. Markos et al. “Hybrid photonic-crystal fiber”. In: *Reviews of Modern Physics* 89.4 (2017), p. 045003.

[145] A. I. Adamu et al. “Deep-UV to mid-IR supercontinuum generation driven by mid-IR ultrashort pulses in a gas-filled hollow-core fiber”. In: *Scientific reports* 9.1 (2019), p. 4446.

[146] M. S. Habib et al. “Multi-stage generation of extreme ultraviolet dispersive waves by tapering gas-filled hollow-core anti-resonant fibers”. In: *Opt. Express* 26.19 (Sept. 2018), pp. 24357–24371. DOI: 10.1364/OE.26.024357. URL: https://opg.optica.org/oe/abstract.cfm?URI=oe-26-19-24357.

[147] E. A. Marcatili and R. Schmeltzer. “Hollow metallic and dielectric waveguides for long distance optical transmission and lasers”. In: *Bell System Technical Journal* 43.4 (1964), pp. 1783–1809.

[148] R. Trebino. *Frequency-resolved optical gating: the measurement of ultrashort laser pulses*. Springer Science & Business Media, 2012.

[149] X. Xie, Y. Deng, and S. L. Johnson. “Compact and robust supercontinuum generation and post-compression using multiple thin plates”. In: *High Power Laser Science and Engineering* 9 (2021), e66.

[150] E. Nibbering et al. “Determination of the inertial contribution to the nonlinear refractive index of air, N 2, and O 2 by use of unfocused high-intensity femtosecond laser pulses”. In: *JOSA B* 14.3 (1997), pp. 650–660.

[151] M. N. Polyanskiy. “Refractiveindex. info database of optical constants”. In: *Scientific Data* 11.1 (2024), p. 94.

List of acronyms

ANDi all-normal dispersion

ASE amplified spontaneous emission

DCI dual-comb interferometry

DFT discrete Fourier transform

DW dispersive wave

ESA electronic spectrum analyzer

FOM figure of merit

FUT fiber under test

FWHM full width at half maximum

FWM four-wave mixing

GNLSE generalized nonlinear Schrödinger equation

GVD group-velocity dispersion

HC hollow-core

HNLF highly nonlinear fiber

IGM interferogram

MFD mode field diameter

MI modulation instability

MOPA master-oscillator power-amplifier

MPR mixed parametric Raman

NEP noise equivalent power

NLSE nonlinear Schrödinger equation

OFC optical frequency comb

OSNR optical signal-to-noise ratio

OWB optical wave-breaking

PCF photonic crystal fiber

PER polarization extinction ration

PM polarization-maintaining

PMI polarization modulation instability

PSD power spectral density

RF radio frequency

RHS right-hand side

RIN relative intensity noise

RIU relative index units

RMS root mean square

SC supercontinuum

SCG supercontinuum generation

SMF single-mode fiber

SN shot noise

SNR signal-to-noise ratio

SPM self-phase modulation

SRS stimulated Raman scattering

TWN technical white noise

UPPE unidirectional pulse propagation equation

UV ultraviolet

WSS wide-sense stationary

XMI cross-phase modulation instability

XPM cross-phase modulation

ZDW zero dispersion wavelength

List of Publications

Work on this dissertation resulted in the following publications:

Peer-reviewed Journal Publications

- A. Rampur, D.-M. Spangenberg, B. Sierro, P. Hänzi, M. Klimczak, and A. M. Heidt. "Perspective on the next generation of ultra-low noise fiber supercontinuum sources and their emerging applications in spectroscopy, imaging, and ultrafast photonics". In: *Applied physics letters* 118.24 (2021), p. 240504. URL: https://doi.org/10.1063/5.0053436
- B. Sierro, P. Hänzi, D. Spangenberg, A. Rampur, and A. M. Heidt. "Reducing the noise of fiber supercontinuum sources to its limits by exploiting cascaded soliton and wave breaking nonlinear dynamics". In: *Optica* 9.4 (2022), pp. 352–359
- P. Hänzi, B. Sierro, Z. Liu, V. Romano, A. Rampur, and A. M. Heidt. "Benefits of cascaded nonlinear dynamics in hybrid fibers for low-noise supercontinuum generation". In: *Optics express* 31.7 (2023), pp. 11067–11079

Submitted or in Preparation

- S. L. Camenzind, B. Sierro, B. Willenberg, A. Nussbaum-Lapping, A. Rampur, U. Keller, A. Heidt, and C. Phillips. "Shot-noise limited dual-comb supercontinuum". (submitted to Opt. Express)
- B. Sierro, S. L. Camenzind, U. Keller, C. R. Phillips, and A. M. Heidt. "Accurate simulation of noise evolution in nonlinear fiber optics". (in preparation)
- B. Sierro, S. L. Camenzind, U. Keller, C. R. Phillips, and A. M. Heidt. "Dual-comb supercontinuum generation in a single nonlinear fiber using polarization multiplexing". (in preparation)

Peer-reviewed Conference Contributions

- B. Sierro, S. L. Camenzind, B. Willenberg, A. Nussbaum-Lapping, A. Rampur, U. Keller, C. R. Phillips, and A. M. Heidt. "Strong Reduction

of Frequency-Comb Noise in All-Normal Dispersion Supercontinuum". In: *Optica Advanced Photonics Congress*. Optica Publishing Group. 2024, SoM1F.3

- **Invited talk:**
  A. M. Heidt, S. L. Camenzind, B. Sierro, A. Rampur, B. Willenberg, U. Keller, and C. R. Phillips. "1-GHz Dual-Comb Supercontinuum from a Single Nonlinear Fiber Using Polarization Multiplexing". In: *Optica Advanced Photonics Congress*. Optica Publishing Group. 2024, NpTu2E.4

- S. L. Camenzind, A. Rampur, B. Sierro, B. Willenberg, A. M. Heidt, U. Keller, and C. R. Phillips. "Shot-Noise Limited Interferometry of a Dual-Comb Supercontinuum Source Generated from a Single ANDi Fiber". In: *CLEO 2024*. Optica Publishing Group, 2024, SF3O.4. URL: https://opg.optica.org/abstract.cfm?URI=CLEO_SI-2024-SF3O.4

- **Invited talk:**
  B. Willenberg, C. Bauer, S. L. Camenzind, J. Pupeikis, Z. Bejm, M. Bollier, A. Nussbaum-Lapping, B. Sierro, A. Rampur, L. Liebermeister, R. Kohlhaas, B. Globisch, A. M. Heidt, U. Keller, and C. R. Phillips. "Single Cavity Dual-comb Lasers with Efficient Wavelength Extensions for Sensing Applications". In: *Optica Sensing Congress*. Optica Publishing Group. 2024, ATu3A.3

- **Post-deadline paper:**
  S. L. Camenzind, A. Rampur, B. Sierro, B. Willenberg, A. Heidt, U. Keller, and C. Phillips. "Shot-Noise Limited 1-GHz Dual-Comb Supercontinuum from a Single-Cavity Dual-Comb and a Single ANDi Fiber". In: *Advanced Solid State Lasers*. Optica Publishing Group. 2023, AW4A.1

- P. Hänzi, B. Sierro, D. Spangenberg, A. Rampur, and A. M. Heidt. "Low Noise Supercontinuum Using Cascaded Soliton and Wave-Breaking Nonlinear Dynamics". In: *Optica Advanced Photonics Congress 2022*. Optica Publishing Group, 2022, SoW5G.2. DOI: 10.1364/SOF.2022.SoW5G.2. URL: https://opg.optica.org/abstract.cfm?URI=SOF-2022-SoW5G.2

- D.-M. Spangenberg, B. Sierro, A. Rampur, P. Hänzi, A. Hartung, P. Mergo, K. Tarnowski, T. Martynkien, M. Klimczak, and A. M. Heidt. "Noise fingerprints of fiber supercontinuum sources". In: *The European Conference on Lasers and Electro-Optics*. Optica Publishing Group. 2021, cd_5_3

- **Invited talk:**
  A. M. Heidt, B. Sierro, D. Spangenberg, A. Rampur, and M. Klimczak. "Specialty Optical Fibers for Coherent and Low-Noise Supercontinuum Generation and their Application in Ultrafast Photonics". In: *Specialty Optical Fibers*. Optica Publishing Group. 2020, SoTu1H.1

- B. Sierro and A. M. Heidt. "Noise evolution in all-normal dispersion fiber supercontinuum and its impact on ultrafast experiments and few-cycle pulse generation". In: *Specialty Optical Fibers*. Optica Publishing Group. 2020, SoTu1H.3

- D.-M. Spangenberg, B. Sierro, and A. M. Heidt. “Polarization-dependent relative intensity noise of fiber supercontinuum sources”. In: *EPJ Web of Conferences*. Vol. 243. EDP Sciences. 2020, p. 17004